Quantum Well and Quantum Dot broadband Optical Devices for Optical Coherence Tomography Applications

By

Negin Peyvast

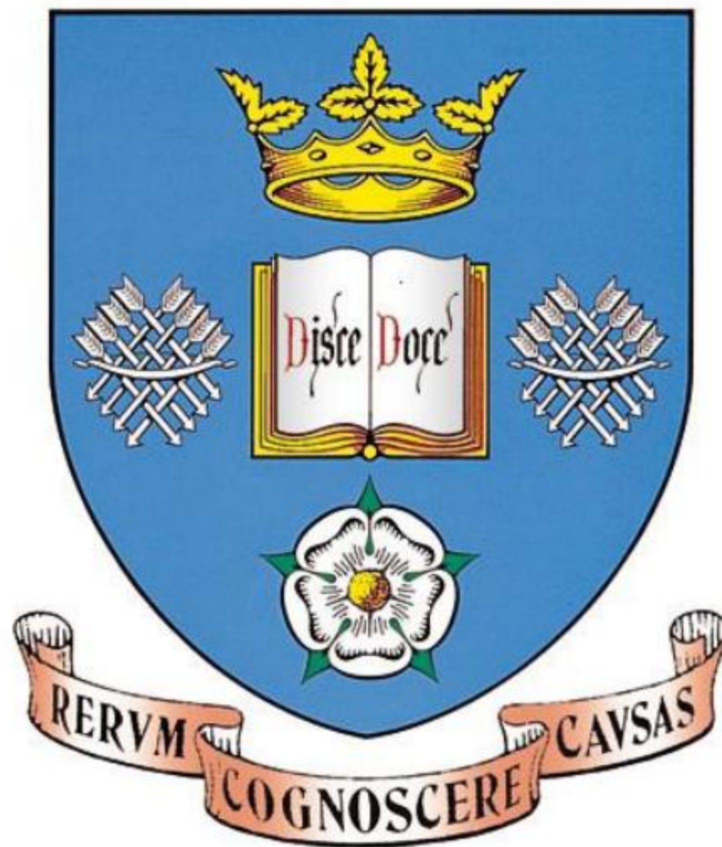

Department of Electronic and Electrical Engineering

Thesis submitted to the University of Sheffield for the Degree of Doctor of Philosophy

2016

Intentionally Blank

Abstract

In this thesis quantum well (QW) and quantum dot (QD) based devices are investigated with the aim of obtaining broad bandwidth light sources for optical coherence tomography (OCT) applications. QD based structures have many possible advantages for broadband applications due to their inhomogeneous broadening. However, more investigation is required in order to fulfil this potential.

Firstly, in chapter one, an introduction to the fundamental principles of semiconductor heterostructures is provided followed by basic concepts of OCT. The experimental techniques used in this thesis are outlined and briefly discussed. Brief reviews of the gain measurement techniques which have been used throughout this thesis are presented.

Free carrier effects have been highlighted as a source of line-width broadening in QD structures. However, to date the effects of free carriers have mostly been experimentally determined at comparatively high carrier densities. In chapter 2 I develop a model for the gain and spontaneous emission spectra of QD active elements and show that not only are free carrier effects important at high QD occupancies, but also at much lower carrier densities where QD lasers would normally operate. Furthermore, it is shown that the choice of carrier distribution function is far less important than was previously thought in describing the experimentally observed gain and spontaneous emission spectra.

The literature has suggested that incorporating QW layers in hybrid QW/QD structures changes the behaviour of the QDs. Optical pumping of the QD active element by emission from the QW active element is investigated experimentally in chapter 3. Analysis of a QD laser, a hybrid QW/QD super luminescence diode (SLD) and mesa

diodes with different active element designs show that emission from the quantum well layer does indeed modify the QD spontaneous emission, suggesting optical pumping of the QD states and the prospect for enhanced gain from the QD ground-state.

Finally in chapter 4, different configurations of swept light sources (SLSs) are implemented with the aim of obtaining broader spectral bandwidth. It is demonstrated that increasing the gain of the QD-SOA is important in enhancing the sweep range. The use of complimentary SOAs is then explored. InP QW-SOAs and GaAs based QD-SOAs have overlapping gain and SE spectra which is utilised in a swept source laser (SSL) and filtered ASE configuration SLS. The results suggest that such sources may be able to achieve ~220nm sweep bandwidths.

Chapter 5 summarizes the whole thesis and provides an overview of future work.

Dedicated to my beloved parents and husband who have supported me all the way.

Acknowledgements

I would like to express my special appreciation and thanks to my supervisor Professor Dr. Richard Hogg, who has been a tremendous mentor for me. This work could never have been done or have made any sense without the enthusiastic support and guidance of him. Without his help and invaluable insights it would not have been as comprehensive or complete.

This work could have never been done as a single enterprise, only through the help of others. I would like to thank Dr. David Childs for his invaluable help and technical support during the course of my PhD. Special thanks to Dr. Nasser Babazadeh for his support, patience and precious advice through all these years, especially his excellent fabrication advice and assistance. My gratitude also goes to Dr. Kenneth Kennedy, my second supervisor, and Dr. Kristian Groom for sharing their knowledge and skills with me. Additionally, the help and advice from Professor Osamu Wada is fully appreciated.

I would also like to thank all my colleagues particularly Siming, Zhou, Xiao, Kristof, Jon, Zheng, Deepa, Avan, Noura, Hifsa, Omar, Majid, Sourabh, Soroush, Ian, Tim, Hongchi, Wei, Razvan and Pavlo.

Special thanks to my family. Words cannot express how grateful I am to my mother and father for all of the sacrifices they have made for me. I would also like to thank my beloved husband, Dr. Sina Askari, for his endless support and understanding.

List of publications

Journal papers:

1- **N. Peyvast**, N. Babazadeh, S. Chen, D.T.D. Childs and R. A. Hogg, "*Role of Quantum Well in Optical Pumping of Quantum Dots in QW/QD Hybrid Structures*," Manuscript submitted to APL.

2- **N. Peyvast,** K. Zhou, R. A. Hogg, and D. T. D. Childs, "*Dominant role of many-body effects on the carrier distribution function of quantum dot lasers*," Appl. Phys. Exp. 9, 032705 (2016). (Has been selected as Spotlight Article).

3- **N. Peyvast**, H. Shahid, R. A. Hogg, and D. T. D. Childs, "*Monte Carlo model incorporating many-body effects for determining the gain spectra of quantum dot lasers*," Appl. Phys. Exp. 8, 122102 (2015).

4- **N. Peyvast**, S. Chen, K. Zhou, N. Babazadeh, A.A. Khozim, Z. Zhang , D.T. D. Childs, O. Wada, M. Hugues R.A. Hogg, T. Kageyama, K. Nishi, K. Takemasa and M. Sugawara, "*Development of Broad Spectral Bandwidth Hybrid QW/QD Structures from 1000-1400 nm*," Proc. SPIE Vol. 9002 (SPIE, Bellingham, WA 2014), 900204.

5- **N. Peyvast**, D.T.D. Childs, N. Krstajić, Z. Lu, S.J. Matcher, D. Livshits, A. Shkolnik, I. Krestnikov, R. A. Hogg , "*Self-assembled quantum dot-based swept laser source for optical coherence tomography applications*", Proc. SPIE 8213, Optical Coherence Tomography and Coherence Domain Optical Methods in Biomedicine XVI, 821336 (2012).

6- N. Krstajic, D. Childs, **N. Peyvas**t, D. Kasaragod, S. J. Matcher, I. Krestnikov, R. Hogg, "*Evaluation of a swept-laser optical coherence tomography light source based on a novel quantum-dot based semiconductor optical amplifier*", Proc. SPIE 8091, Optical Coherence Tomography and Coherence Techniques V, 80911S (2011).

Oral presentations

1- **N. Peyvast**, K. Zhou, R. A. Hogg, and D. T. D. Childs, "*Dominant role of many-body effects on the carrier distribution function of quantum dot lasers*," ISLC, Japan, 2016.

2- **N. Peyvast**, D.T. D. Childs, K. Zhou, R.A. Hogg, T. Kageyama, K. Nishi, K. Takemasa, and M. Sugawara, "*Evaluation of Free Carrier Effects on the Gain and Spontaneous Emission Spectra of InAs/GaAs Quantum Dot Lasers,*" SPIE Photonics West, San Francisco, Feb 2015.

3- **N. Peyvast**, S. Chen, K. Zhou, N. Babazadeh, A.A. Khozim, Z. Zhang , D.T. D. Childs, O. Wada, M. Hugues R.A. Hogg, T. Kageyama, K. Nishi, K. Takemasa and M. Sugawara, "*Development of Broad Spectral Bandwidth Hybrid QW/QD Structures from 1000-1400 nm*," SPIE Photonics West, San Francisco, Feb 2014.

4- S. Chen, **N. Peyvast**, K. Zhou, N. Babazadeh, , Z. Zhang, D.T. D. Childs, M. Hugues, O. Wada, R.A. Hogg, T. Kageyama, K. Nishi, K. Takemasa, and M. Sugawara, "*Broad Bandwidth Emission from Hybrid QW/QD Structures*," CLEO_PR, Japan 2013.

5- **N. Peyvast**, D.T.D. Childs, N. Krstajić, S.J. Matcher, D. Livshits, A. Shkolnik, I. Krestnikov, R. A. Hogg, "*Quantum Dot Semiconductor Optical Amplifier Based Swept Laser for Optical Coherence Tomography*", UK Semiconductor Conference, 2011.

Poster presentations

1- **N. Peyvast**, D.T.D. Childs, N. Krstajić, Z. Lu, S.J. Matcher, D. Livshits, A. Shkolnik, I. Krestnikov, R. A. Hogg , "*Self-assembled quantum dot-based swept laser source for optical coherence tomography applications*", The Celebration of the 50th Anniversary of the Diode Laser, UK, Sep 2012.

2- N. Krstajic, D. Childs, **N. Peyvas**t, D. Kasaragod, S. J. Matcher, I. Krestnikov, R. Hogg, "*Evaluation of a swept-laser optical coherence tomography light source based on a novel quantum-dot based semiconductor optical amplifier*", ECBO, Munich, Germany, May 2011.

Contents

Abstract.......... II

Acknowledgements.......... V

List of Publications.......... VI

Chapter 1: Introduction and methodology.......... 1

1.1 Semiconductor laser theory.......... 1

1.1.1 Introduction to semiconductor double hetero structures.......... 1

1.1.2 Optical transition in semiconductors.......... 3

1.1.3 Gain in semiconductor lasers.......... 4

1.1.4 Density of states in semiconductors.......... 5

1.1.5 QD laser development.......... 8

1.1.6 QDs and free carrier effects – Gaps in knowledge.......... 11

1.2 QW/QD hybrid structures.......... 12

1.3 Optical coherence tomography.......... 13

1.3.1 Active element in swept light sources (SLS).......... 16

1.3.2 Spectral window for OCT applications.......... 17

1.3.3 QD devices in OCT systems – Gaps in knowledge.......... 18

1.4 Experimental methods.......... 19

1.4.1 Quantum dot growth - Molecular beam epitaxy.......... 19

1.4.2 Device Fabrication.......... 20

1.4.3 Hakki Paoli gain measurement method.......... 23

1.4.4 Segmented contact method.......... 25

Chapter 2: Effects of the Carrier Distributions on Quantum Dot Lasers.......... 32

2.1 Introduction.......... 32

2.2 Carrier distribution in semiconductor QDs.......... 33

2.3 Free carrier effects in QDs.......... 37

2.4 Previous work.......... 39

2.5 Gap in knowledge.......... 44

2.6 Monte Carlo model.......... 45

2.7 Comparison with existing data.......... 51

2.8 Comparison of incorporating free-carrier effects for samples with varying inhomogeneous linewidth and state separation...57
2.8.1 Ensemble B...57
2.8.1.1 Simulation results without free carrier effects.........................57
2.8.1.2 Simulation results including free carrier effects.......................59
2.8.2 Ensemble C...60
2.8.2.1 Simulation results without free carrier effects.........................60
2.8.2.2 Simulation results including free carrier effects.......................64
2.9 Experimental study - State-of-the-art QD laser material.......................................66
2.10 Ln(1-Pm) plots..71
2.11 Discussion..72
2.12 Summary and future work..73

Chapter 3: Study of QW optical pumping effects on QDs in hybrid QW/QD samples.81
3.1 Introduction..81
3.2 Previous work and motivation..81
3.3 Methodology...85
3.3.1 QD laser...85
3.3.2 Superluminescent diode..86
3.3.3 Mesa diodes...91
3.3.3.1 QD sample: QLF1375-AD..93
3.3.3.1.1 Wafer structure...93
3.3.3.1.2 Experimental results...94
3.3.3.2 Hybrid QW/QD sample: QLF1375-AG................................97
3.3.3.2.1 Wafer structure...97
3.3.3.2.2 Experimental results...98
3.3.3.2.3 Discussion...101
3.3.3.3 Digital alloy QW with chirped QDs: QLF1375-AI................102
3.3.3.3.1 Wafer structure...102
3.3.3.3.2 Experimental results...104
3.4 Summary...108
3.5 Future work..108

Chapter 4: Broadband Swept Light Sources for Optical Coherence Tomography Applications..112
4.1 Introduction..112
4.2 Light source………………..112
4.2.1 Semiconductor optical amplifiers as gain medium…………..………114
4.2.2 Filter section..118
4.2.3 Swept light source configurations...119
4.3 Previous work..124
4.4 Gaps in knowledge..125
4.5 Experimental results..127
4.5.1 Comparison of QD-SOA and QW-SOA...127
4.5.2 QD-SOA characterization...129
4.5.3 QW-SOA characterization...130
4.5.4 Identical QD-SOAs..132
4.5.5 Complementary QD-SOA and QW-SOA...135
4.5.6 Multiple pass ASE..137
4.5.6.1 Filter Characterisation...137
4.5.6.2 Analysis of SSL scanning speed..138
4.5.6.3 Configuration of QD & QW swept laser..............................144
4.6 Summary...146
4.7 Future work...146

Chapter 5: Conclusions and future work…..150
Appendix I: Monte Carlo model Methodology..155
Appendix 1: BOA 1130: O-Band booster amplifier..164

Chapter 1: Introduction and methodology

In this chapter, firstly an introduction to the basic concepts of semiconductor structures is presented. The optical transitions in these devices are discussed and the development of lasers based on QDs is reviewed. With recent progress in the development of QD lasers, a thorough understanding of the physics of these structures is required. In this chapter I address the gaps in knowledge in this area and the motivation for introducing a new empirical model explained in chapter 2. An introduction to optical coherence tomography technique is also presented and the requirements of the light source in this technique are explained. Finally the experimental techniques used in this thesis are outlined and briefly discussed.

1.1 Semiconductor laser theory

1.1.1 Introduction to semiconductor double hetero structures

In recent decades, there has been tremendous progress in the development of semiconductor optoelectronic devices due to their unique properties. Small size, being able to be pumped electrically and the manufacturability of these devices made them the most promising candidates for many optoelectronic applications. In this thesis a range of these devices including semiconductor optical amplifiers, mesa diode LEDs (light emitting diodes) and lasers have been investigated. With a common active area, the physics of these devices are quite similar to each other regardless of the device type.

The invention of p-n junction, as the elementary building block in semiconductor devices, is considered as the first step in this progress [1]. With sufficient carrier flow

in this structure, radiative recombination of carriers is possible. In the case of direct bandgap semiconductors (such as InAs and GaAs) this recombination will be accompanied by radiation with a wavelength attributed to the band gap energy.

For devices where gain is required such as lasers and SOAs this recombination rate needs to be under control and loss needs to be minimised. The room temperature operation of these devices, at an acceptable current density level, needs simultaneous confinement of carriers and photons in the active region. To get high efficiency devices hetero structures were introduced [2, 3]. A schematic of a double hetero structure with schematic of the relative refractive index and band gaps is plotted in figure 1.1.

In a double hetero structure usually an intrinsic layer of a lower band gap material (higher refractive index) is sandwiched between doped layers of higher band gap (lower refractive index). Due to high refractive index and low band gap of the intrinsic material, photons and carriers are confined in this region. This layer is usually too thin to confine the light effectively. In order to solve this problem separate confinement heterostructures (SCH) were introduced by adding another two layers with a lower refractive index on the outside of the existing ones.

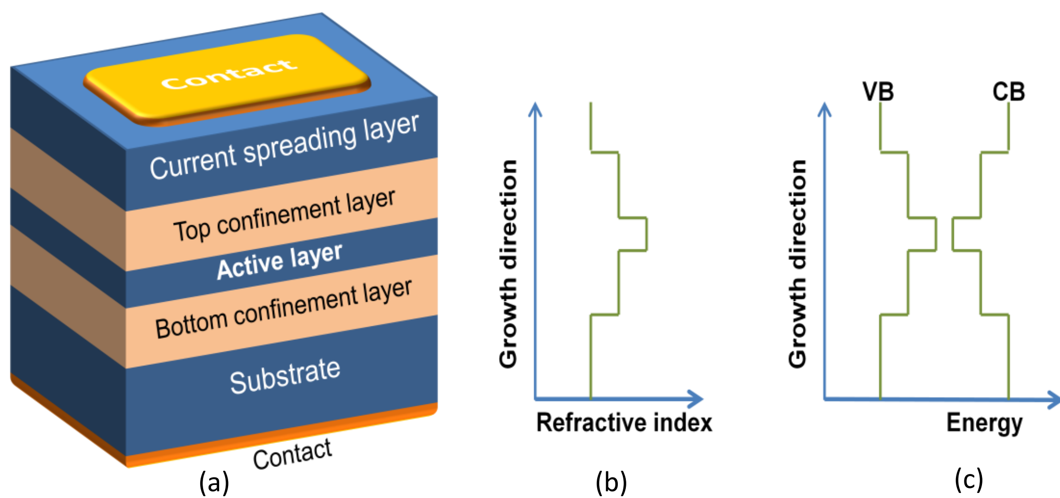

Figure 1.1: (a) schematic of a double hetero structure (b) refractive index and (c) band gap energy of materials in a double hetero structure.

1.1.2 Optical transition in semiconductors

The activation of the gain medium in a semiconductor system mostly occurs with the energy source being provided by an external current. In waveguide designs, similar to a laser diode and SOA, a waveguide is designed to confine the propagating wave in the active region. There are three optical transitions that can occur between the states of the semiconductor; absorption, spontaneous emission and stimulated emission. These transitions are schematically shown in figure 1.2 in a two-level semiconductor.

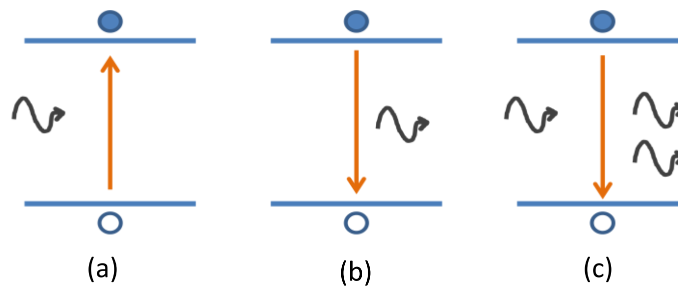

Figure 1.2: (a) absorption, (b) spontaneous emission and (c) stimulated emission of a photon.

In the absorption process, an incident photon (with energy greater than the band-gap) is annihilated and its energy is transferred to an electron which is promoted to the conduction band, leaving a positively charged hole. For high absorption probabilities an empty conduction band and full valence band are required. In the absence of non-linear effects, such as a two photon absorption process, the semiconductor will be transparent for the photons with energies less than the band gap.

In semiconductors there is always a possibility that a carrier in the conduction band recombines spontaneously with a hole in the valence band giving rise to a photon with energy equal to the bandgap. These spontaneously emitted photons are generated with random phase, frequency, and direction and are sources of noise in SOAs and lasers.

In the stimulated emission process a photon with suitable energy interacts with an electron and hole, stimulating their recombination and emission of a photon with exactly the same energy, phase and frequency as the incident photon. These two photons may then contribute to the stimulation of further carrier recombination.

1.1.3 Gain in semiconductor lasers

Radiative transition rates increases in a diode laser by increasing the current density. At low carrier injection level the absorption and spontaneous rates are higher than the stimulation rate and no gain will be observed. By increasing the carrier density the system reaches its transparency point which is the point where we have an equal number of electrons in the conduction and valence bands for an ideal lossless cavity. At this point the absorption and stimulated emission rates are equal. Obviously, for practical systems the transparency point will be reached at higher injection levels as additional stimulated emission is required to overcome additional internal losses. For higher carrier densities, the number of electrons in the conduction band will be greater than that of the valence band (population inversion) and the stimulated emission rate will dominate, leading to optical gain. The threshold gain is the value when the modal gain overcomes all the losses in the cavity, including absorption, scattering and mirror loss.

In a lossless laser cavity with population inversion, the photon intensity (I) will be amplified as photons travel through the cavity. Therefore, gain (g) can be defined as:

$$\frac{dI}{dx} = g.I(x) \qquad (1.1)$$

By integrating the above equation the intensity can be calculated as:

$$I(x) = I_0 e^{gx} \quad (1.2)$$

In order to enable lasing in the cavity, the roundtrip gain must overcome the mirror and internal losses. Assuming R_1 and R_2 as facet reflectivities and α as the internal loss, then the change in the intensity after one complete roundtrip would be equal to $R_1 R_2 e^{2L(g-\alpha)}$, where L in the length of the cavity. At lasing threshold where the number of lost photons is equal to the number of generated photons by stimulated emission in one roundtrip, we will have:

$$R_1 R_2 e^{2L(g-\alpha)} = 1 \quad (1.3)$$

Threshold gain (g_{th}) calculated from above equation is scaled with a confinement factor (Γ), since the light produced in the cavity is not totally confined to the active region. By further increasing the current density after the threshold condition is satisfied, the gain clamps and carriers participate in recombination process (stimulated emission) to produce more photons.

In this thesis, the gain of active elements is measured by two different methods: Hakki-Paoli and segmented contact method. A brief description of these methods will be presented later in this chapter.

1.1.4 Density of states in semiconductors

In semiconductors the density of states is dependent on the degree and form of carrier confinement. In bulk material, due to a continuum of states in all three dimensions, carriers can potentially have any energy within their band structure. The density of states in bulk semiconductors varies as $E^{1/2}$. By decreasing the size in one dimension significant effects on the density of states are observable. Figure 1.3 plots schematically the density of states for different degrees of confinement in semiconductors.

By quantizing the states in the growth direction (quantum well structures) the carrier motion is limited in that direction. In an ideal quantum well with infinitely deep potential barrier the trapped electrons and holes can have motion perpendicular to the plane of the quantum well only if the thickness of the quantum well is an integer multiple of half motion wavelengths. This restriction is a result of the requirement to have zero amplitude (a node) at the edges of the well. The density of states therefore can be calculated from the available states in the QW plane which leads to a constant (energy Independent) value for each quantised level.

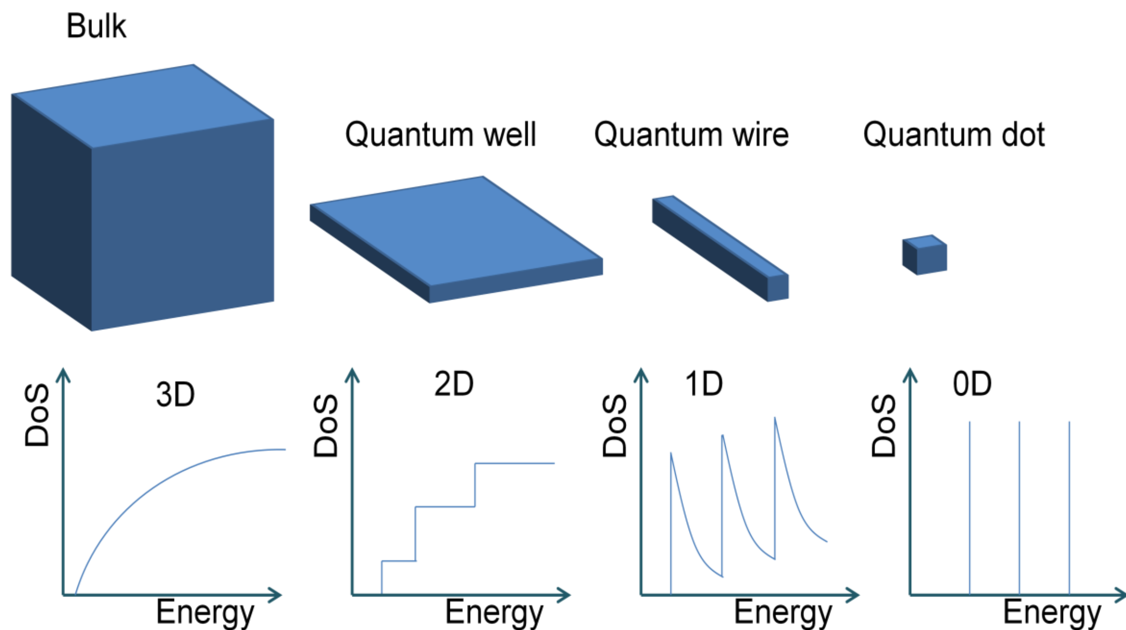

Figure 1.3: Schematic comparison of density of states for different confinement degrees [4].

By decreasing the degree of freedom for carrier motion to one dimension (quantum wire structures) the density of states decreases in comparison with QW structures as shown in figure 1.3. In these structures, the total quantised energy is the summation of individual quantised energies in each confined dimensions. The density of states in one dimensional structures is calculated to vary by energy as $E^{-1/2}$ [5].

In quantum dot structures, carriers are confined in all three dimensions. Unlike bulk, quantum well and quantum wire structures, no continuous energy term exists in quantum dots (since in other structures carriers have freedom of motion in unconfined dimensions) realizing a delta function like density of states. This will lead to a low threshold current density for lasers based on quantum dots and ideally no temperature sensitivity. This concept was proposed by Arakawa *et. al.* in 1982 for semiconductor laser applications [6].

For the formation of quantum dots the Stranski- Krastanow (S-K) method is widely used. In this method, highly strained layers are grown, resulting in the formation of islands having zero dimensional properties. Dots created by this method are not identical in size and composition. This inhomogeneous broadening of the gain and spontaneous emission from the ensemble can be approximated as a Gaussian function [7]. This is schematically plotted in figure 1.4. This broadening results in lower peak gain due to a spread over a wide range of wavelengths. This is disadvantageous for lasers, but makes wider spectral emission possible for applications such as optical coherence tomography.

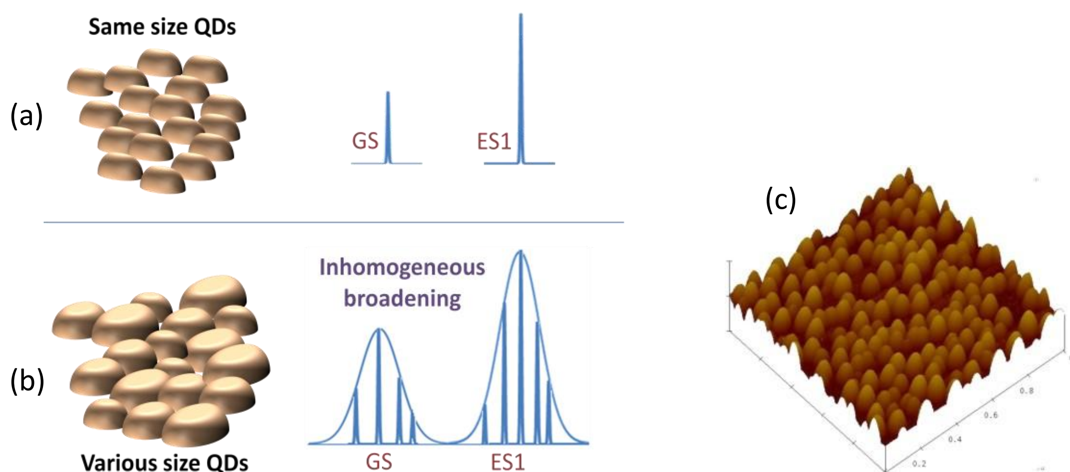

Figure 1.4: (a) Identical size QDs and the resultant delta function like density of states. (b) Self assembled QDs in variable sizes and the resultant Gaussian density of states, (c) real QDs grown by S-K method, courtesy Max Hugues.

In quantum dot structures the size and shape of dots define the electronic structure, i.e. the number of carriers which can be contained, and their confinement energies. The shape of a dot is dependent on the material they are made of and the growth method and conditions. These structures are sometimes referred to artificial atoms due to the similarity of the physics at play.

As explained previously, the confinement of carries results in quantized delta function like energy levels in a quantum dot but in real quantum dots broadening of this transition is expected due to both homogeneous broadening and the previously described inhomogeneous broadening. Homogeneous broadening of the QDs is a consequence of the finite carrier life time, carrier-carrier, and carrier-phonon interactions [8, 9].

1.1.5 QD laser development

The first semiconductor lasers operating at room temperature were commercialized about then years after the first semiconductor laser was introduced by Robert Hall and colleagues at General Electric at 1962. The small size, manufacturability and being electrically pumped were the basic parameters of these type of lasers which attracted attentions to optimize their performance. Reduced threshold current density was achieved in the double heterostructure lasers, by confining the optical mode and carriers in the active region as described earlier.

The advantages of two dimensional active regions over bulk semiconductor lasers were predicted by Dingle and Henry in 1974[10]. More efficient lasing was realized later by quantum well structures benefiting from their step like density of states.

Arakawa and Sakakai predicted improvements in laser performance by introducing the concept of carrier confinement. They theoretically claimed that quantum dots for laser applications will enable a temperature insensitive behaviour of the current density.

In bulk semiconductor materials the carriers can potentially have any energy. Therefore, the emission energy can be increased with any addition of thermal energy (k_BT). However, in QD materials if the energy separation between the discrete levels be more than k_BT, then the thermal energy cannot change the emission energy making the QD laser temperature insensitive. Nevertheless, this is true for ideal QDs, while in reality complete confinement is hardly achievable. The temperature sensitivity of the QD lasers can significantly be decreased by engineering the energy levels to have a large separation between the ground and excited state levels. However, due to the effective mass difference of electrons and holes, the energy levels for holes are closer to each other enabling thermal broadening of the holes and decrease the ground state emission as well as increasing the temperature sensitivity.

Further investigation on QD lasers predicted reduced threshold current density by increasing the quantum confinement in bulk semiconductor which itself enables less power consumption and less heating. It was expected that fewer carriers would be required for population inversion in QDs due to the delta function like density of states, as well as reduced threshold current density and increased material gain [11].

After the prediction of attractive properties of QD materials, almost no progress had been made for a decade due to difficulties in QD fabrication. Numerous attempts have been made in order to realize QD lasers. Quantum box lasers were realized by high resolution electron beam lithography (EBL) and etching process [12]. This technique was not very successful as the wet etching process caused non uniform shapes and very

low number of quantum boxes. Self assembled QDs as the most promising approach to fabricate QD lasers was realized by Kristaedter *et al.* [13] in 1994. In this process three dimensional islands are grown on highly lattice mismatched semiconductors by releasing the strain energy. InAs islands on the GaAs substrate with 7% lattice mismatch was first reported in 1985 by Goldstein [14].

Lots of work has been done toward realizing QD lasers based on GaAs/InGaAs material to replace InP QW lasers which are currently used in 1.3µm wavelength range [15, 16]. The reason is GaAs/InGaAs is much stronger material which makes it easy to grow on larger wafers a well as less sensitivity to temperature due to higher conduction band offsets.

Another step to improve the performance of QD lasers was decrease in the threshold current introduced by dot-in-well (DWELL) structures [17] with increased carrier capture rate due to the QW acting as a reservoir of carriers for the QDs.

Although an ideal QD ensemble with completely identical QDs is not practical but better performance compared to their QW counterparts is still expected from QD lasers. Years later these predicted improvements were realized on 1.3µm QD lasers such as low threshold current density of $19A/cm^2$ for oxide-confined InGaAs/GaAs QD lasers [18], high characteristic temperature of 161k for lasing threshold with p-type modulation doping for temperatures between 0 to 80°C [19], and enhanced small-signal modulation bandwidth of 15GHz and characteristic temperature of 237k at 278K<T<318K [20]. Enhanced optical gain of QD lasers were realized by increasing the QD density and stacking QD layers in growth direction. QD density of $6e10cm^{-2}$ was reported by QDL, Fujitsu Laboratories and University of Tokyo in 2007 [21] for InAs self-assembled quantum dots emitting at 1.3µm.

1.1.6 QDs and free carrier effects – Gaps in knowledge

In order to optimize the desired properties of semiconductor active elements, a fundamental understanding of the carrier dynamics is required. For this reason the energy-band profile of device should be well understood. Bulk, QW and QD systems have different energy levels due to different density of states, Coulomb and carrier-lattice interactions. In bulk semiconductors a continuum of states is available in all three dimensions and in thermal equilibrium Fermi function can provide the probability that an energy level is occupied by an electron. By increasing the confinement from bulk to QW structures, the Fermi probability function can still be utilized to model the behaviour of the carriers in the system. Further increase in the carrier confinement, by moving to in QD ensembles, requires a modified probability function to well explain the carrier distribution in the physically discrete states.

The carrier dynamics in QD ensembles is significantly influenced by its physical parameters such as density, size and composition. These parameters change the energy level of QD states thus the carrier confinement. Moreover, band-gap renormalization, broadening due to intra-dot scattering and Coulomb interactions at high carrier densities make many-body effects of importance for QD system. Due to the small size and limited available electronic stated in QDs, many body effects have significant role even at low carrier densities which can influence the optical properties of the laser. A better understanding of carrier dynamics requires modelling of the physics in QDs. Although during the past years efforts have been made to introduce computational models to explain the carrier distribution in QD lasers, yet a simple model which fits to the physical properties of the QD ensembles is not available. In chapter 2, I will introduce an empirical model to address this requirement. A Monte Carlo model based on

experimental data, that incorporates many-body effects empirically will be explained and be used to predict the gain spectra of QD lasers. Validity of this model is verified by the very good agreement of simulated data and experimentally measured gain of fabricated QD lasers. Incorporating this model different carrier statistics (Fermi-Dirac and Random population), effects of state separation and inhomogeneous broadening of the QD ensemble as well as free-carrier induced energy shifts and broadening are investigated. This model highlights the dominant role of free carrier effects on the carrier distribution function in self-assembled QD lasers.

1.2 QW/QD hybrid structures

The inhomogeneous broadening in QD ensembles made them a promising candidate for high bandwidth applications. By engineering the QD formation process the state separation and inhomogeneous broadening of states can be modified with the aim of achieving broad and flat emission/gain profiles. Due to the increase in degeneracy for higher states in QDs, high carrier density would be required to reach wavelengths attributed to the higher energy levels. This will cause self heating effects. Recently, hybrid QW/QD structures been introduced by incorporating QW layers into the QD active element. The aim was to adjust the excited state of the QW to overlap the energy level of the QD state which is in loss, enabling higher bandwidths for the structure. This complex active structure has shown simultaneously three state lasing but with different sequence which was previously observed in QD only structures.

Grundmann *et al.* theoretically predicted the possibility of two-state lasing in QD lasers [22, 23] with a master-equation model of QD microstates. Years later simultaneous two state lasing was reported in fabricated QD lasers [24] and was attributed to the incomplete clamping of the ES population at the GS threshold which itself was

attributed to the phonon bottleneck in QDs. Following this work, Sugawara *et. al.* studied the effect of homogeneous broadening of optical gain on the lasing spectra in self assembled QD lasers [25]. They experimentally and theoretically investigated the simultaneously two state lasing of the QD laser with ground state starting to lase first followed by the excited state. They calculated the homogeneous broadening of the ground state in 1.3μm self assembled InAs/GaAs QDs to be between 5 and 10meV under the ground state lasing, while it increases up to 20meV under the excited state lasing [7]. This sequence of lasing in QD energy states, starting from the ground state and being followed by the first and second excited state respectively, was also reported in [26].

In chapter 3 I study the EL spectra of hybrid samples to reveal the possibility of an optical pumping process induced by the QW layer to QDs causing the different sequence of lasing from the energy states. A detailed study of these structures is presented in order to determine the role of the QW layer. A QD laser, a hybrid QW/QD SLD and three mesa diodes with different active area structures are fabricated and the characteristics of these devices are discussed. It is shown that emission from the quantum well layer modifies the QD emission.

1.3 Optical coherence tomography

Optical coherence tomography (OCT) is a recently developed imaging technology that can complement conventional imaging techniques. OCT makes it possible to obtain three dimensional (3D) images from live tissues with resolution in the several micrometer range and depth of image in the millimetre range. Being a non-invasive technique to acquire real time data, it can be used in many biomedical applications and is well established in ophthalmology. A range of features of biological tissues such as

structural information, polarization sensitivity, blood flow, elastography, and spectroscopy can be measured by the OCT technique [27].

A comparison of OCT with other medical imaging systems has been summarized in figure 1.5 [28]. Ultrasonography and magnetic resonance imaging (MRI) suffer from poor resolution, yet have deep penetration. Confocal microscopy cannot penetrate deeply into the tissue, but has comparatively high resolution. Having these critical advantages, OCT systems are suited in morphological tissue imaging.

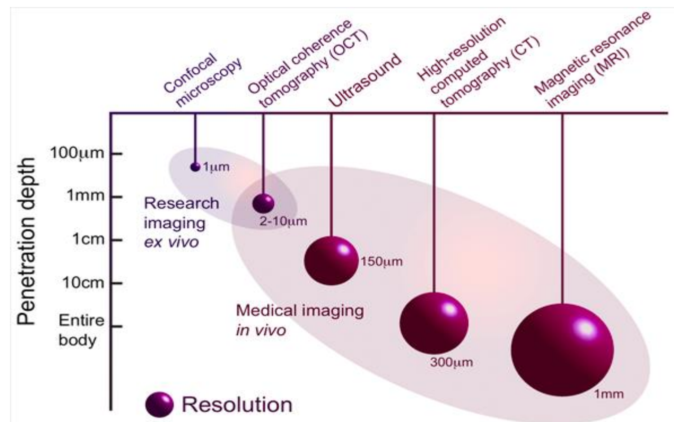

Figure 1.5: OCT in comparison with conventional imaging techniques [28].

The concept of OCT is based on a Michelson interferometer. In this configuration light is split into reference and sample arms. The combination of reflected light from these arms results in an interference pattern. A simple schematic of an OCT system is shown in figure 1.6.

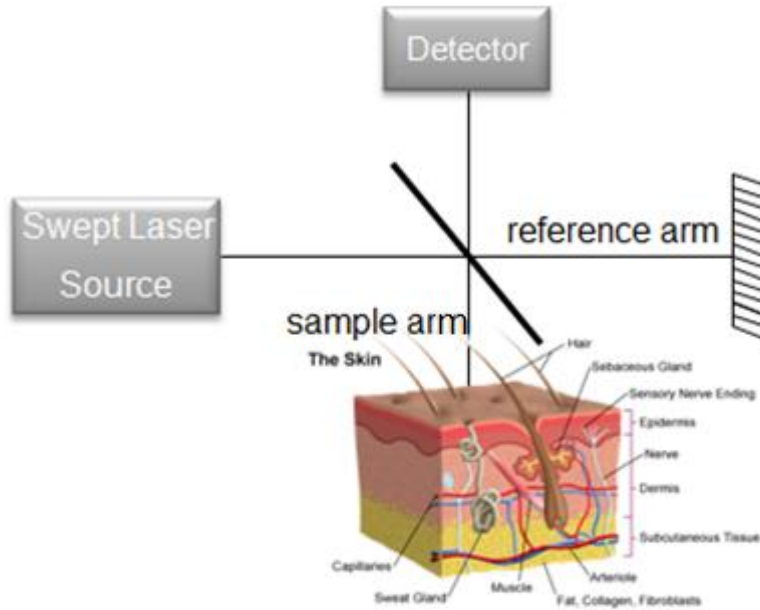

Figure 1.6: Schematic diagram of an OCT system.

The axial and lateral resolutions of OCT images are detached from each other. Axial resolution is determined by the coherence length of the light source. In OCT systems, for a Gaussian spectrum light source the coherence length is defined as [29]:

$$l_c = c\tau = c\,\frac{2\ln 2}{\pi}\frac{1}{\Delta f} = c\,\frac{2\ln 2}{\pi}\frac{\lambda^2}{c\Delta\lambda} \approx 0.44\frac{\lambda_0^2}{\Delta\lambda} \qquad (1.4)$$

Where $\Delta\lambda$ is the 3dB-bandwidth and λ_0 is the center wavelength. Therefore broader bandwidth light sources are required in order to provide shorter coherence lengths and higher resolution. The lateral resolution of OCT images depends on the focusing optics.

OCT systems can be set up in essentially two different configurations: Time domain OCT (TDOCT) and Fourier domain OCT (FDOCT). In TDOCT the mirror in the reference arm moves forward and backward to create the interference pattern while in FDOCT the mirror is held fixed. FDOCT in comparison with TDOCT is dramatically faster and provides superior signal-to-noise ratio [30-33]. Spectral domain OCT (SD OCT) and swept source OCT (SS OCT) were presented by Fercher *et al.* for the first

time [34]. SD OCT systems for skin tissue imaging are expensive as they require array type detectors and high speed cameras (Si detectors make this inexpensive for ophthalmic OCT) while in SS OCT systems only one detector is used. Especially for 1.3μm OCT systems SS OCT is preferred to be used rather than SD OCT because of the availability and cost of detectors [35]. In SS OCT a widely tuneable light source is utilized and the interference is achieved by encoding the optical frequency in time with a fast sweeping light source through a range of frequencies. In this method there is no need to physical movement of the mirror and the axial scan is calculated through a Fourier transform from the obtained spectra, leading to improvements of the signal to noise ratio and the speed of imaging [36].

1.3.1 Active element in swept light sources (SLS)

Active elements in light sources for OCT system can be chosen from different types. Continuous sources such as superluminescent diode (SLD), light emitting diode (LED) and superfluorescent fibers with typical coherence length of 10-15μm, pulsed lasers and scanning sources that can tune narrow-width wavelength over the entire spectrum [37].

Due to their small size and cost, the active element in a swept source cavity is typically a semiconductor optical amplifier (SOA). Wider spectral range of the SOA will provide broader spectral bandwidth for the swept light source, leading to higher resolution in the OCT image [38].

Because of characteristics such as high saturation powers, low noise and high spectral bandwidth, quantum dot (QD) based SOAs have attracted significant attention and became a good candidate for these type of applications [39].

1.3.2 Spectral window for OCT applications

Scattering in tissue and absorption in water are schematically plotted over the range of wavelength in figure 1.7. Different ranges of wavelengths are achievable by GaAs quantum well (QW) and QDs, and InP QWs. Each range can be employed for a specific application. Wavelengths less than 920nm which are currently used for retinal OCT meet the minimum water absorption. Referring to equation (1.4), shorter wavelengths would provide higher resolution, but visible light will make the imaging process appear more invasive for the patient, and the OCT system will experience large dispersion. Devices with 1060nm wavelength combine both moderate scattering and low absorption. At this range dispersion in water is at its minimum value. For skin tissue imaging, wavelengths in the range of 1100 to 1350nm are ideal due to low scattering and moderate absorption in the non-transparent and highly multiply scattering tissue [40]. This range of wavelength can be achieved by InP and GaAs QW and QDs. Broad spectral bandwidth sources can benefit from the broad spectral region of GaAs QDs due to the inhomogeneous QD size, composition distribution and state-filling effects.

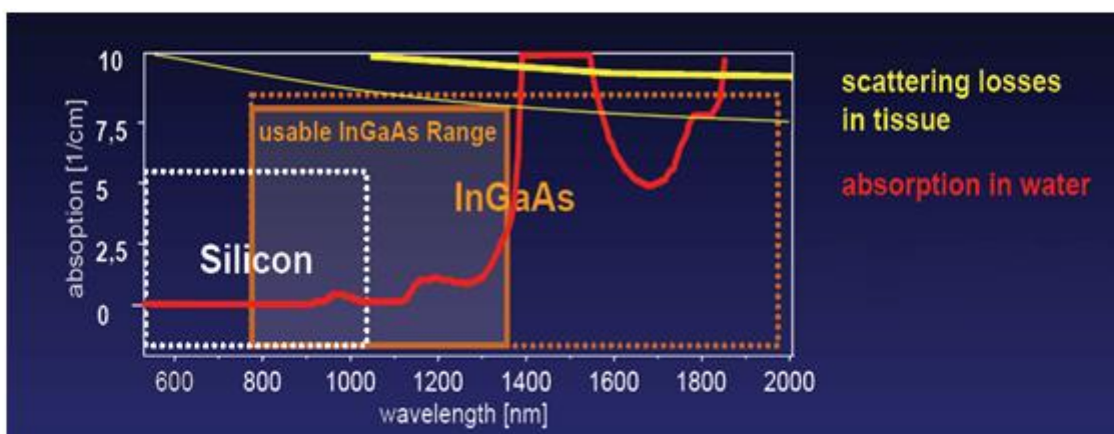

Figure 1.7: Scattering in tissue and absorption in water [41].

1.3.3 QD devices in OCT systems – Gaps in knowledge

As mentioned previously, broadband optical sources are required for high resolution imaging in OCT systems. Due to the inhomogeneous broadening of the QD ensembles they can be a good candidate for this application. The quantum dot size and composition can be engineered in order to achieve control over the emission spectrum. Desired bandwidth can be achieved by multi-layer design where the indium composition or the quantum dot size is varied slightly between layers. In addition to the chirped QDs [42-45], QD intermixing [46] and QD multi-section devices [47] have been studied with the aim of broader bandwidth.

With commercialized QW and QD SOAs being available at different range of wavelengths, we can benefit from the overlapped spectra of these active elements. Just like having separate QW and QD layers in one wafer structure in hybrid QW/QD samples, two SOAs with different wavelength coverage can provide broader bandwidth. Various configurations of QD and QW SOAs can be utilised but the simultaneous operation of these elements needs to be studied. In chapter 4 of this thesis I introduce a range of broad bandwidth light sources implemented by QD and QW SOAs. It will be shown how multiple QD-SOAs in a swept source laser can increase the bandwidth. A spectral coverage of 154nm is achieved by a complimentary QD-SOA and QW-SOA SSL for the first time and the opportunities to increase it up to ~220nm are discussed. Finally, a filtered ASE source with a spectral coverage of 225nm is described and routes to improve this structure have been analysed.

1.4 Experimental methods

In this section I briefly describe molecular beam epitaxy (MBE) as a technique to grow epitaxial structures which is widely used in semiconductor devices manufacturing process. Later, fabrication steps of a multi-section super luminescent diode are described followed by gain measurement methods used in this thesis.

1.4.1 Quantum dot growth - Molecular beam epitaxy

All samples studied in this thesis are grown by MBE [48]. A schematic diagram of a typical MBE system growth chamber is shown in figure 1.8 [49]. In this technique thickness, doping and composition of the layers can be precisely controlled. High quality epitaxial layers are formed inside a high vacuum chamber (less than 10^{-11} Torr), by deposition of molecular beams from thermally evaporated sources on a heated substrate. Extensive in-situ monitoring tools may be employed which makes this method preferable in the growth of complex compound semiconductor structures. Effusion cells usually contain materials like Al, Ga, In, As, Si and Be. Continuous azimuthal rotation (CAR) controls the rotation of heated substrate to ensure a uniform layer of atomic deposition. The atomic beam flux is controlled by beam flux monitor (BFM) and the MBE reactor is kept cold by Cryopanels. For in-situ monitoring, reflection high energy electron diffraction (RHEED) is used. The semiconductor surface crystallography is provided from the reflection and diffraction patterns of the electrons emitted from RHEED gun.

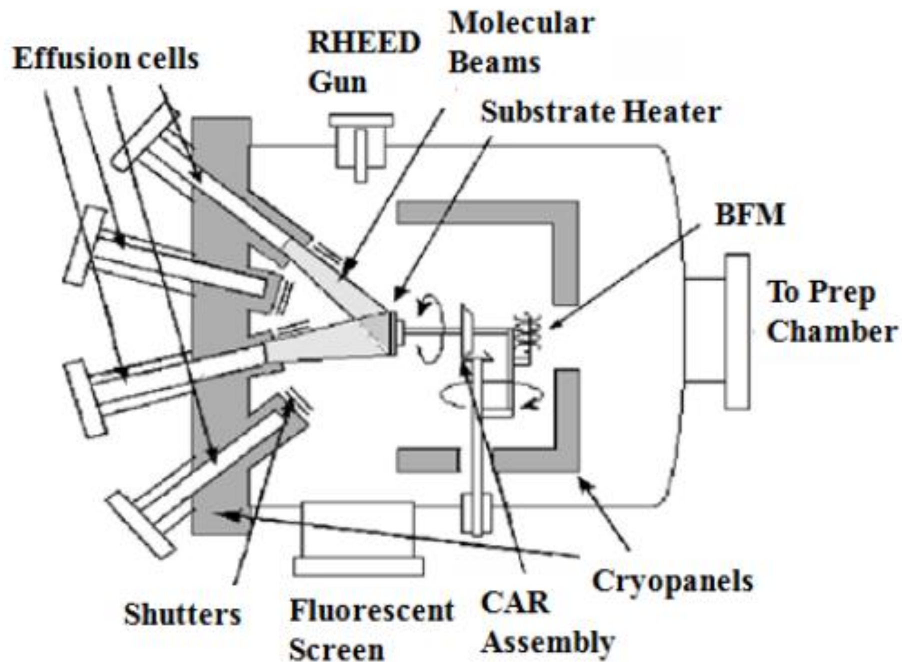

Figure 1.8: Schematic of molecular beam epitaxy (MBE) reactor [50].

1.4.2 Device Fabrication

In this thesis several semiconductor optical devices been analysed. The fabrication process of these devices was based on standard recipes. In table 1.1 I list the main steps of fabrication process which I followed for the multi-section super luminescent diode used in chapter 3. The cross-section of sample at different stages of fabrication is shown in figure 1.9.

	Process	Note
1	Scribe	diamond tipped hand-scribe tool
2	Cleaning	1)n-Butyl 2)Acetone 3)IPA
3	dehydration bake	1min on 100°C hotplate
4	Photolithography with removed edge beads	Trench mask
5	Cleaning the patterned area	O_2 Plasma ash for 1min and 1min at 100°C hotplate

6	Etch	ICP $SiCl_4$	Inductively coupled plasma
7	Check the etch depth	Dektak and SEM	
9	Removing the resist	3min O_2 plasma ash, resist strip	
10	Cleaning	1)n-Butyl 2)Acetone 3)IPA	
11	Si_3N_4 deposition	PECVD 0.5um	plasma-enhanced chemical vapour deposition
12	dehydration bake	1min on 100°C hotplate	
13	Photolithography	Opening SiN window for later metallization	
14	Etch	ICP CHF_3 and Ar	Inductively coupled plasma
15	Removing the resist	3min O_2 plasma ash, resist strip	
16	Photolithography	For metallization	
17	19:1 H_2O Annular Ammonia	to remove the surface oxide before metallization	
18	Metallization	Au/Zn/Au 20/10/200	thermal evaporator
19	Lift off	Acetone	
20	Cleaning the patterned area	O_2 Plasma ash for 1min	
21	Annealing	RTA 360°C 30sec	Rapid thermal anneal
25	Photolithography	Bond pad metallization	
26	19:1 H_2O Annular Ammonia	to remove the surface oxide before metallization	
27	Metallization	Ti/Au 20/200	sputtered
28	Lift off	Acetone	
29	Photolithography	Electroplating	
30	Electroplate	1µm gold	
31	Photolithography	segmentation etch	
32	Au Etch	KI/I2	
33	Semiconductor etch	H_2O_2/Citric Acid	
34	Thinning the backside	thickness: 150um	

35	Backside metallization	InGe/Au 20:200	thermal evaporator
36	Annealing	RTA 360°C 30sec	Rapid thermal anneal

Table 1.1: Fabrication steps for multi section superluminescent diode.

For this process after scribing the wafer, standard three step cleaning was performed (including n-Butyl followed by Acetone and then IPA) on the samples. The first photolithography was carried out to pattern the trenches at both sides of the ridge. The thick photoresist at the edges of the sample was removed prior to the trench exposure (edge bead removal). To clean the exposed area the sample was placed into O_2 plasma asher for 1 minute followed by another 1 minute on 100°C hot plate. Then the samples were loaded into an inductively coupled plasma (ICP) etcher to etch the semiconductor through the active region. After this step the remaining photoresist were washed and the samples went through another cleaning process. The cross section of the device at this stage is shown in figure 1.9(a). The next step is to deposit dielectric on top of the chip followed by another photolithography step in order to open a window on top of the ridge for metal contact on P region. The etch process was performed in ICP and the remained photoresist was cleaned afterward (figure 1.9(b)). After this step samples went through another photolithography followed by thermally evaporated metallization for P contact. After the liftoff process and cleaning the resist, rapid thermal annealing (RTA) was used to anneal the samples (figure 1.9(c)). Same steps were repeated for bond pad metallization (sputtering Ti/Au). The cross section of the chip after liftoff and cleaning process is plotted in figure 1.9(d). 2µm gold layer was deposited afterward on the semiconductor surface after another photolithography for gold bond pads. Last photolithography was performed to create segments on the ridge. First the metal was etched followed by semiconductor etching. At the end the samples were thinned to

150µm and back contact was thermally evaporated for N contact metallization. Another annealing process was performed as the final step.

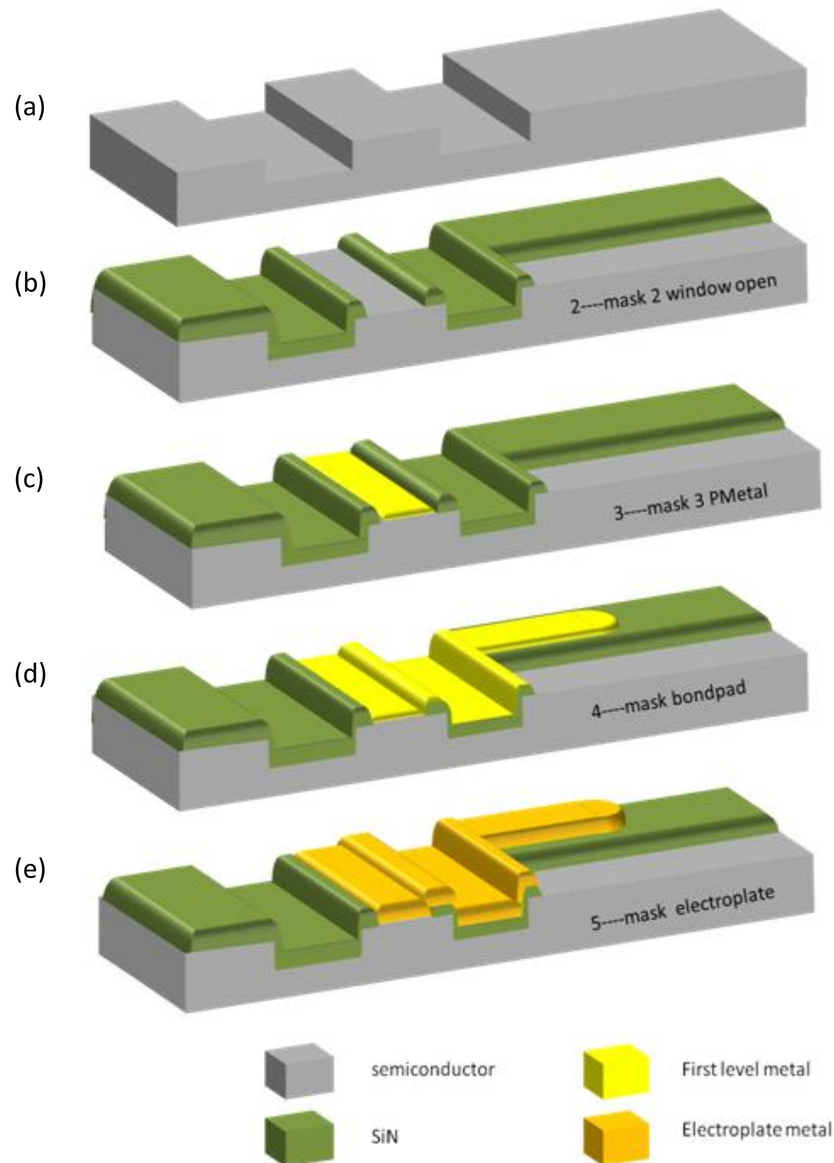

Figure 1.9: Cross-section of multi section superluminescent diode sample at different stages of photolithography. (a) after ridge etch, (b) after opening the window for metallization, (c) after first metallisation, (d) after bond pad metallization and (e) after electroplating.

1.4.3 Hakki Paoli gain measurement method

Introduced in 1975 [51], this method determines the net modal gain of a laser by utilizing individual Fabry-Perot modes below threshold. High resolution spectroscopy is employed to determine the spectral modulation of amplified spontaneous emission due to round trip interference (constructive and destructive) as shown in figure 1.10.

The peak to valley ratio of this modulation allows the determination of the net modal gain of the laser. For this technique short devices are preferred to ensure the full resolution of individual modes.

The difference between the peaks (P_i , P_{i+1}) and valleys (V_i) of consecutive modes in the electroluminescence spectrum is used for net modal gain calculation as:

$$\gamma_i = \frac{P_i + P_{i+1}}{2V_i} \qquad (1.5)$$

$$\text{Gain} = \frac{1}{L}\ln\left(\frac{\gamma_i^{0.5} + 1}{\gamma_i^{0.5} - 1}\right) + \frac{1}{L}\ln R \qquad (1.6)$$

Where L is the length of the laser and R is the facet reflectivity. In this thesis I used an Excel sheet to calculate the gain from the peak and valley values.

Spontaneous emission (SE) of the laser can be derived from the amplified spontaneous emission (ASE) by eliminating the effect of round trip amplification [52]. It can be calculated as:

$$\text{SE} = \frac{P_i V_i}{(\frac{1}{2}[P_i^{0.5} + V_i^{0.5}])^2} \qquad (1.7)$$

The resolution of the optical spectrum analyser (OSA) used for these measurements should be set to a value ensuring full resolution of the modes as plotted in figure 1.10. Using too low resolution will underestimate the gain, whilst too high a resolution will result in low signal to noise and long measurement times.

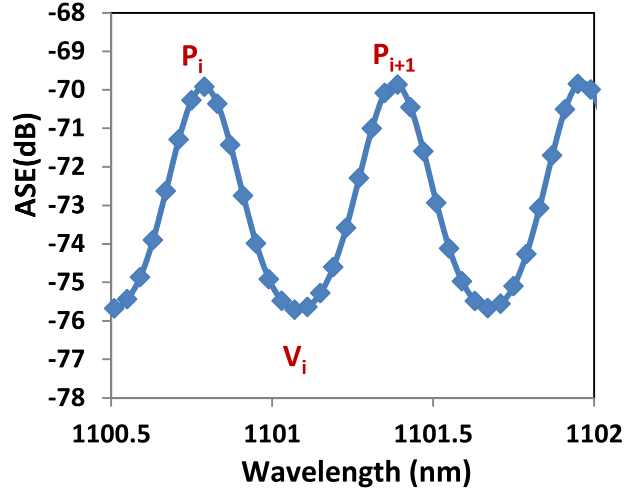

Figure 1.10: Fabry–Perot resonances of an electroluminescence spectrum indicating the peaks and valley.

The Fabry-Perot mode spacing in a cavity waveguide can be calculated as:

$$\Delta\lambda = \frac{\lambda^2}{2nL} \tag{1.8}$$

Where λ is the wavelength, n the refractive index of the waveguide and L is the length of the device. Based on this equation, shorter cavity length devices lead to larger spacing between the modes which makes it easier to fully resolve the individual modes. Moreover for shorter cavity lengths, mirror loss and therefore threshold current are higher which makes it possible to calculate the gain for higher current densities.

On a practical note, beside setting the resolution of the OSA, the number of points measured in the required wavelength range should be adjusted to ensure enough data points are measured within one periodic cycle of the F-P modes.

1.4.4 Segmented contact method

In the segmented contact method the modal gain can be calculated from a multi-section device, as shown schematically in figure 1.11. To prevent the device from lasing, different designs can be implemented. In a tilted waveguide design, the angle between

the light direction and the back facet prevents the reflected light from re-entering the waveguide. In a different design the back facet can be anti reflection coated or an absorber section can be employed to absorb the light coming out of the waveguide and act as an attenuator. This is achieved by either reverse biasing rear contacts, or by leaving them unbiased.

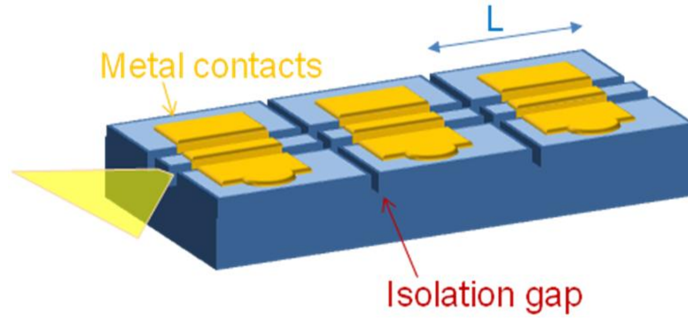

Figure 1.11: Multi section device for segmented contact measurement.

For this measurement only two sections are needed which should be of equal length. First, the section closest to the facet is driven with a current density J and the electroluminescence spectrum is measured. Then the second section together with the first section are both driven with the same current density and the output electroluminescence is measured once more. In this case the first section acts as an amplifier for the light waveguided from the second section. Net modal gain, G, can be calculated from these two sets of data as follows:

$$G = \frac{1}{L} \ln \left(\frac{ASE_{2L}}{ASE_L} - 1\right) \tag{1.9}$$

Where L is the length of a single section of the multi-section device, ASE_L and ASE_{2L} are the amplified spontaneous emissions from section lengths L and 2L driven at the same current density. The spontaneous emission then can be calculated as:

$$SE = \frac{G.ASE_L}{\exp(L.G) - 1} \tag{1.10}$$

References

[1] M. Riordan, L. Hoddeson, “Crystal fire: the invention of the transistor and the birth of the information age.,” USA: W. W. Norton & Company. pp. 88 (1988).

[2] H. Kroemer, "Theory of a wide-gap emitter for transistors", Proc. IRE, 45, 1, 1535 (1957)

[3] Z. I. Alferov, V. M. Andreev, E. L. Portnoy, and M. K. Trukan, "AlAs–GaAs heterojunction injection lasers with a low room-temperature threshold", Fiz. Tekh. Poluprovodn. 3, 1328 (1969)

[4] https:// www2.warwick.ac.uk/ fac/ sci/ physics/ current/ postgraduate/ regs/ mpags/ ex5/ bandstructure/

[5] Bart Van Zeghbroeck, Principles of Semiconductor Devices, University of Colorado (2007)

[6] Y. Arakawa and H. Sakaki, “Multidimensional quantum well laser and temperature dependence of its threshold current,” Appl. Phys. Lett., 40, 939 (1982).

[7] M. Sugawara, N. Hatori, H. Ebe, M. Ishida, Y. Arakawa, T. Akiyama, K. Otsubo, and Y. Nakata, "Modeling room-temperature lasing spectra of 1.3μm self-assembled InAs/GaAs quantum-dot lasers: Homogeneous broadening of optical gain under current injection", J. Appl. Phys. 97, 043523 (2005).

[8] K. Leosson, B. Birkedal, I. Magnusdottir, W. Langbein, and J. M. Hvam, “Homogeneous linewidth of self-assembled III-V quantum dots observed in single-dot photoluminescence”, Physica E 17, 1 (2003).

[9] A. V. Uskov, I. Magnusdottir, B. Tromborg, J. Mørk, and R. Lang, “Line broadening caused by Coulomb carrier-carrier correlations and dynamics of carrier capture and emission in quantum dots”, Appl. Phys. Lett. 79, 1679(2001).

[10] R. Dingle, W. Wiegmann and C. H. Henry, “Quantum states of confined carriers in very thin AlxGa1.xAs.GaAs.AlxGa1.xAs heterostructures,” Phys. Rev. Letts., 33, 14, 827, (1974).

[11] M. Asada, Y. Miyamoto, "Gain and the threshold of three-dimensional quantum-box lasers," IEEE J. Quant. Elect. 22, 1915 – 1921(1986).

[12] H. Hirayama, K. Matsunaga, M. Asada and Y. Suematsu, “Lasing action of Gao,G,lno.33As/GalnAsP/lnP tensile-strained quantum-box laser,” Elect. Letts, 30(2), 142, (1994).

[13] N. Kirstaedter, N. N. Ledentsov, M. Grundmann, D. Bimberg, V. M. Ustinov, S. S. Ruvimov, M. V. Maximov, P. S. Kop'ev, Zh. I. Alferov, U. Richter, P. Werner, U. Gösele and J. Heydenreich, “Low threshold, large To injection laser emission from (InGa)As quantum dots,” Elect. Letts., 30, 17, 1416.1418, (1994).

[14] L. Goldstein, F. Glas, J. Y. Marzin, M. N. Charasse and G. Le Roux, “Growth by molecular beam epitaxy and characterization of InAs/GaAs strained-layer superlattices,” Appl. Phys. Lett. 47, 1099, (1985).

[15] [7]. K. Mukai, N. Ohtsuka, M. Sugawara and S. Yamazaki, “Self-formed $In_{0.5}Ga_{0.5}As$ quantum dots on GaAs substrates emitting at 1.3μm,” Japan. Jrnl. Appl. Phys., 33, 12A, L1710.1712, (1994).

[16] D. L. Huffaker, G. Park, Z. Zou, O. B. Shchekin and D. G. Deppe, “1.3μm room temperature GaAs based quantum dot laser,” Appl. Phys. Letts., 73, 18, 564.2566, (1998).

[17] L. F. Lester, A. Stintz, H. Li, T. C. Newell, E. A. Pease, B. A. Fuchs and K. J. Malloy, “Optical characteristics of 1.24μm InAs quantum dot laser diodes,” IEEE. Photon. Tech. Letts., 11, 8, 931, (1999).

[18] G. Park, O. B. Shchekin, D. L. Huffaker, and D. G. Deppe, “Low-threshold oxide-confined 1.3-μm quantum-dot laser,” IEEE Photon. Technol. Lett., 13, 3, 230–232 (2000).

[19] O. B. Shchekin and D. G. Deppe, “1.3 μm InAs quantum dot laser with To=161 K from 0 to 80 °C,” Appl. Phys. Lett. 80,3277 (2002).

[20] P. Bhattacharya and S. Ghosh, “Tunnel injection $In_{0.4}Ga_{0.6}As$/ $GaAsIn_{0.4}Ga_{0.6}As$/ GaAs quantum dot lasers with 15 GHz modulation bandwidth at room temperature,” Appl. Phys. Lett. 80, 3482 (2002).

[21] M. Ishida, K. Watanabe, N. Kumagai, Y. Nakata, N. Hatori, H. Sudo, T. Yamamoto, M. Sugawara, and Y. Arakawa, 19th International Conference on Indium Phosphide and Related Materials (IPRM2007) FrB1-3, Matsue, Japan (2007).

[22] M. Grundmann, A. Weber, K. Goede, V. M. Ustinov, A. E. Zhukov, N. N. Ledentsov, P. S. Kopev, and Zh. I. Alferov, “Mid-infrared emission from near-infrared quantum-dot lasers,” Appl. Phys. Lett. 77,4 (2000).

[23] M. Grundmann and D. Bimberg, “Theory of random population for quantum dots,” Phys. Rev. B 55, 9740 (1997).

[24] A. Markus, J. X. Chen, C. Paranthoën, A. Fiore, C. Platz, and O. Gauthier-Lafaye, "Simultaneous two-state lasing in quantum-dot lasers," Apl. Phys. Lett. 82, 1818 (2003).

[25] M. Sugawara, K. Mukai, Y. Nakata, and H. Ishikawa, " Effect of homogeneous broadening of optical gain on lasing spectra in self-assembled $In_xGa_{1-x}As/GaAs$ quantum dot lasers ," Phys. Rev. B, 61, 11, 7595-7603 (2000).

[26] Z. Y. Zhang, Q. Jiang, and R. A. Hogg, "Simultaneous three-state lasing in quantum dot laser at room temperature," Electron. Lett., 46, 16, 1155-1157 (2010).

[27] M. Ali and R. Parlapalli, "Signal processing overview of optical coherence tomography systems for medical imaging," Texas Instruments Inc., SPRABB9 (2010).

[28] "Introduction to optical coherence tomography (OCT)," Optical + Biomedical Engineering Laboratory (OBEL) Website, http://obel.ee.uwa.edu.au/research/oct/intro/.

[29] C. Akcay, P. Parrein, and J. P. Rolland, "Estimation of longitudinal resolution in optical coherence imaging," Appl. Opt. 41, 25, 5256-5262 (2002).

[30] R. Leitgeb, C. K. Hitzenberger, and A. F. Fercher, "Performance of Fourier domain vs. time domain optical coherence tomography," Opt. Express, 11, 889 (2003).

[31] J. F. de Boer, B. Cense, B. H. Park, M. C. Pierce, G. J. Tearney, and B. E. Bouma, "Improved signal to noise ratio in spectral domain compared with time domain optical coherence tomography," Opt. Lett. 28, 2067 (2003).

[32] M. A. Choma, M. V. Sarunic, C. Yang, and J. A. Izatt, "Sensitivity advantage of swept source and Fourier domain optical coherence tomography," Opt. Express, 11, 2183 (2003).

[33] S. H. Yn G. J. Tearney, J. F. de Boer, N. Iimia and B. E. Boua, "High speed optical frequency-domain imaging," Opt. express, 11, 22, 2953 (2003).

[34] A. F. Fercher, C. K. Hitzenberger, G. Kamp, and S. Y. Elzaiat, "Measurement of intraocular distances by backscattering spectral interferometry," Opt. Commun., 117,43 (1995).

[35] Y. Yasuno, V. D. Madjarova, S. Makita, "Three-dimensional and high-speed swept-source optical coherence tomography for in vivo investigation of human anterior eye segments," Opt. Express, 13, 26, 10652 (2005).

[36] J. M. Schmitt, "Optical Coherence Tomography (OCT): A Review," IEEE J. Select. Topics Quantum Electron., 5, 1205 (1999).

[37] S. H. Yun, C. Boudoux, G. J. Tearney, and B. E. Bouma, "High-speed wavelength-swept semiconductor laser with a polygon-scanner-based wavelength filter," Opt. Lett.28,1981 (2003)

[38] M. A. Choma, K. Hsu, and J. A. Izatt, “Swept source optical coherence tomography using an all fiber 1300-nm ring laser source," J. Biomed. Opt. 10, 4, 04400 (2005).

[39] T. Akiyama, M. Sugawara and Y. Arakawa, “Quantum-dot semiconductor optical amplifiers,” Proc. of the IEEE, 95, 9, 1757 (2007).

[40] M. E. Brezinski and J. G. Fujimoto, “Optical coherence tomography: high-resolution imaging in nontransparent tissue,” IEEE J. Sel. Top. Quantum Electron., 5, 1185 (1999).

[41] P. E. Andersen, “Optical coherence tomography,” Presentation, FAST-DOT Summer School, Crete, Greece, Sep. 2011.

[42] S. Haffouz, S. Raymond S, ZG. Lu, PJ. Barrios, D. Roy-Guay, X. Wu, JR. Liu, D. Poitras, Z. R. Wasilewski “Growth and fabrication of quantum dots superluminescent diodes using the indium-flush technique: a new approach in controlling the bandwidth,” J Cryst Growth, 311, 1803 (2009).

[43] S. K. Ray, K. M. Groom, R. Alexander, K. Kennedy, H. Y. Liu, M. Hopkinson and R. A. Hogg, “Design, growth, fabrication, and characterization of InAs⁄GaAsInAs⁄GaAs 1.3μm quantum dot broadband superluminescent light emitting diode,” J. Appl. Phys. 100, 103105 (2006).

[44] H. Y. Liu, M. Hopkinson, C. N. Harrison, M. J. Steer, R. Frith, I. R. Sellers, D. J. Mowbray and M. S. Skolnick, “Optimizing the growth of 1.3 μm InAs/InGaAs dots-in-a-well structure,” J. Appl. Phys. 93, 2931 (2003).

[45] Y. C. Yoo, I. K. Han, and J. I. Lee, “High power broadbandsuperluminescent diodes with chirped multiple quantum dots,” Electron. Lett. 43, 1045 (2007).

[46] X. C. Wang, S. J. Xu, S. J. Chua, Z. H. Zhang, W. J. Fan, C. H. Wang, J. Jiang, and X. G. Xie, "Widely tunable intersubband energy spacing of self-assembled InAs/GaAs quantum dots due to interface intermixing," J. Appl. Phys. 86, 2687 (1999).

[47] Y. Xin, A. Martinez, T. A. Nilsen, A. Moscho, Y. Li, A. L. Gray, and L. F. Lester, “1.3 μm quantum dot multi-section superluminescent diode with extremely broad bandwidth (>150 nm),” IEEE Photon. Technol. Lett., 19, 501 (2007).

[48] A. Y. Cho, J. R. Arthur, "Molecular beam epitaxy", Prog. Solid State Chem.Vol.10, 157-192 (1975).

[49] G. Biasiol and L. Sorba, "Crystal growth of materials for energy production and energy-saving applications", Edizioni ETS, Pisa, (2001).

[50] G. Biasiol and L. Sorba, "Crystal growth of materials for energy production and energy-saving applications", Edizioni ETS, Pisa, (2001).

[51] B. W. Hakki and T. L. Paoli, "Gain spectra in GaAs double−heterostructure injection lasers", J. Appl. Phys. 46, 1299 (1975).

[52] B. W. Hakki and T. L. Paoli, "CW degradation at 300K of Ga-As double heterostructure junction lasers. II. Electronic gain", J. Appl. Phys. Vol. 44, no.9, 4113 - 4119(1973).

Chapter 2: Effects of the Carrier Distributions on Quantum Dot Lasers

2.1 Introduction

In this chapter, the effects of free-carrier induced energy shifts and broadening on the carrier distribution function are studied for self assembled quantum dots. I consider different extreme cases for carrier statistics (Fermi-Dirac and random carrier distribution) as well as QD ensemble inhomogeneity and state-separation variation. I introduce a Monte Carlo model to simulate the gain spectra of QD laser material that empirically includes these effects. Based on this model, I compare the simulated results with existing experimental gain measurement data which demonstrated negative differential gain for the first time. Then I provide simulation results of samples with different inhomogeneous linewidth and state separation to show that not only are free carrier effects important at high QD occupancies, but also at much lower carrier densities where QD lasers would normally operate. To confirm this, the effect of free carriers on the profile of gain and spontaneous emission spectrum for QD ensembles are discussed and compared to the effects due to the choice of carrier statistics. A quantum dot device was fabricated and characterized in order to compare the simulation and experimental results, indicating that without the inclusion of the free carriers a good fit was unobtainable. Furthermore, it is shown that the choice of carrier distribution function is far less important than was previously

thought in describing the experimentally observed gain and spontaneous emission spectra.

2.2 Carrier distribution in semiconductor QDs

The band-to-band radiative transitions, stimulated emission, spontaneous emission and absorption were discussed previously in chapter one. The rate of these transitions is dependent on the density of states. The density of states is determined by the material and its geometry but only a fraction of these states are available to participate in the radiative transitions. This fraction is a function of the injection level. For stimulated and spontaneous emission, considered as downward transitions, the rate is maximum when all the electrons are injected into the conduction band (*e.g.* by applying current to a PN junction).

For stimulated emission to occur, the incident photon requires energy (hυ) to be equal to the transition energy. Moreover, momentum conservation needs to be satisfied. For a bulk material these restrictions reduce the transition to a limited region of the E-k diagram of the semiconductor as plotted in figure 2.1 with only transitions in vertical direction [1].

In addition, the transitions can only occur between filled states in the valence band and empty states in conduction band for absorption process and vice versa for spontaneous and stimulated emission processes.

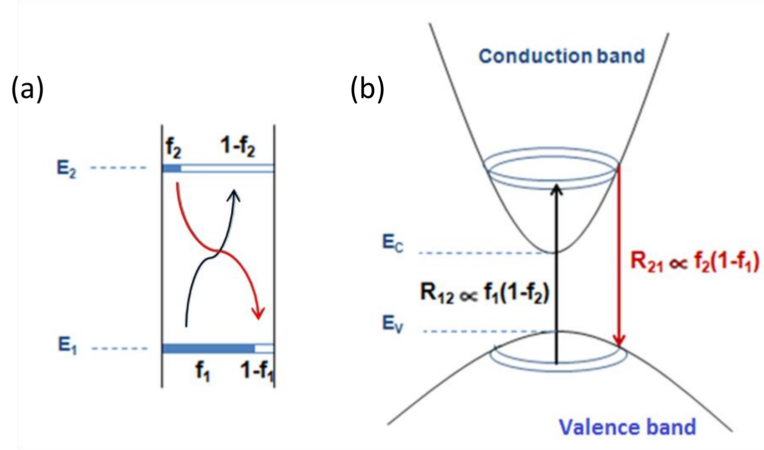

Figure 2.1: (a) In stimulated emission the incident photon requires energy (hυ) to be equal to the transition energy E_{21}. (b) Reduced state pairs due to momentum conservation [1].

In figure 2.1 the rate for upward transitions R_{12} (absorption) and downward transitions R_{21} (Stimulated and spontaneous emissions) are defined as:

$$R_{12} = R_r . f_1(1 - f_2), \quad R_{21} = R_r . f_2(1 - f_1) \qquad (2.1)$$

In these equations R_r is the radiative transition rate with all states available for transition. f_1 and f_2 are the occupation probabilities. From R_{21} and R_{12}, the net generation rate of photons, which is directly proportional to the optical gain in material can be extracted as:

$$R_{net} = R_{21} - R_{12} = R_r . (f_2 - f_1) \qquad (2.2)$$

To define the occupation probabilities, f1 and f2, Fermi-Dirac statistics can provide adequate description of bulk and quantum well structures. Due to spatial carrier localisation in quantum dots some justification needs to be considered for applying the Fermi-Dirac statistics. Thermal equilibrium in QDs can occur at room temperature due to carrier exchange with the wetting layer. However this cannot fully explain the low temperature behaviour of dots where they are populated randomly *i.e.* independent of their energy.

In the case of thermalized carrier population, occupation probabilities can be described using Fermi-Dirac statistics. Considering two quasi Fermi levels for conduction and valence band we will have:

$$f_1(E) = \frac{1}{e^{(E_1 - E_{Fv})/kT} + 1}, \quad f_2(E) = \frac{1}{e^{(E_{Fc} - E_2)/kT} + 1} \qquad (2.3)$$

Where E_{Fc} and E_{Fv} are conduction and valence band quasi Fermi levels.

Alternatively, population probabilities can be defined as being random rather than being described by Fermi-Dirac statistics. Based on the random population, after injection, carriers start to occupy the dots independent of their size and energy levels. In this case, the probability function for the carriers is fixed at a particular value for all energies.

Based on rapid relaxation of carriers into the lowest state there is no luminescence expected from the excited state until the ground state is fully saturated. This is the case for large state separation as compared to k_BT. However experimental results show that there is a carrier population in the ES while the GS is still not full. This phenomenon was initially attributed to the phonon-bottleneck effect [2] which is brought about by the requirement of multiple phonons to relax the carriers to the ground state. There have been theoretical analyses for a random population showing the excited state population before the saturation of the lower states, even for infinitely fast energy relaxation in a QD ensemble [3]. An infinitely fast energy relaxation implies that carriers are always at their lowest possible energy level.

Based on these two carrier distributions, different gain profiles can be calculated. Figure 2.2(a) schematically shows density of states for a QD

ensemble with a state separation of 100meV and ensemble inhomogeneous broadening of 30meV which is wide enough to clarify the effect of occupation function on the gain profile. Considering Fermi-Dirac statistics, the probability function profile can be schematically plotted as in figure 2.2(b) for different quasi Fermi values based on equation 2.3. The gain profile then can be calculated from the emission spectra, simply by the product of density of states and probability function which is plotted in figure 2.2(c). The same graphs are re-plotted for random population in figures 2.2(d) and (e). Since in random statistics there is no preference for the carriers to fill the different size QDs, the probability function would be fixed over the energy for different carrier densities. In all these graphs free carrier effects are not included.

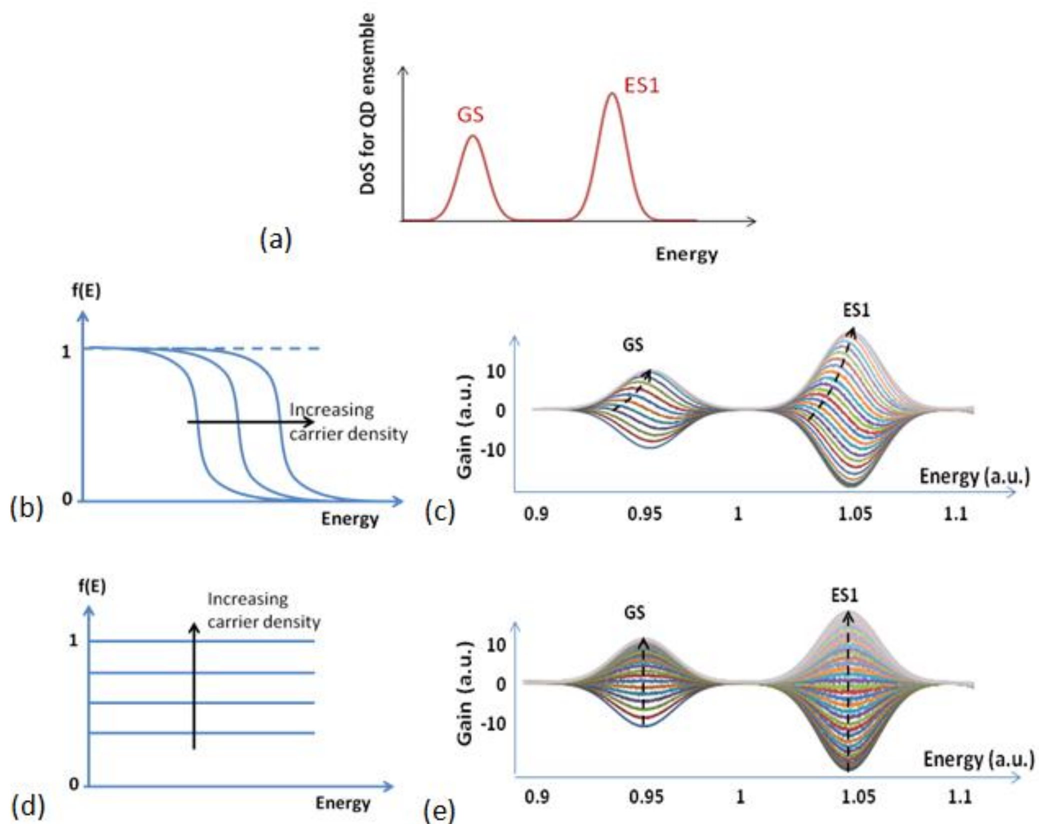

Figure 2.2: (a) Density of states for inhomogeneous QD ensemble with wide state separation, (b) Fermi function as occupation probability (c) gain profile based on Fermi function, (d) random population and, (e) gain profile for random mechanism.

There are clear differences between the two calculated gain profiles. For the random population, there is no change in the peak energy (wavelength) while a clear blue shift in energy can be observed in the case of Fermi-Dirac statistics. Moreover the linewidth in random population is fixed for different injection levels while in Fermi-Dirac statistics there is an increase in linewidth by increasing the injection level. All these differences imply that the choice of carrier distribution in case of no free carrier effects has an important effect in the gain profile.

2.3 Free carrier effects in QDs

In quantum dot structures, by increasing the carrier occupancy the gain spectrum is expected to be influenced by the homogeneous lineshape broadening and energy shift of states [4]. The homogeneous lineshape broadening effect is more significant for QD ensembles with narrow inhomogeneous broadening. The uncertainty of the energy of the electron states, due to the finite lifetime of states, implies that integration over energy is required for gain calculation.

Studies of individual QDs has shown that increasing the number of carriers in QDs raises the linewidth (FWHM) of individual dots due to an increase in the homogeneous broadening [5]. To investigate the effects of excitation density on the linewidth, Matsuda *et.al.* studied individual QDs with different sizes. Figure 2.3 plots the dependence of the linewidth on the excitation power density in three different QDs. It was observed that by increasing the number of carriers within the QDs an additional broadening occurs when the carriers begin to populate the excited state of dots. In self assembled QD structures Coulomb

correlations (carrier-carrier scattering) and phonon-carrier scattering between the confined carriers in QDs and free carriers in the wetting layer constantly alter the instantaneous number of carriers in QDs [6] which results in frequency fluctuations in the ground state transitions. Moreover, by an increase in excitation energy an increased interaction between carriers inside the QDs would lead to an additional increase in the dephasing rate.

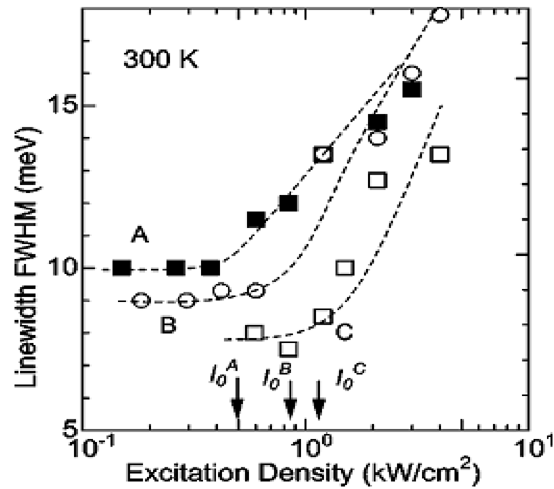

Figure 2.3: Ground state emission linewidth as a function of the excitation density in three different QDs. The dotted lines are a guide for the eyes [5].

Studies of the PL spectra of single quantum dots have also shown an energy shift of the ground state towards lower energy (red shift), as a function of the number of carriers within the QDs [5]. This phenomenon can be explained by bandgap renormalization due to Coulomb interaction between carriers, where the atomic attractive forces are screened out by the carriers. This results in a less localized electron wavefunction and higher overlap with the nearest electron wavefunction. As the larger overlap implies wider energy band, the gaps between bands are reduced leading to shrink in bandgap by increasing the carrier density. Figure 2.4 plots the excitation density dependence of energy shift in a single QD reproduced from Matsuda *et.al.* [5].

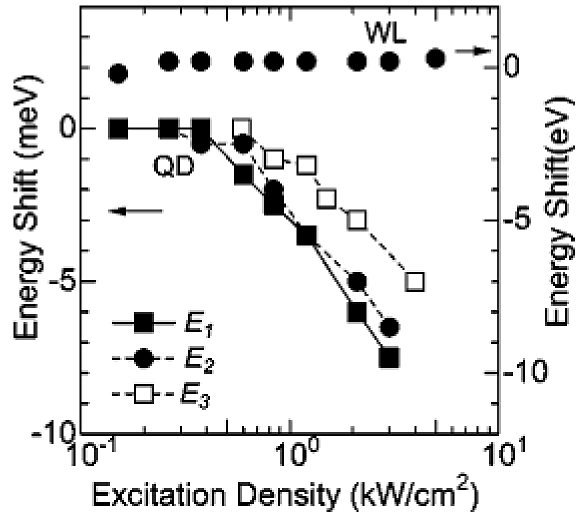

Figure 2.4: Energy shifts of the ground state (E1), and the first (E2) and second excited state (E3) emission of a single QD, and the PL energy of the wetting layer as a function of the excitation density [5].

2.4 Previous work

As discussed in chapter one, quantum dot lasers have attracted significant interest over more than thirty years due to the prediction of temperature insensitivity and enhanced material gain [7, 8]. The importance of the carrier distribution within quantum dot laser materials has been highlighted and discussed widely [9, 10, 11], and can be expected to play a key role in many aspects of the operation of the laser diode.

The requirement of having completely confined states for ideal QD lasers is in conflict with the establishment of a thermal equilibrium within the QD system. Moreover, even in self-assembled quantum dot systems, thermodynamic balance cannot be assumed due to spatially discrete electronic states [12]. The quantum dot parameters such as confinement energy and density of states distribution function make it difficult to accurately define the behaviour of the carrier population.

GaAs based InAs QDs operating at ~1000nm (shallow QDs) have been shown to exhibit a carrier distribution in thermal equilibrium at 300K by extracting the carrier distribution from the shape of the gain and spontaneous emission spectrum, considering the role of energy distribution of the carriers in gain and SE spectral shape [12]. A breakdown in this thermal equilibrium was observed at low temperatures where a random carrier population of isolated quantum dots was observed [13]. The details of the carrier distribution were deduced for these short wavelength InAs/GaAs QDs by taking the ratio of the gain (g) and spontaneous emission spectra (R_{sp}) to determine the carrier distribution function, P_f [13] as written in equation 2.4 (c).

$$R_{sp} = A\rho_c\rho_v f_c(1 - f_v) \qquad (2.4\ a)$$

$$g = \frac{B}{c}\rho_c\rho_v(f_c - f_v) \qquad (2.4\ b)$$

$$P_m = \frac{g}{R_{sp}} = \frac{B}{cA}\frac{(f_c - f_v)}{f_c(1 - f_v)} = \frac{B}{cA}P_f \quad ; \quad P_f = \frac{(f_c - f_v)}{f_c(1 - f_v)} \qquad (2.4\ c)$$

Where R_{sp} is the spontaneous emission, g is the modal gain, A and B are Einstein coefficients, c is the velocity of light, ρ_c (ρ_v) and f_c (f_v) are density of states and probability distribution function for conduction (valence) band, respectively.

For much more deeply confined GaAs/InAs quantum dots operating at 1300nm, a thermalised (Fermi-Dirac) carrier distribution at room temperature was deduced by extracting the gradient of a plot of ln[1-P_m] against emission energy for the excited states of the QD ensemble [13]. As derived in equation (2.4), P_m is defined as the ratio of modal gain and spontaneous emission and is

proportional to P_f. In thermal equilibrium, f_c and f_v are Fermi-Dirac functions, therefore, one can write:

$$\ln[1 - P_f(h\nu)] = \frac{h\nu}{kT_{em}} - \left(\frac{E^*}{kT_{em}}\right) \quad (2.5)$$

Where T_{em} is defined as the temperature at which the occupation population of states are in quasi-equilibrium with each other. E^* is the energy separation of populated electron and holes states participating in the transitions and k is the Boltzmann constant.

Other studies show that a finite carrier capture and relaxation time within the quantum dots has been pointed out to have a significant impact upon the carrier distribution, and that a non-thermalised carrier population is required to explain the appearance of multi-state lasing from the QD ensemble [14]. Moreover, free carrier effects have been shown to shift the gain peak in the QD ensemble [15], and give rise to a negative differential gain at high current densities due to gain saturation, yet continually increasing dephasing effects [16].

The modelling of the evolution of the QD gain spectrum including many-body effects is nontrivial. Koch *et al.* presented a model to describe Coulomb interactions between localised and delocalised states which predicted a ∼20meV redshift in the room-temperature gain peak on the injection of ∼15 electron–hole (e–h) pairs per QD [17]. In this model, dephasing was introduced phenomenologically, with an ensemble-averaged polarisation.

Lorke *et al.* introduced a microscopic theory that makes a full quantum treatment of carrier–carrier and carrier–phonon correlations. This theory has been applied to determine free-carrier effects in a system consisting of an

ensemble of identical QDs [18]. It was pointed out that reproducing experimental findings [5, 19, 20] is problematic as precise knowledge of the specific QD parameters in addition to improvements in this model would be required. Inhomogeneous broadening was subsequently introduced through the statistical averaging of calculated homogeneous gain spectra [21] with an *a priori* assumption of Fermi–Dirac carrier statistics. This approach is described schematically in figure 2.5. In brief, the procedure follows the determination of the confined states, the *a priori* application of Fermi–Dirac statistics, the introduction of many-body effects through single-particle renormalization due to the Coulomb, and the carrier–phonon interactions to give the absorption/gain spectra for an ensemble of identical QDs, which is then broadened with an inhomogeneous linewidth. This approach therefore has great precision in determining the many-body effects on a single QD [22], but dealing with experimentally observed QD inhomogeneity is computationally intensive through this approach. The present approach therefore leads to a non-ideal treatment of inhomogeneous broadening. Furthermore, the digital carrier occupancy of the QDs, where the recombination process does not depend on the average carrier density but only on the particular instantaneous occupancy of the QD [23] is not fully covered. However, more recently, such an approach has been extended to investigate the effect of the position/clustering of indium atoms in QDs of fixed average composition with regard to a negative deferential gain [24]. This approach accommodates some aspects of inhomogeneity present in self-assembled QD ensembles, but is limited to an ensemble of QDs with equivalent indium compositions and sizes.

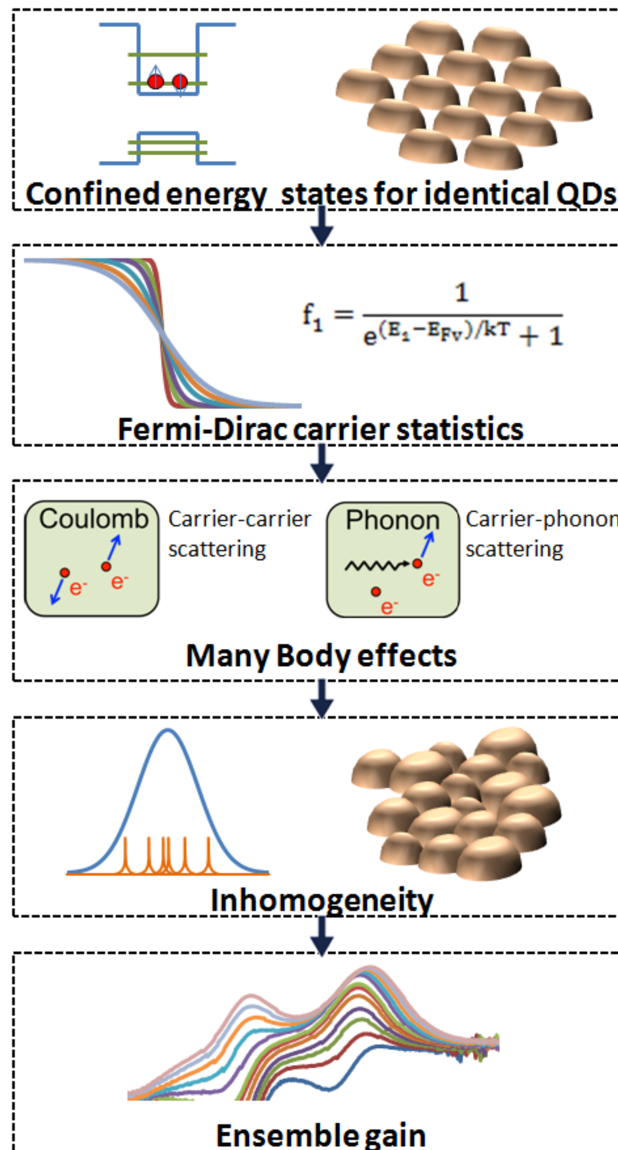

Figure 2.5 Schematic of the approach being used by [18] to determine the gain spectra of QD lasers, where a full quantum treatment of carrier–carrier and carrier–phonon correlations is applied and inhomogeneity is applied at final step.

In 1999, Sugawara et. al. reported the effect of homogeneous broadening on QD laser characteristics in self-assembled InGaAs/GaAs QD lasers [4]. To explain the temperature dependency of the lasing spectra a model was introduced based on a coupled set of rate equations including the size distribution of quantum dots as well as homogeneous broadening effects. This model assumes the carriers occupy the inhomogeneous QDs equally at all temperatures regardless of their size and energy states which can be true only at low temperature where

the carrier filling is assumed to be random. As the temperature increases carriers would prefer to occupy deeper confined dots due to confinement energy dependence for carrier escape. To address this issue, a model including the inhomogeneous size distribution with temperature dependence homogeneous broadening and considering carrier thermal escape was introduced later in [25] considering only the electrons. Based on this model the carrier dynamics of optically pumped QD SOAs to produce broad gain amplification was investigated and the effects of band filling on the gain and refractive index were discussed [26, 27]. A numerical model based on multi-population rate equations analysis were introduced [28] based on electrons and holes taking into account the inhomogeneous QD size distribution as well as the temperature dependence of both the inhomogeneous and the homogeneous broadenings. In this work the static and dynamic characteristics of a QD semiconductor laser was analysed.

Further Analysis of rate equations describing interaction of QW and QDs were discussed in [29, 30] introducing a gain model which includes the QW material gain and QD fluctuations in the conduction band arising from compositional fluctuations of N within the dilute Nitride 1.3µm QW.

2.5 Gap in knowledge

Previous simulation deals with calculations including free carrier effects for a specific ensemble of identical QDs. The inhomogeneity was then applied to the calculations by statistically averaging the homogeneous gain spectra, which requires intense computation to fit this model with experimentally observed inhomogeneity. In order to have a more practical method to simulate QD ensembles, in the next part of this chapter I describe a Monte Carlo model, on

the basis of experimental data, that incorporates many-body effects empirically. I then proceed to simulate the gain spectra as a function of applied current. I adopt this simple empirical approach since a precise reproduction of experimental results through present techniques is known to be difficult[18]. Furthermore, most of the input parameters can be deducted experimentally, with minimal free-fitting parameters, lending confidence to the predicted gain spectra.

Incorporating this model, effects of free-carrier induced shift and broadening on the carrier distribution function are studied considering different extreme cases for carrier statistics (Fermi-Dirac and random carrier distribution) as well as quantum dot (QD) ensemble inhomogeneity and state-separation using the introduced Monte Carlo model. Using this model I show that the dominant factor determining the carrier distribution function is the free carrier effects and not the choice of carrier statistics. Using empirical values of the free carrier induced shift and broadening, a good agreement is obtained with experimental data for QD laser materials obtained under electrical injection for both extreme cases of carrier statistics.

2.6 Monte Carlo model

The procedure I adopt is shown schematically in figure 2.6. This contrasts that adopted previously, shown in figure 2.5. I consider an ensemble of 10^6 QDs with a ground-state energy distribution following a Gaussian envelope with a FWHM representing the inhomogeneous distribution of QD size and composition.

A constant ground state and excited state (GS–ES) separation for all the QDs is assumed owing to the observation that the widths of the ground, first, and second excited states are almost identical. This comes about during the formation of the QDs in that the larger QDs are found to contain more indium since they represent a reduced surface energy for indium incorporation relative to the smaller QDs.

The width of the Gaussian envelope can be determined experimentally from absorption measurements or PL/EL measurements at a very low QD occupancy, which provides a measure of the inhomogeneous broadening (which is dominant) and homogeneous broadening due to phonon scattering. The state separation can also be determined by, for example, absorption spectroscopy and/or high-excitation PL/EL measurements. At this stage I apply carrier statistics to the ensemble of QD states.

In the case of Fermi–Dirac statistics, the QD array is filled using a Fermi probability distribution until the required average QD occupancy (average number of e–h pairs per QD) is achieved. In the case of a random carrier distribution, the QDs are filled randomly (regardless of energy and previous occupation – via Poisson statistics) until this required average QD occupancy is achieved.

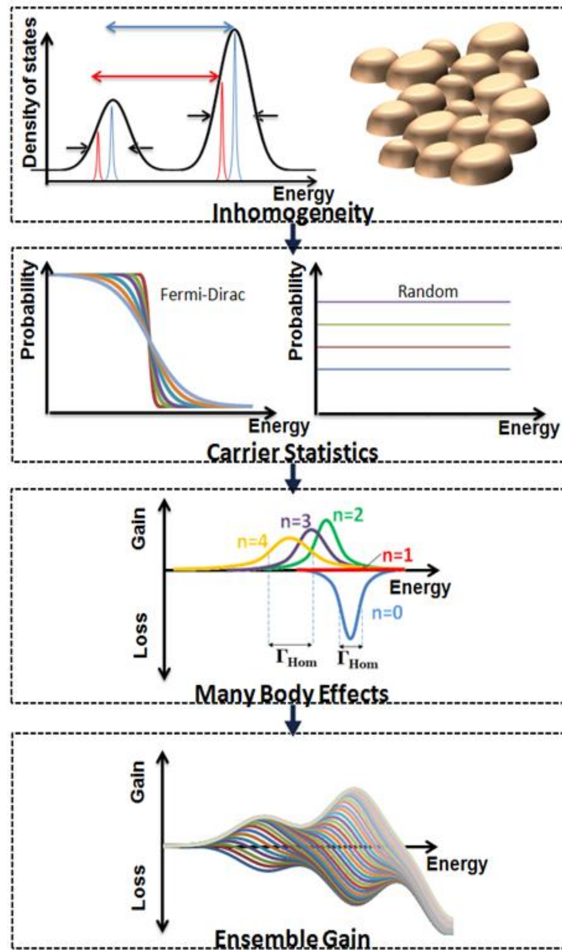

Figure 2.6. The procedure being used here to determine the gain spectra of QD lasers.

Based on the discrete Poisson distribution, the probability of QD occupancy as a function of average dot occupancy, <n>, can be plotted as figure 2.7.

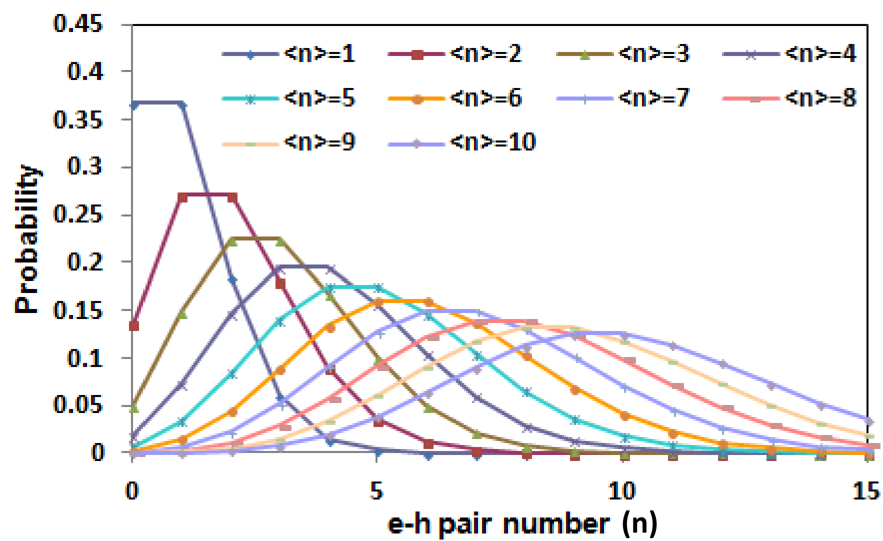

Figure 2.7: Poisson carrier distribution as a function of average QD occupancy.

In both cases, I assume a geminate population with charge neutral QDs. The microstate of the QD [23] is determined by considering the thermal energy of the carriers with regard to the state separation. Instantaneous carrier relaxation is therefore considered, which is a reasonable approximation in terms of the relative magnitude of the carrier (~ns) and relaxation lifetimes (~10 ps). Once this is completed, I have a QD array where each QD has a specified instantaneous occupancy.

I then introduce many-body effects on the emission properties of the microstates of the QDs. This is shown schematically in figure 2.8. Each QD is assumed to have the same recombination lifetime and oscillator strength. A renormalization shift and additional inhomogeneous broadening to the gain/spontaneous emission of each QD based on its instantaneous occupancy is then introduced. Both effects are assumed to be linear in carrier density, which is generally found in both theory [17, 21, 31] and experiment [5].

For zero occupancy, the QD ground state contributes only in absorption. With one e–h pair in the ground state, the QD is transparent (as absorption and stimulated emission have equal probabilities), and finally, gain is obtained with 2 e–h pairs. In this case, the integrated gain is assumed to be the same as the integrated absorption with 0 e–h pairs. However, the maximum gain will not be equal to the maximum absorption owing to the many-body effects causing additional broadening and a renormalization shift to the transition energy, as described previously. This shift and broadening continue as more carriers are added to the QD owing to the continuously increasing dephasing yet saturated

GS gain. This is the origin of the negative differential gain observed in QD systems [16, 21].

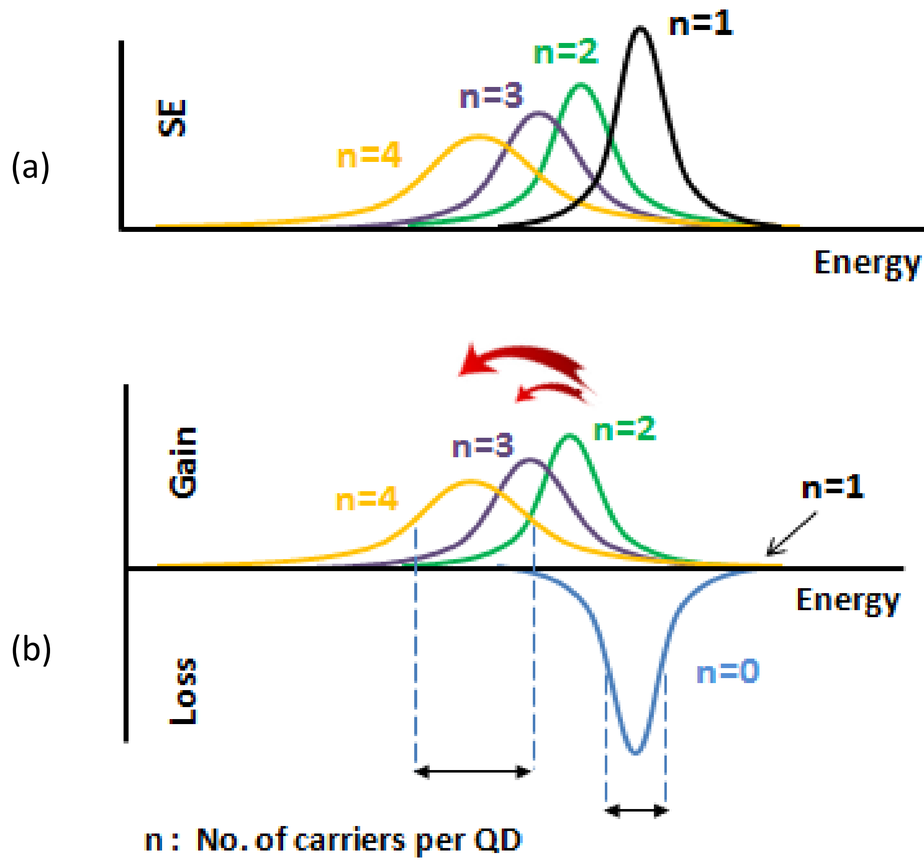

Figure 2.8: Schematic of (a) emission and (b) gain and loss in one single quantum dot for various numbers of carriers per dot.

In this model no lattice distortion is assumed, therefore the emission from QD with one carrier would be at the same energy as that of absorption (i.e. there is no Franck-Condon shift). Having sufficient statistical information of QD size and compositions in the actual sample would increase the accuracy of the model but would require a considerable number of high resolution transmission electron microscopy (TEM) and energy-dispersive X-ray (EDX) measurements [32].

From measurements on individual QDs, the homogeneous linewidth is found to be a function of both temperature and carrier density [4, 5]. Here I assume that the sample temperature is constant at 300K, and neglect both Joule heating and the transfer of the energy from the carrier to the lattice as it relaxes into the QD. It is worth noting that since this relaxation heat is deposited directly into each QD, it will be responsible for local effects over short timescales. However, as long as we only consider the steady state, then this can be neglected since the carrier lifetime is long (nS) relative to the relaxation time (pS). The homogeneous linewidth is approximated as a Lorentzian broadening, and due to the infinite tails of the distribution, it is truncated to neglect the extreme ±2% of the distribution for computational simplicity.

The gain in each QD is calculated by summation across the entire ensemble to yield the gain spectrum. The saturated ground state gain (G_{max}) is used to calibrate the model and is measured from multi-length FP measurements. Details of calculation used in this model are summarized in Appendix 1.

In the rest of this chapter three QD ensembles will be analysed with this model. Table 2.1 provides a summary of these samples.

Sample	Source	Inhomogeneous linewidth(meV)	State separation (meV)
Ensemble A	Innolume GMBH	42	85
Ensemble B	University of Sheffield	41	60
Ensemble C	QD laser Inc.	31	90

Table 2.1. Summary of the samples studied in this chapter.

2.7 Comparison with existing data

In order to compare the model to the experimental results, the gain spectrum obtained from a commercial QD material (Innolume GMBH), Ensemble A, was studied (courtesy Dr. Hifsa Shahid) [16].

The quantum dot laser structure was grown by molecular beam epitaxy and consisted of 10 QD layers. Figure 2.9 shows the epitaxial structure of the wafer with 1.5μm $Al_{0.35}Ga_{0.65}As$ as n-cladding layer, 10 repeats of 33 nm GaAs, InAs QDs, and 5 nm $In_{0.15}Ga_{0.85}As$ strain reducing layer followed by 1.5 nm $Al_{0.35}Ga_{0.65}As$ p-cladding and a 200 nm heavily doped p^+ GaAs contact layer.

Fabricated lasers on this wafer had 3μm width by 300and 450μm lengths. Hakki Paoli gain measurement at very low current densities (≪1e–h pair per QD) allows the determination of the inhomogeneous broadening (42meV) and state separation (85meV). A homogeneous broadening of the individual QD state 5meV is assumed [5]. A shift between the absorption minimum at a low current density and the gain peak at a gain saturation of ~12meV is observed. This is in line with similar experiments on 1.3 μm bi-layer QD lasers, which showed a ~10meV shift between absorption minima and gain maxima [16]. The GS gain as a function of current density of this laser is shown in figure 2.10.

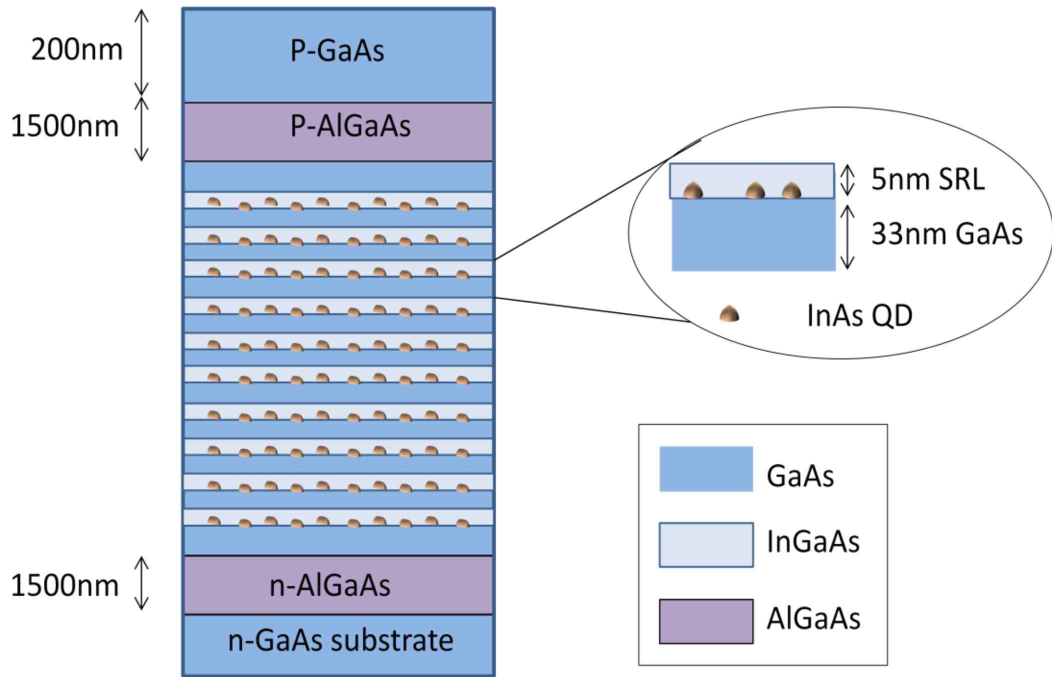

Figure 2.9. Wafer epitaxial structure of Ensemble A.

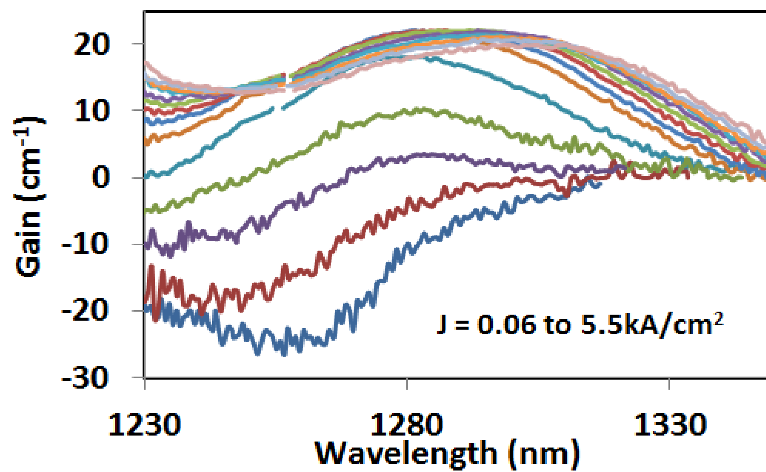

Figure 2.10: Hakki–Paoli measurement of gain spectra of Ensemble A.

GS gain saturation can be expected at average carrier occupancies of ~2–3e–h pairs per QD providing a free-carrier shift of ~3–6meV per e–h pair. Such shifts for the ensemble are in agreement with theoretical calculations [31] and single-QD spectroscopy results [5] which give ~2–3meV/e–h pair for the renormalization shift. All the values are in line with those expected for bulk band-gap renormalization, given the small volume of the QD [33]. The increase

in homogeneous linewidth with increasing QD occupancy has also been measured to be ∼1meV/e–h pair. Note that these reports having low values for the free-carrier renormalization shift per e–h pair were for short-wavelength (i.e., less highly confined) QDs.

I now go on to discuss the simulated gain spectrum based on the input parameters described above in the case of the two extreme cases for the carrier occupancy: Fermi–Dirac statistics and a random carrier distribution. Figure 2.11(a) shows experimentally obtained [16] and simulated curves using a Fermi–Dirac carrier distribution. Figure 2.11(b) shows the same experimental data with simulated gain curves using a random carrier distribution. In both cases, I adopt typical mono-molecular, bimolecular, and Auger coefficients to convert between average numbers of e–h pairs per QD and carrier density [34].

Note that a reasonable fit is obtained in both cases, but with a much closer fit being obtained in the case of a random carrier population. However, I find that free-carrier effects dominate the form of the gain spectrum rather than the choice of carrier statistics. The empirical values for band-gap shift and transition broadening are shown to naturally lead to a negative differential gain for both carrier statistics. In the case of a Fermi–Dirac carrier distribution, an oscillation in the peak gain of the GS is observed, in contrast to the monotonic reduction in peak gain in the case of a random carrier distribution.

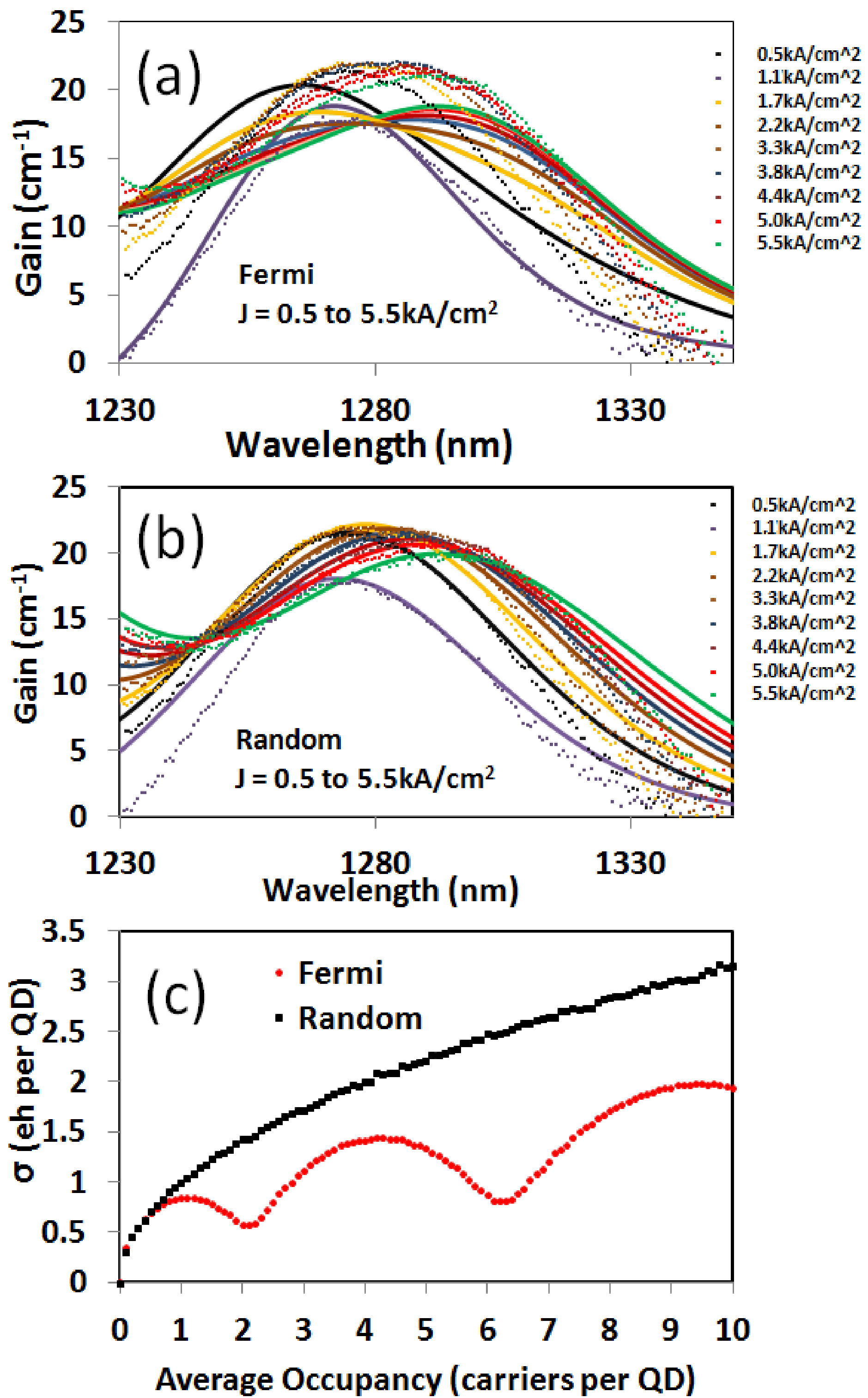

Figure 2.11. Simulation results for (a) Fermi–Dirac statistics and (b) random population of QDs in Ensemble A. The dotted lines are the measured data and the solid lines are the simulated fitted data. (c) Standard deviation in carrier occupancy amongst the QDs in the ensemble as a function of average carrier occupancy.

In order to understand the physical origin of this oscillation in the simulated ensemble gain, figure 2.11(c) shows the standard deviation in carrier occupancy amongst the QDs in the ensemble as a function of average carrier occupancy. For Fermi–Dirac carrier statistics, we observe local minima at average QD occupancies of 2, and 6 e–h pairs per QD. These values correspond to a full ground state and an excited state, respectively. This reduction in sigma is driven by the carrier thermalisation process and the energy jump to populate the excited state. As the average carrier occupancy approaches 2, the excited state is preferentially filled before proceed to fill the excited state of each QD. The precise form of this oscillation is driven by the state separation and inhomogeneous linewidth. As a consequence, the shift of the ensemble gain peak (driven by the instantaneous carrier occupancies and their standard deviation) is considerably more digital in the case of a Fermi–Dirac carrier distribution. This leads to the oscillations in the peak ensemble gain in our model. Such oscillations have not been predicted owing to the effects of inhomogeneity being applied after the Fermi–Dirac carrier statistics [21]. A possible reason why this effect has not been seen experimentally is that, as the QD carrier occupancy rises, the electron–electron scattering may dominate, making carrier escape from the QDs insensitive to the confinement potential. Note, however, that the integrated modal gain for a full ground state is similar to the integrated modal loss of an empty ground state, in agreement with similar measurements on QD bilayer structures [16]. This suggests that a large reduction in QD occupancy with increasing carrier density is unlikely (in addition to continued excited-state saturation). However, a mixture of carrier statistics between Fermi–Dirac and a random population has been pointed out to

be required in order to explain the appearance of multistate lasing from the QD ensemble [14]. This hybrid situation will act to obscure these oscillations by allowing a larger variation in occupancy for each QD in the ensemble, as would a state separation of <2 kT.

I also note a comparatively poor fit to a long-wavelength tail of the ensemble gain spectrum in both cases. A purely Gaussian QD size/composition distribution in the ensemble was assumed, which is a good but not perfect approximation of the real ensemble, where in some cases even bimodal distributions are seen [35]. Additionally, I assume that the renormalization shift and additional broadening are identical for each QD. Long-wavelength QDs will generally have a different size shape and composition as compared with short-wavelength QDs, so this assumption is not necessarily valid [24].

In addition to a more accurate treatment of carrier–carrier and carrier–phonon interactions in producing renormalization shifts and additional homogeneous broadening, full treatment of carrier scattering in determining the precise carrier distribution is required. A measurement of the carrier lifetime [34] whilst simultaneously measuring the gain spectrum would be a powerful tool for understanding and predicting the gain spectrum. Considering these approximations and the few fitting parameters employed, the quality of agreement in Fig. 2.11(b) is suitable for predicting a number of phenomena for real devices in a computationally efficient model.

2.8 Comparison of incorporating free-carrier effects for samples with varying inhomogeneous linewidth and state separation

In this section I describe simulation results which explore the effect of the free-carrier induced shift and broadening on the carrier distribution function. The different extreme cases for carrier statistics (Fermi-Dirac and random carrier distribution), QD ensemble inhomogeneity and state-separation are explored. I show that not only are free carrier effects important at high QD occupancies [16], but also at lower carrier densities where QD lasers would normally operate. I conclude that the free carrier effects dominate the form of the gain and spontaneous emission spectrum for the QD ensemble, and hence the carrier distribution function, rather than the carrier statistics.

2.8.1 Ensemble B

2.8.1.1 Simulation results without free carrier effects

To explore the influence of QD state separation and inhomogeneous linewidth on the distribution function, the carrier distribution function for an ensemble of QDs with inhomogeneous linewidth of 41meV and state separation of 60meV [36], termed Ensemble B was calculated. Resultant gain and SE are plotted in Figure 2.12(a) and (b) for Fermi-Dirac and 2.12(c) and (d) for random carrier distribution.

The modal gain divided by SE for this sample is plotted in figure 2.13 for the two extreme cases for carrier statistics. It is observed that for the Fermi-Dirac statistics the distribution is less modulated in the transition region between ground and excited state.

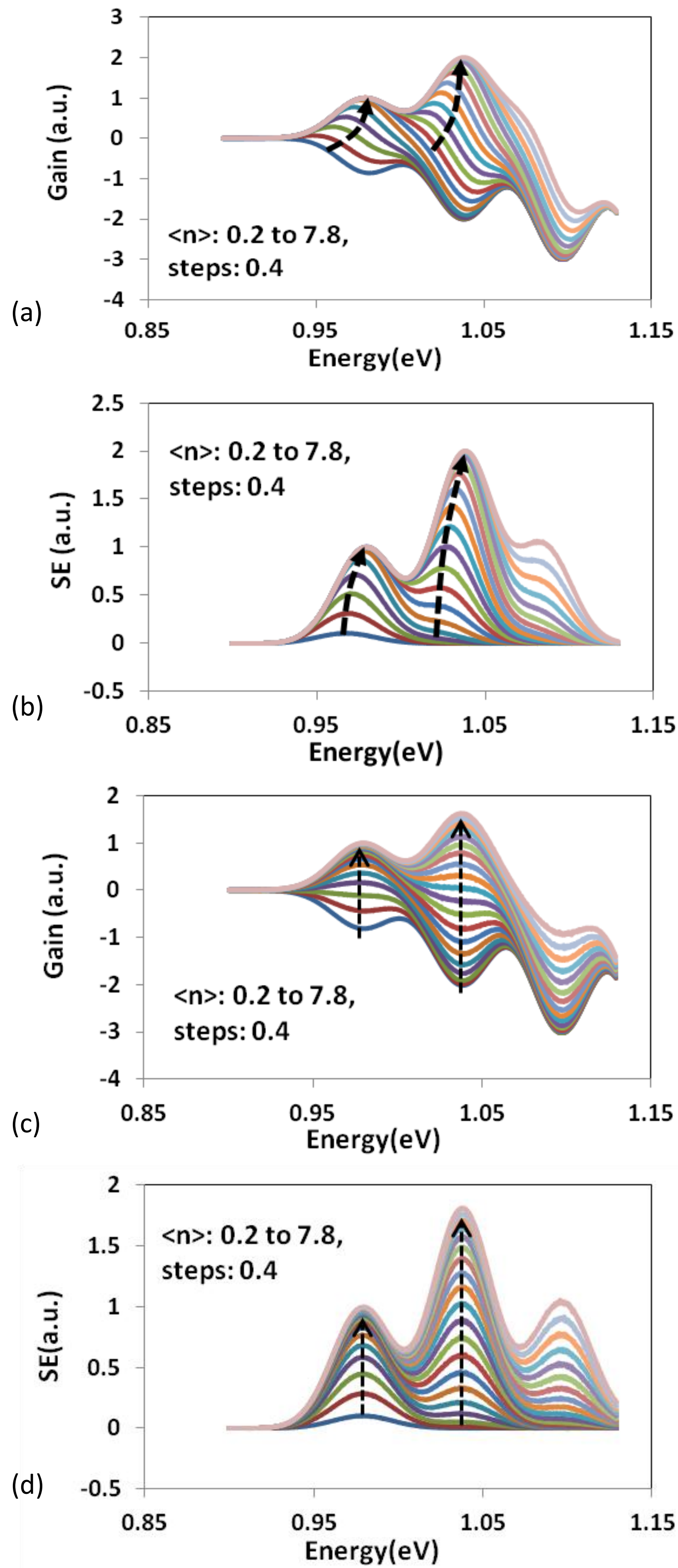

Figure 2.12: (a) Gain and (b) SE of Ensemble B for Fermi-Dirac carrier statistics. (c) gain and (d) SE of the same sample for random carrier distribution.

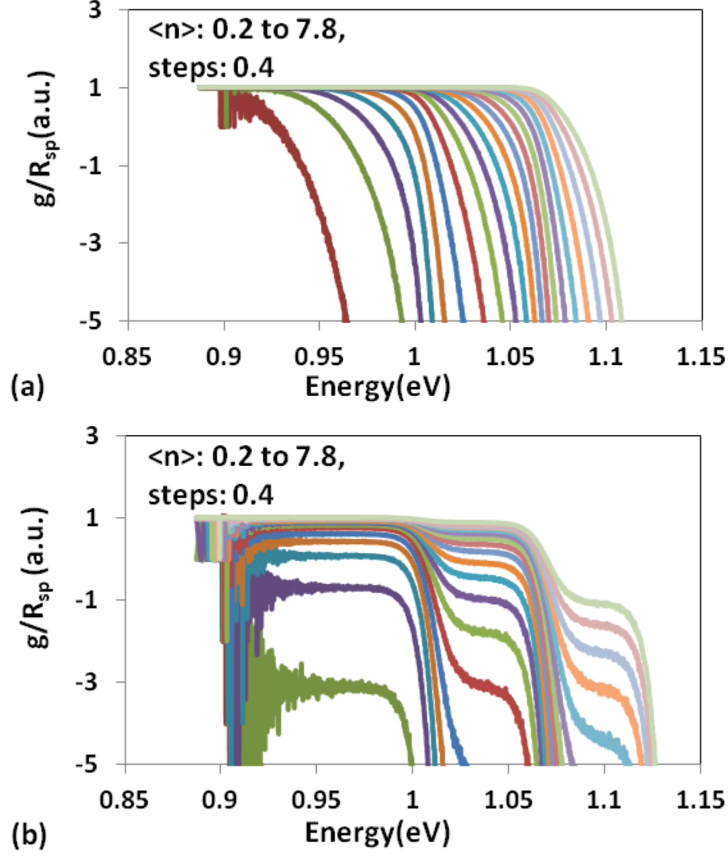

Figure 2.13: Gain divided by spontaneous emission rate of Ensemble B for (a) Fermi-Dirac and (b) random carrier statistics at 300K.

2.8.1.2 Simulation results including free carrier effects

I now introduce an empirical values for the energy shift and homogeneous broadening of individual QD emission as a function of carrier occupancy deduced from experimental observations, [5, 37] which are also in agreement with theoretical predictions [17, 21, 31]. As in the previous discussions, I considered a homogeneous linewidth with no free carrier effects of 5meV at 300K. In addition, a homogeneous broadening dependent on carrier density of 1meV per carrier per QD was included as observed experimentally [5]. The bandgap shrinkage is calculated using bulk values of 32meV/(10^{18} $cm^{-3})^{1/3}$ [1] which is in good agreement for both bulk and quantum well material [38, 39, 40]. A QD volume of 10 x 10^{-18} cm^{-3} was used.

Incorporating these values into the model, the gain and spontaneous emission spectra were recalculated and are plotted in figure 2.14(a, b) for Fermi-Dirac and (c, d) random carrier statistics at 300K for Ensemble B. Comparing the results the gain and spontaneous emission profiles look very similar for Fermi-Dirac and random statistics.

2.8.2 Ensemble C

2.8.2.1 Simulation results without free carrier effects

Figure 2.15 plots the modal gain (a) and spontaneous emission (b) of an ensemble of quantum dots with inhomogeneous linewidth of 31meV and state separation of 90meV (Ensemble C) for Fermi-Dirac carrier statistics at room temperature whilst that of the random carrier distribution, is plotted in (c) and (d). The influence of free carrier effects is not considered in these simulations. The values of state-separation and inhomogeneous linewidth were measured using Hakki-Paoli method as in chapter one from commercial QD laser material discussed later in this chapter.

For Fermi-Dirac statistics the distribution is a function of energy (QD size) with a preferential occupation of deeper confined dots due to a confinement energy dependence for carrier escape. By contrast, for random carrier statistics, rapid/continuous carrier escape and capture is not included, and all QDs have the same carrier distribution function.

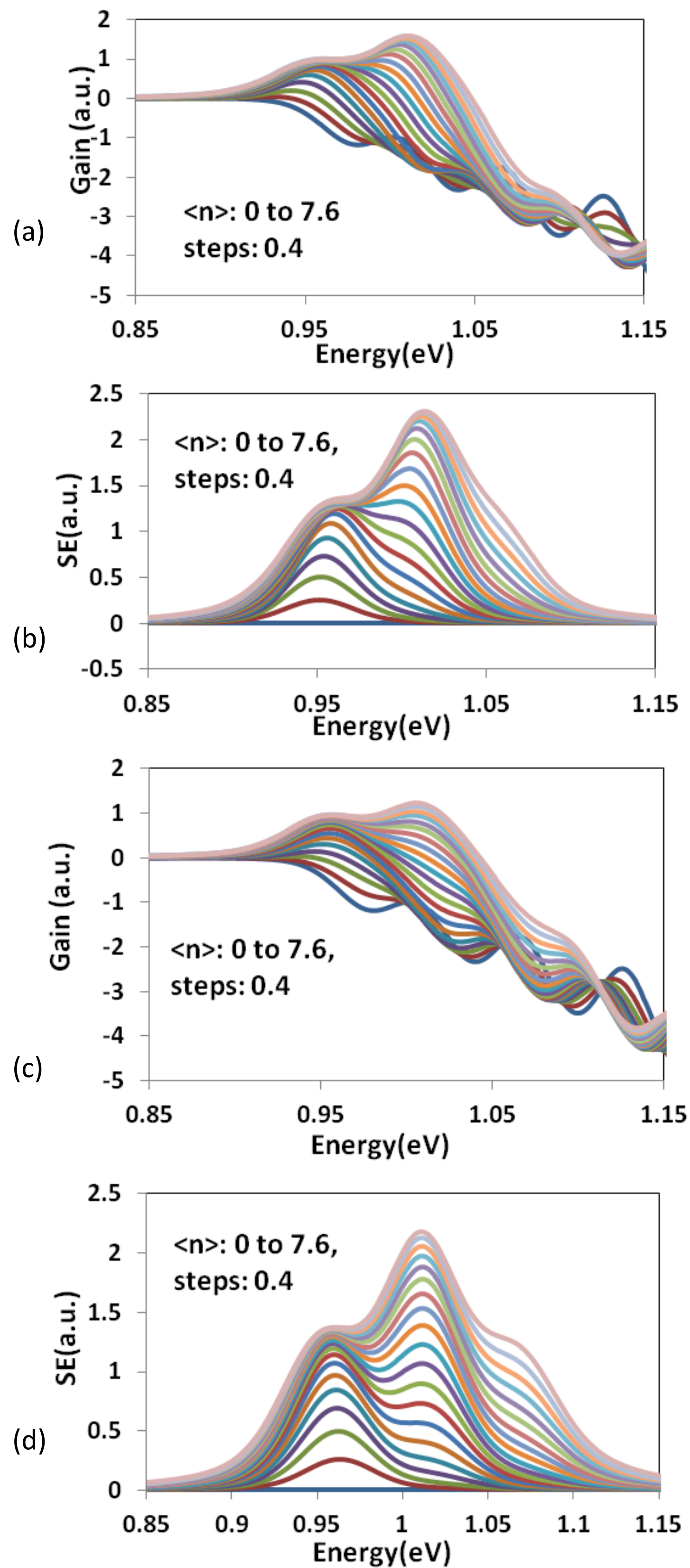

Figure 2.14 (a) Gain and (b) SE for Fermi-Dirac at 300K for Ensemble B including free carrier effects. (c) Gain and (d) SE for random carrier statistics for the same sample.

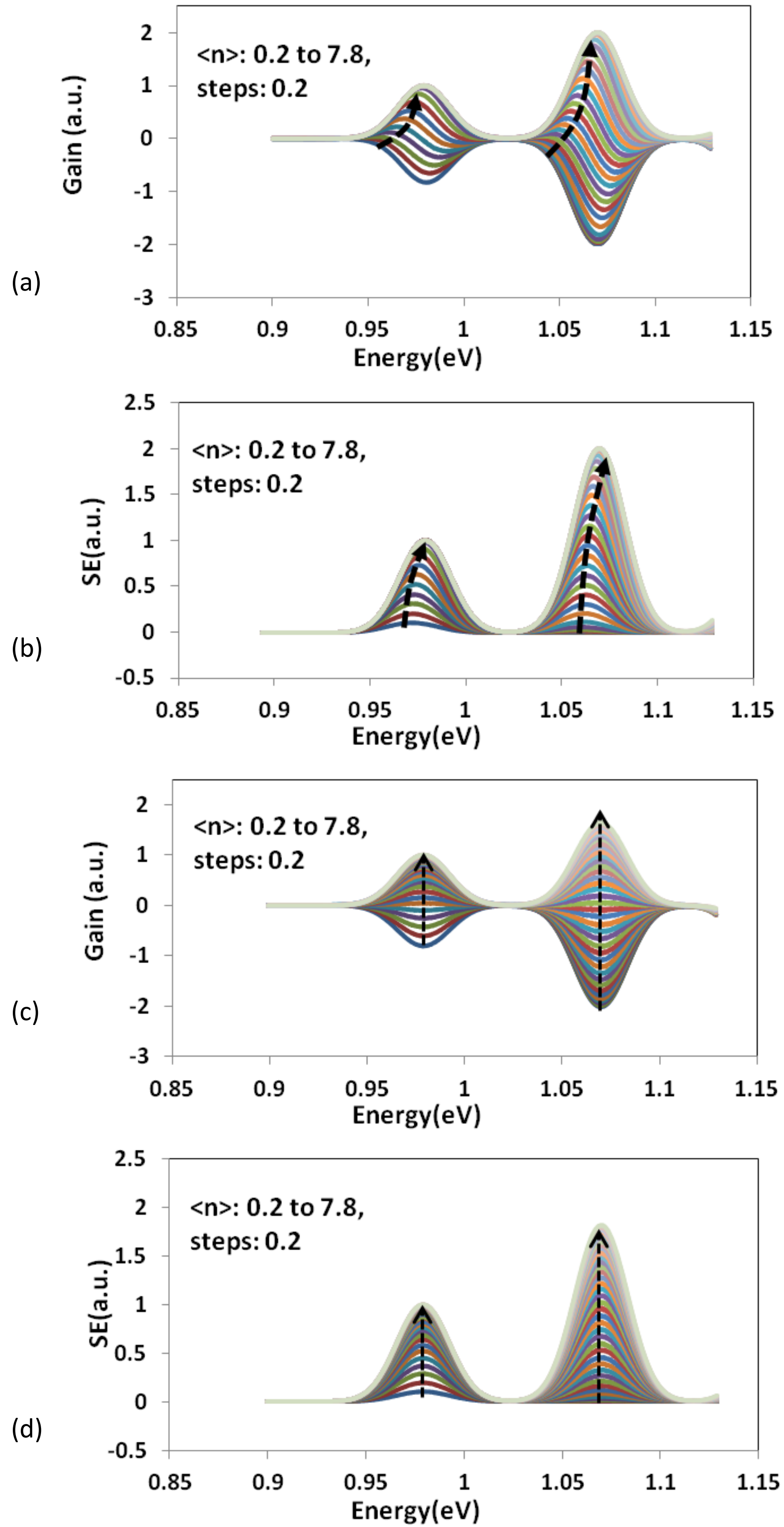

Figure 2.15: (a) Gain and (b) SE of Ensemble C for Fermi-Dirac carrier statistics. (c) gain and (d) SE of the same sample for random carrier distribution.

Figure 2.16 plots the gain divided by spontaneous emission rate (P_m) of Ensemble C for Fermi-Dirac and random carrier distributions. This value is proportional to the distribution function of electrons as discussed previously [12].

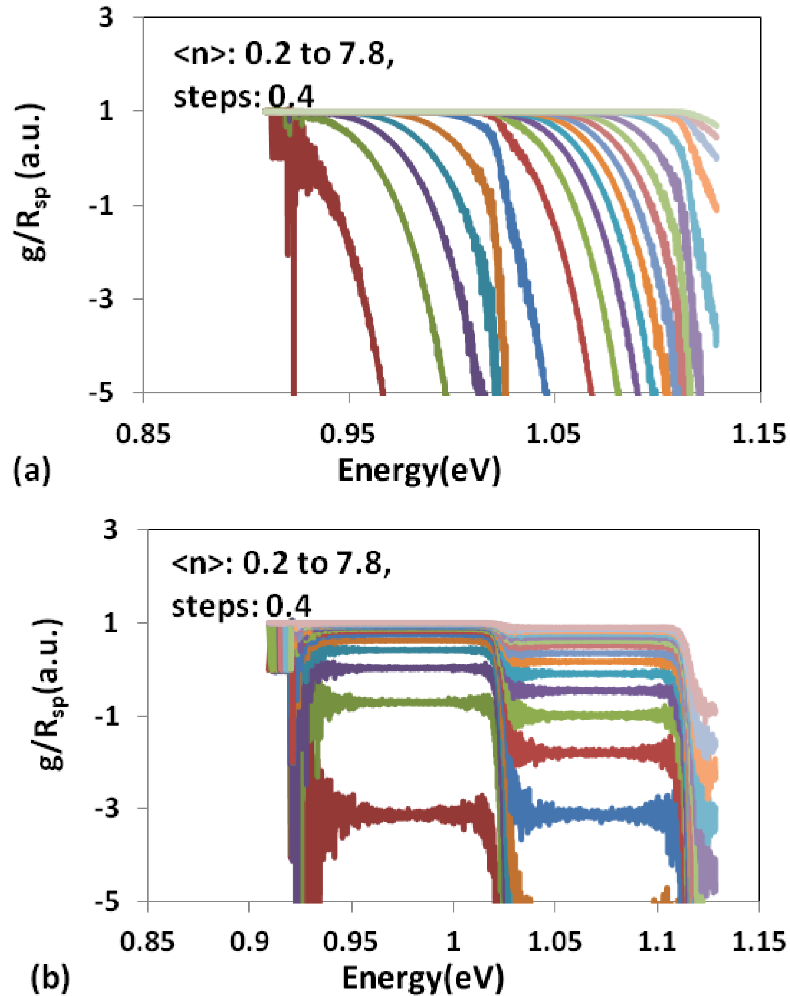

Figure 2.16: Gain divided by spontaneous emission of Ensemble C of quantum dots for (a) Fermi population and (b) random population of carriers at the same <n>. <n> is the average number of carriers per dot at 300K.

The influence of the density of states in the probability distribution of carriers makes a step like transition profile from GS to the ES1 for both Fermi-Dirac and random carrier statistics, which is a function of both state separation and inhomogeneous linewidth of the ensemble. It is also noted that in the case of random carrier statistics, the flat carrier distribution signature which was lost at higher energies for Ensemble B, is much better resolved in Ensemble C.

2.8.2.2 Simulation results including free carrier effects

Incorporating the same values for the homogeneous broadening and energy shift in the model, the gain and spontaneous emission spectra were recalculated and are plotted in figure 2.17(a, b) for Fermi-Dirac and (c, d) random carrier statistics at 300K for Ensemble C. Similar to Ensemble B (figure 2.14), the gain and spontaneous emission profiles look very similar for Fermi-Dirac and random statistics.

The modal gain divided by spontaneous emission (P_m) is plotted for (a) Fermi-Dirac and (b) random carrier statistics at 300K for Ensemble C in figure 2.18. The addition of these free-carrier effects is significant and strongly modulates these plots as compared to figure 2.16, where they are not included. It is noted that the two curves in figure 2.18(a) and 2.18(b) show very strong similarities.

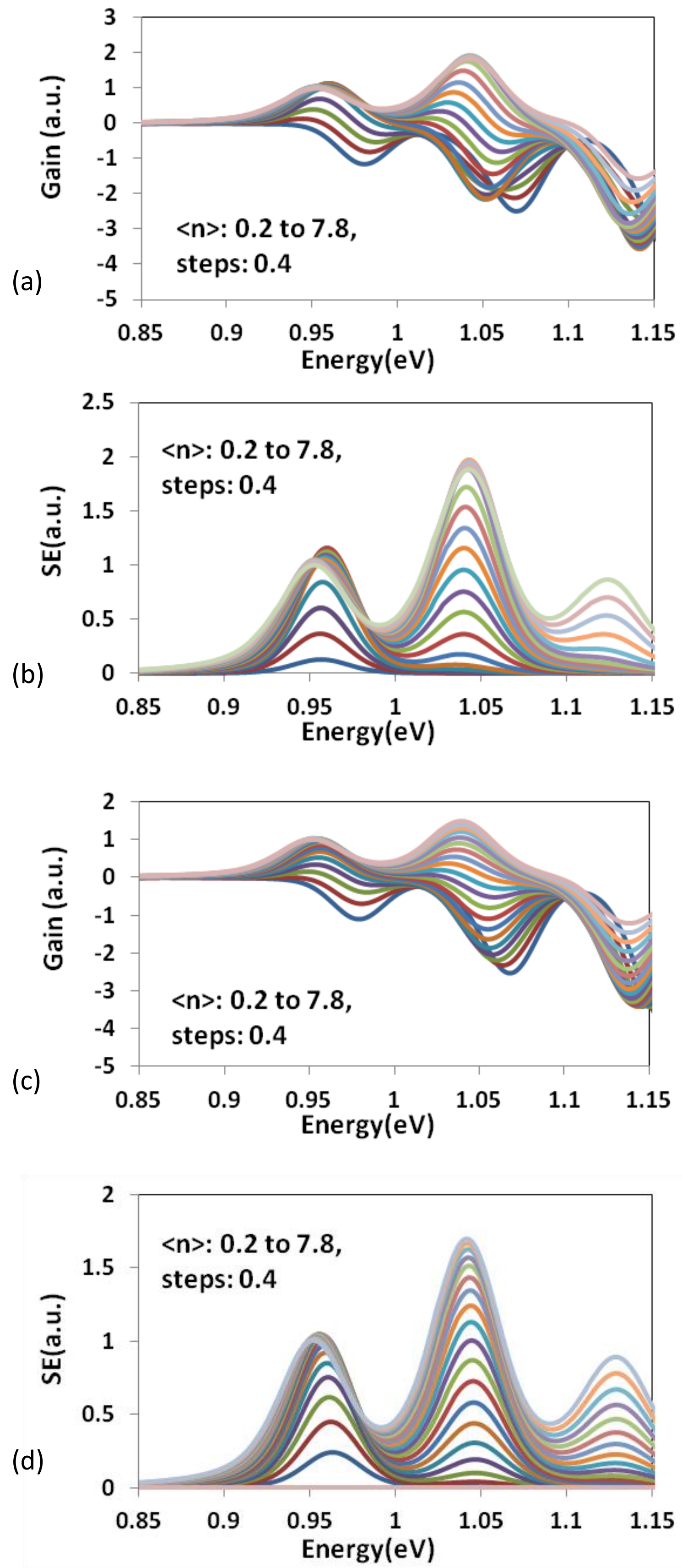

Figure 2.17 (a) Gain and (b) SE for Fermi-Dirac at 300K for Ensemble C. (c) Gain and (d) SE for random carrier statistics for the same sample.

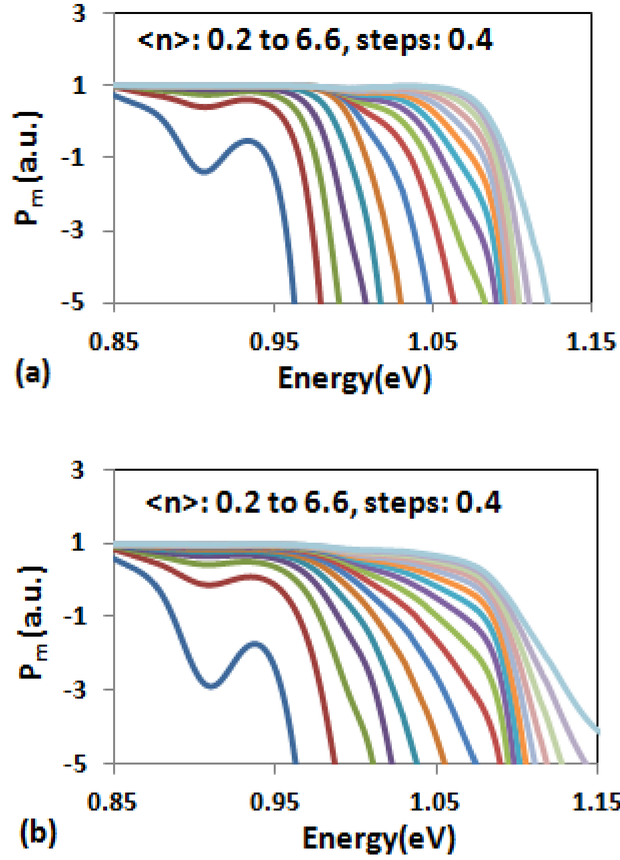

Figure 2.18: Gain divided by spontaneous emission as a function of energy for Ensemble C with (a) Fermi-Dirac and (b) random carrier statistics at 300K.

2.9 Experimental study - State-of-the-art QD laser material

In order to assess the suitability of this model, a QD laser with state separation and inhomogeneous linewidth identical to Ensemble C was studied experimentally. The wafer material was supplied by QD Laser Inc. (Japan).

The device under study in this chapter was a short cavity (250um) single-mode (3um ridge width) laser diode and was maintained at a constant junction temperature of 300K [16]. The gain and spontaneous emission spectra of the laser were measured by the Hakki-Paoli technique as discussed in chapter one.

The wafer structure of QLF1375-AA is plotted in figure 2.19 which includes eight layers of InAs quantum dots sandwiched by p/n doped AlGaAs cladding layers. The QDs have GS center wavelength of ~1285nm.

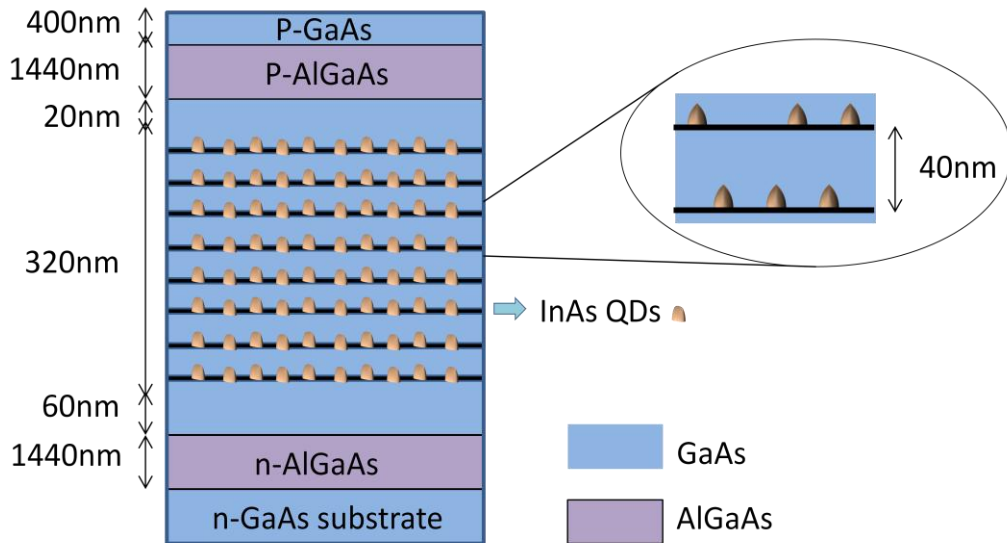

Figure 2.19: wafer structure of QLF1374-AA.

The epitaxy for this structure is essentially identical with the sample QLF1375-AE, which will be discussed in next chapter, except for the growth of the active region which starts with 60nm of undoped GaAs and then 8 layers of 40nm thick QD period. This period consists of ~2.5 monolayer InAs to form the QDs, an InGaAs SRL, and 32nm of GaAs [40].

A short cavity edge emitting laser was fabricated by Dr. K. Zhou with 3μm x 250μm dimensions through standard process steps. I used the Hakki Paoli gain measurement method as described previously in chapter one to characterise this device. The setup used is plotted schematically in figure 2.20.

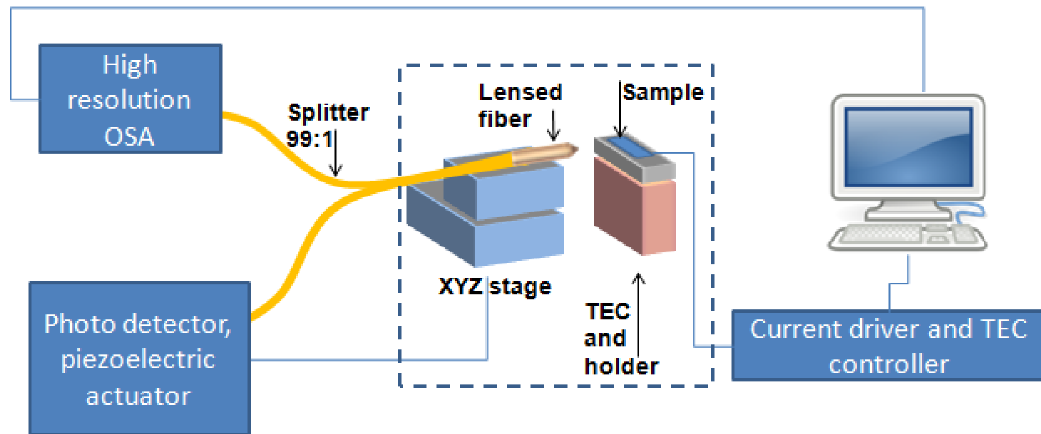

Figure 2.20: Schematic of the setup used for gain measurements.

The sample was placed on a platinum plated copper sample holder. Continuous wave current was applied to the laser by a current source, ILXLightwave- LDP 3811. The temperature of the sample was kept constant with a thermoelectric cooler (TEC). The TEC was sandwiched between two parts of the copper block (sample holder and heatsink) in order to maintain a stable upper temperature using a PID controller. To measure the gain, amplified spontaneous emission of the laser was collected by a lensed single mode fiber coupled to a high resolution spectrum analyser (Advantest Q8384). 1% of the collected light was split and used by a feedback loop to control piezoelectric actuators holding the fibre in order to maintain the maximum fibre coupling over extended times. In order to resolve individual Fabry-Perot modes the resolution of the OSA was set to 0.02nm with 10000 data points. Under the CW current the device was characterized at a constant junction temperature by compensating for the temperature dependent individual mode shifts [16].

ASE from the chip is plotted in figure 2.21. The inset shows the individual Fabry-Perot modes for different current densities. To keep the junction

temperature constant the peaks of the modes are kept fixed in wavelength by changing the sample holder temperature as applied current is increased.

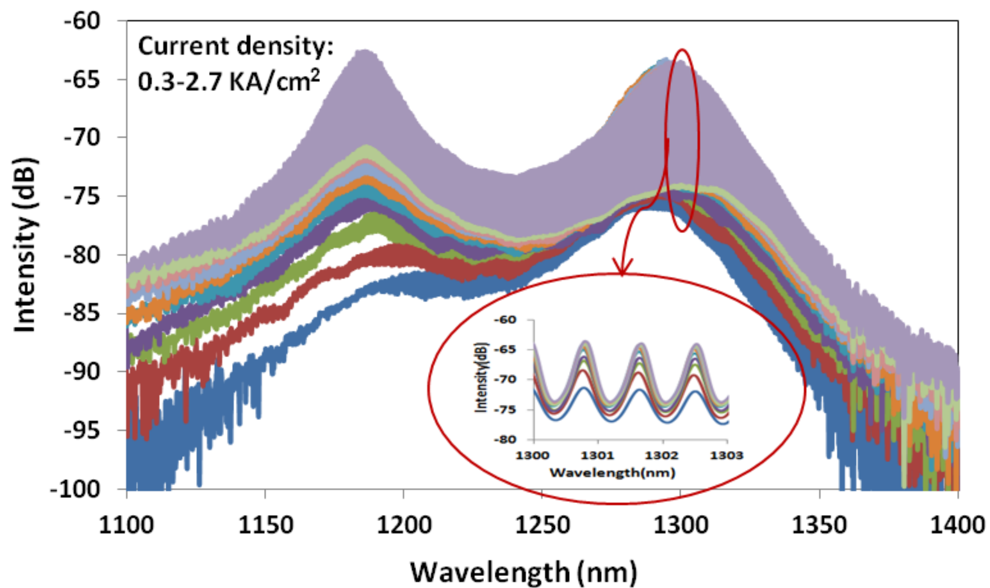

Figure 2.21: EL intensity of QLF1374-AA laser at constant junction temperature. The inset shows the Fabry-Perot modes at different current densities.

The GS of the QDs can be seen at ~1300nm. Further increase in current density leads to an increase in intensity and the appearance of a peak at ~1180nm which is attributed to the ES1 of the QDs.

Figure 2.22 plots the calculated gain of this device as discussed in chapter one. Figure 2.23 provides the spontaneous emission spectra calculated from the gain data and original amplified spontaneous emission spectra. The state separation and inhomogeneous linewidths in this sample were used in defining the state separation and linewidth in Ensemble C.

The modal gain divided by spontaneous emission (P_m) is plotted for this sample in figure 2.24.

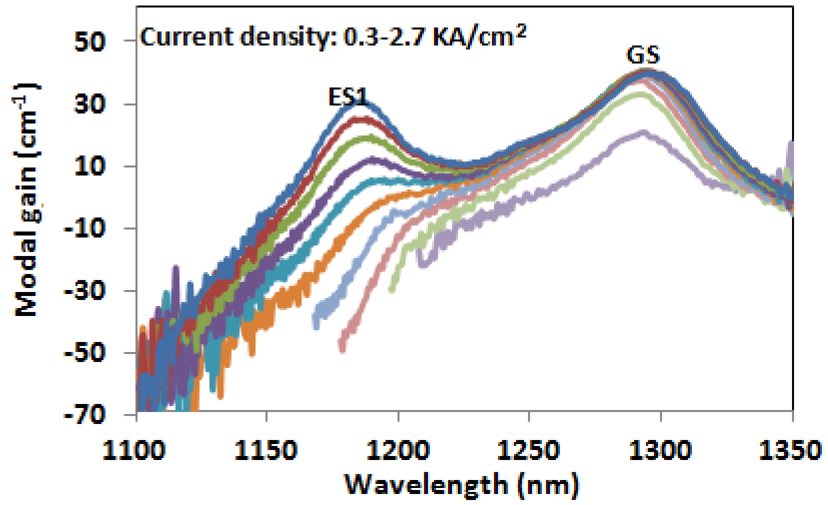

Figure 2.22: Modal gain of QLF1374-AA laser at constant junction temperature.

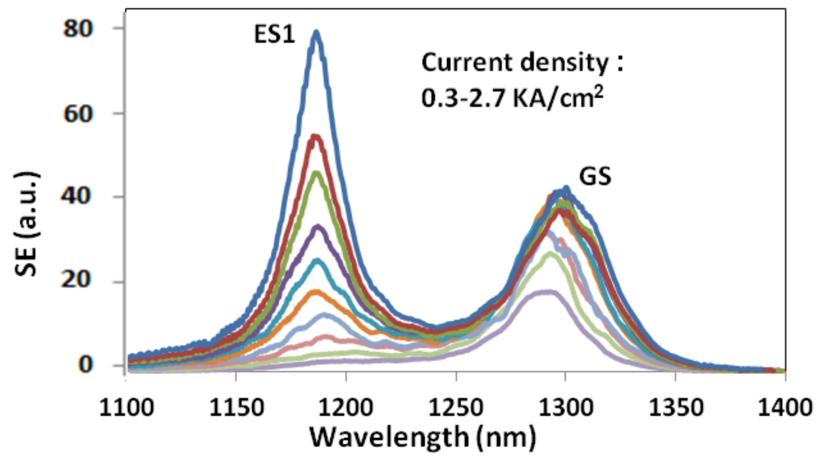

Figure 2.23: Spontaneous emission of QLF1374-AA laser at constant junction temperature.

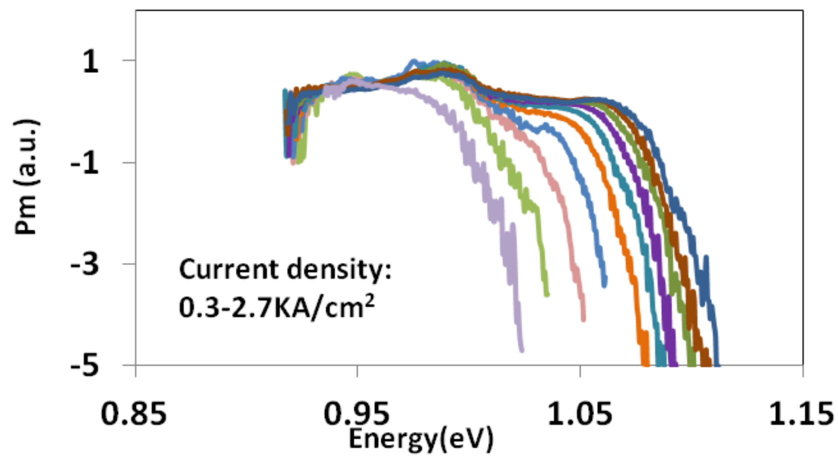

Figure 2.24: Normalized gain divided by spontaneous emission as a function of energy for QD laser.

2.10 Ln(1-Pm) plots

The gradient of a plot of Ln[1-P_m] against emission energy for the excited states of the QD ensemble has been used to infer details of the carrier population [13]. In figure 2.25 I recast the data presented in Figures 2.13(a) and 2.16(a) in order to plot this value for these two different QD ensembles in the case of Fermi-Dirac carrier statistics.

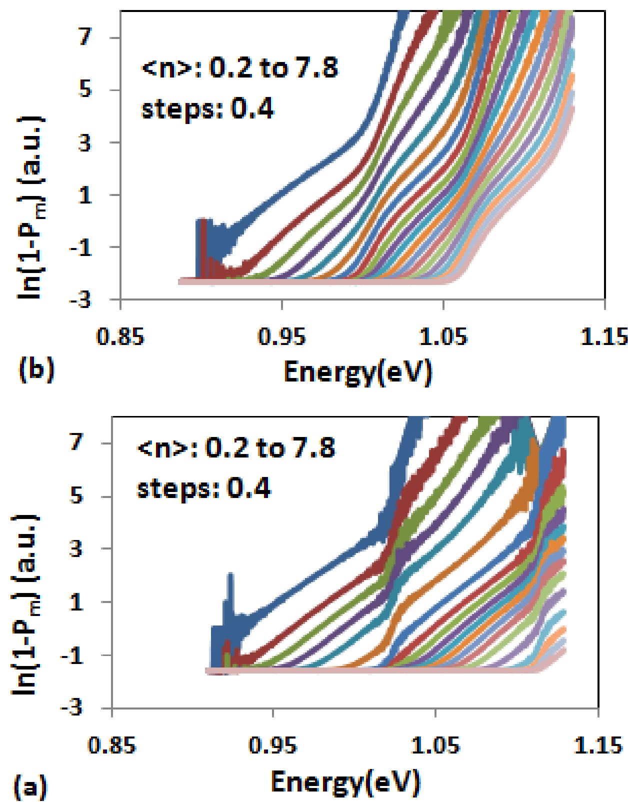

Figure 2.25: Logarithmic plots of [1-Pm] versus photon energy for Fermi-Dirac carrier statistics of (a) Ensemble B and (b) Ensemble C at 300K.

Steps are observed in the plots which is due to the energy separation term in equation 2.5. We note that the gradient is not constant over all regions of these plots. For the gradient of this plot to be considered as a measure of carrier temperature only the values in the region of the GS emission should be considered as the overlap of higher order states “modulates” the curve and the gradient is no longer constant. Fermi-Dirac carrier statistics were chosen in this

case to highlight the influence by quantum dot state separation and inhomogeneous broadening.

2.11 Discussion

With regard to the simulation very different gain and SE spectra and carrier distribution functions are observed when free carrier effects are not included (figure 2.13). Strong similarities are observed between the two simulations using very different carrier statistics when free carrier effects are included. The positive gradient region to the lower energy side of the ground-state of the quantum dots (at ~0.92eV in figure 2.18(a) and 2.18(b)) is a particular signature of the effects of the free carriers in the simulation regardless of carrier statistics.

Such a positive gradient has been observed previously for 1000nm QDs (low confinement energy) at low temperature and attributed to a non-equilibrium carrier distribution [12]. This positive gradient feature is clearly observed experimentally for these deeply confined QDs at room temperature in figure 2.24. It is noted that the experimentally measured P_m does not resemble either of the plots in figure 2.18 where free carrier effects are ignored. This suggests that free carrier effects must be considered in order to accurately predict the gain and SE spectra.

Differences between the simulated (including free carrier effects) 2.18(a) and 2.18(b) and experimental results 2.24 are observed around 1.02eV. This is attributed to the simulation not including any nominally forbidden transitions due to parity conservation. This is not surprising, since a real QD has strain,

width and composition variation leading to a potential that is far from that of an infinitely deep QD.

From these simulations and experimental data, I conclude that the deduction of the carrier statistics from this measurement is very difficult. Moreover, I conclude that the dominant effects which determine the form of the spontaneous emission and gain spectra, even at low levels of carrier injection are the free carrier effects.

2.12 Summary and future work

In this chapter I have described simulation results of the effect of free-carrier induced shift and broadening on the carrier distribution function. Different carrier statistics (Fermi-Dirac and random carrier distribution) have been studied. It has been shown that the free carrier effects are important at high QD occupancies, as well as lower carrier densities where QD lasers would normally operate. It is concluded that the free carrier effects dominate the form of the gain and spontaneous emission spectrum for the QD ensemble, rather than the carrier statistics

It has been shown that the gain and SE profiles do not show unambiguous signatures of carrier distribution. In order to find a solution to identify the carrier distribution we may study the GS and ES1 peak values and crossing points. To clarify this, the peak values of the GS and ES1 in gain and SE are plotted in figure 2.26 (a) and (b) for Fermi-Dirac statistics for ensemble A at room temperature including free carrier effects. The same graphs are plotted for random statistics in 2.26 (c) and (d). From the simulation results a clear

difference is observed in the crossing points of GS and ES1 peak values for Fermi-Dirac and random carrier distributions.

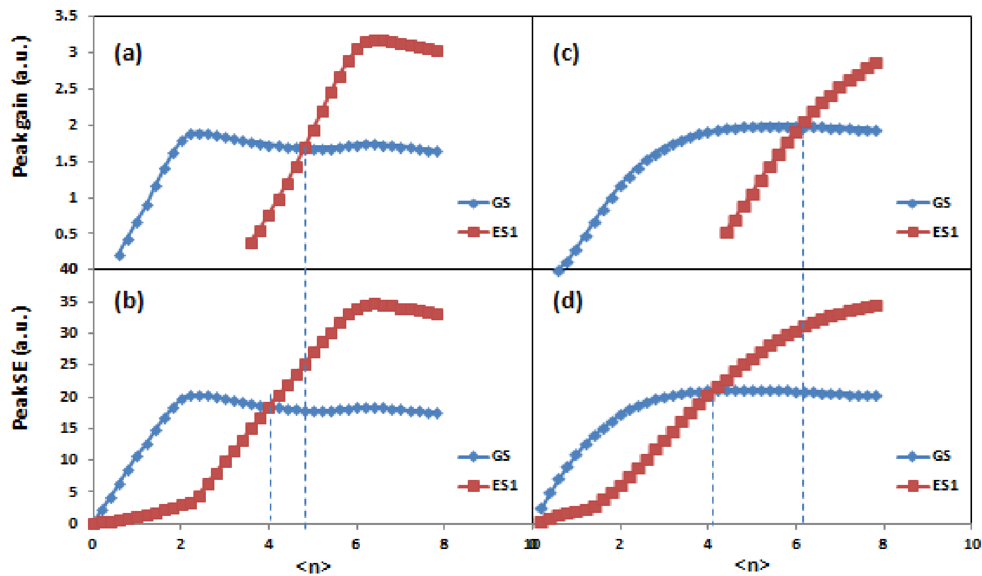

Figure 2.26: (a) Gain and (b) SE peak values for Fermi-Dirac statistics of ensemble A. (c) Gain and (d) SE peak values for random statistics of the same sample.

For random population a large difference in n is noted for equal GS and ES SE (~<4>) and gain (~<6>) as compared to the case for Fermi-Dirac statistics where equal SE (~<4>) and gain (~<4.7>).

Same values for the QD laser, extracted from figures 2.22 and 2.23, are plotted in figure 2.27. The peak values in SE GS and ES over cross each other at current density ~2050A/cm^2. However, the current density of 2700A/cm^2 is not enough for gain of the ES to overcome the gain of GS in QDs.

The data in figures 2.26 and 2.27 are not easily comparable since the simulation results show the peak values vs. the average number of carriers per QD while the experimental data shows the values vs. carrier density. Converting these two parameters requires accurate knowledge of the carrier lifetime based on the following equation:

$$\tau_c = \frac{< n > qN_{qd}}{J.\eta_i} \tag{2.6}$$

Where J is the current density, N_{qd} is the areal dot density, q is the electron charge, and η_i is the internal quantum efficiency which is introduced to account for the efficiency of converting carriers into photons and is assumed to be independent of current [41].

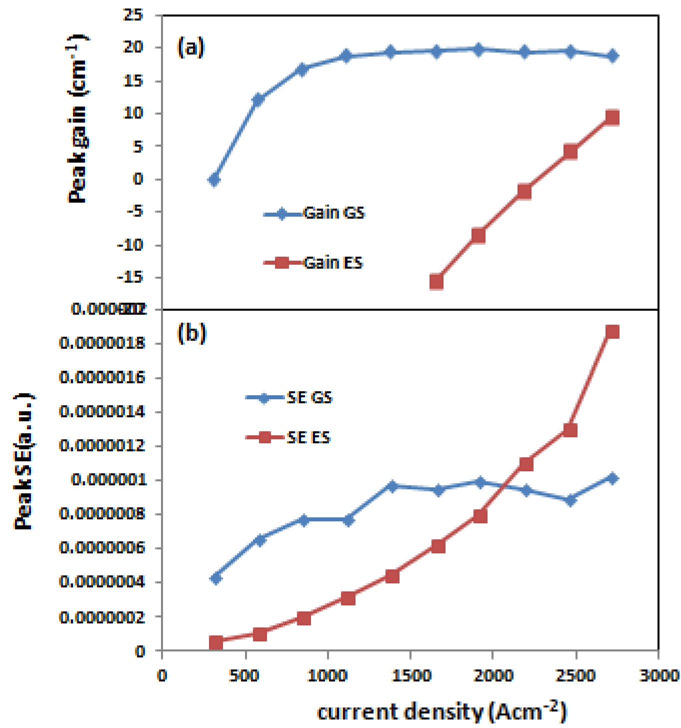

Figure 2.27: (a) Gain and (b) SE peak values for QD laser.

If we could have a method which gives the carrier lifetime simultaneously with the gain and SE spectrum, then we may be able to determine the carrier population in QDs. Differential carrier lifetime and temperature dependent studies have been carried out to this end [42], but a combined measurement has yet to be carried out.

References

[1] L. A. Coldren, S. W. Corzine, "Diode lasers and photonic integrated circuits," Wiley (1995).

[2] C. M. Sottomayor Torres, "energy relaxation in quantum dots: recent developments on the phonon bottleneck," Hot carriers in semiconductors: 287-292 (1996).

[3] M. Grundmann and D. Bimberg, "Theory of random population for quantum dots," Phys. Rev., 55, 15 (1996).

[4] M. Sugawara, K. Mukai, Y. Nakata, H. Ishikawa and A. Sakamoto, "Effect of homogeneous broadening of optical gain on lasing spectra in self assembled $In_xGa_{1-x}As/GaAs$ quantum dot lasers," Phys. Rev. B, 61, 7595 (2000).

[5] K. Matsuda, K. Ikeda, and T. Saiki, H. Saito and K. Nishi, "Carrier–carrier interaction in single $In_{0.5}Ga_{0.5}As$ quantum dots at room temperature investigated by near-field scanning optical microscope," Appl. Phys. Letts., 83, 11 (2003).

[6] A. V. Uskov, I. Magnusdottir, B. Tromborg, J. Mørk and R. Lang, "Line broadening caused by Coulomb carrier–carrier correlations and dynamics of carrier capture and emission in quantum dots," Appl. Phys. Letts., 79, 1679 (2001).

[7] Y. Arakawa and H. Sakaki, "Multidimentional quantum well laser and temperature deppendance on its threshold current," Appl. Phys. Lett., 40, 939 (1982).

[8] M. Asada, Y. Miyamoto and Y. Suematsu, "Gain and the threshold of three-dimensional quantum-box lasers," IEEE J. Q. Elect., QE-22, 1915 (1986).

[9] P. M. Smowton, E. J. Pearce, J. Lutti, D. R. Matthews, H. D. Summers, G. M. Lewis, P. Blood, M. Hopkinson and A. Krysa, "Carrier distribution, spontaneous emission and gain in self assembled quantum dot lasers," Invited Paper, Proc. of SPIE, 5365 (2004).

[10] G. A. Alexander, "Carrier distributions in long wavelength quantum dot laser diodes," PhD Thesis, School of Physics and Astronomy Cardiff University (2007).

[11] M. Grundmann, R. Heitz, D. Bimberg, "New approach to modelling carrier distribution in quantum dot ensembles: Gain and threshold of QD lasers and impact of

phonon bottleneck," Physica E: Low-dimensional Systems and Nanostructures, 2, 1–4, 725 (1998).

[12] H. D. Summers, J. D. Thomson, P. M. Smowton, P. Blood and M. Hopkinson, "Thermodynamic balance in quantum dot lasers," Semicond. Sci. Technol., 16, 140 (2001).

[13] M. Hutchings, I. O'Driscoll, P. M. Smowton and P. Blood, "Fermi-Dirac and random carrier distributions in quantum dot lasers," Appl. Phys. Lett., 104, 031103 (2014).

[14] A. Markus, M. Rossetti, V. Calligari, J. X. Chen, and A. Fiore, "Role of thermal hopping and homogeneous broadening on the spectral characteristics of quantum dot lasers," J. Appl. Phys., 98, 104506 (2005).

[15] I. O'Driscoll, P. Blood and P. M. Smowton, "Random population of quantum dots in InAs–GaAs laser structures," IEEE J. Q. Elec., 46, 525 (2010).

[16] H. Shahid, D. T. D. Childs, B. J. Stevens, and R. A. Hogg, "Negative differential gain due to many body effects in self-assembled quantum dot lasers," Appl. Phys. Lett. 99, 061104 (2011).

[17] H. C. Schneider, W. W. Chow and S. W. Koch, "Many-body effects in the gain spectra of highly excited quantum-dot lasers," Phys. Rev. B, 64, 115315 (2001).

[18] M. Lorke, T. R. Nielsen, J. Seebeck, P. Gartner, and F. Jahnke, "Influence of carrier-carrier and carrier-phonon correlations on optical absorption and gain in quantum-dot systems," Phys. Rev.B 73, 085324 (2006).

[19] M. Bayer and A. Forchel, "Temperature dependence of the exciton homogeneous linewidth in $In_{0.60}Ga_{0.40}As$/GaAs self-assembled quantum dots," Phys. Rev. B 65, 041308(R) (2002).

[20] P. Borri, W. Langbein, S. Schneider, U. Woggon, R. L. Sellin, D. Ouyang, and D. Bimberg, "Ultralong Dephasing Time in InGaAs Quantum Dots," Phys. Rev. Lett. 87, 157401 (2001).

[21] M. Lorke, W. W. Chow, T. R. Nielsen, J. Seebeck, P. Gartner, and F. Jahnke, “Anomaly in the excitation dependence of the optical gain of semiconductor quantum dots,” Phys. Rev. B 74, 035334 (2006).

[22] E. Goldmann, S. Barthel, M. Florian, K. Schuh, and F. Jahnke, “Excitonic fine-structure splitting in telecomwavelength InAs/GaAs quantum dots: Statistical distribution and height-dependence,” Appl. Phys. Lett. 103, 242102 (2013).

[23] M. Grundmann and D. Bimberg, “Theory of random population for quantum dots,” Phys. Rev. B 55, 15, 9740 (1997).

[24] E. Goldmann, M. Lorke, T. Frauenheim, and F. Jahnke, “Negative differential gain in quantum dot systems: Interplay of structural properties and many-body effects,”Appl. Phys. Lett. 104, 242108 (2014).

[25] H.C.Wong, M. Dragas, G. B. Ren, J. M. Rorison, M. Hopkinson, “Temperature Dependence of Carrier Dynamics in an Inhomogeneous Array of Quantum Dots,” Proceedings of SPIE Vol. 5452, (2004).

[26] H.C. Wong, G.B. Ren and J.M. Rorison, “Mode amplification in inhomogeneous QD semiconductor optical amplifiers,” Optical and Quantum Electronics 38:395–409 (2006).

[27] H.C. Wong, G.B. Ren and J.M. Rorison, “The Constraints on Quantum-Dot Semiconductor Optical Amplifiers for Multichannel Amplification,” IEEE Photonics technology letters, vol. 18, no. 20, (2006).

[28] M. Gioannini, A. Sevega and I. Montrosset, “Simulations of differential gain and linewidth enhancement factor of quantum dot semiconductor lasers,” Optical and Quantum Electronics 38:381–394 (2006).

[29] X. Sun, N. Vogiatzis, and J. M. Rorison, “Theoretical Study on Dilute Nitride 1.3μm Quantum Well Semiconductor Optical Amplifiers: Incorporation of N Compositional Fluctuations,” IEEE Journal of quantum electronics, vol. 49, no. 10, (2013).

[30] X. Sun, N. Vogiatzis, and J. M. Rorison, “Modeling Dilute Nitride 1.3 μm Quantum Well Lasers: Incorporation of N Compositional Fluctuations,” EEE Journal of selected topics in quantum electronics, vol. 19, no. 5, (2013).

[31] S. V. Nair and Y. Masumoto, “Multi-Exciton states in semiconductor quantum dots,” Phys. Stat. Sol. 178, 303 (2000).

[32] P. D. Siverns, S. Malik, G. McPherson, D. Childs, C. Roberts, R. Murray, B. A. Joyce, and H. Davock, “Scanning transmission-electron microscopy study of InAs/GaAs quantum dots,” Phys. Rev. B. 58, 16 (1998).

[33] D. A. Kleinman and R. C. Miller, “Band-gap renormalization in semiconductor quantum wells containing carriers,” Phys. Rev. B 32, 2266 (1985).

[34] A. Dikshit, V. Vangapally, and J. Pikal, “Carrier lifetime in 1.3 μm InAs quantum-dot lasers using small-signal modulation technique,” Proc. SPIE 6017, 60170L (2005).

[35] H. Kissel, U. Muller, C. Walther, and W. T. Masselink, “Size distribution in self-assembled InAs quantum dots on GaAs (001) for intermediate InAs coverage,” Phys. Rev. B 62, 7213 (2000).

[36] P. D. L. Greenwood, D. T. D. Childs, K. Kennedy, K. M. Groom, M. Hugues, M. Hopkinson, R. A. Hogg, N. Krstaji´ c, L. E. Smith, S. J. Matcher, M. Bonesi, Sh. MacNeil and R. Smallwood, “Quantum dot superluminescent diodes for optical coherence tomography: device engineering,” IEEE J. Sel. Top. in Q. Elect. 16, 1015 (2010).

[37] R . Heitz, F. Guffarth, I. Mukhametzhanov, M. Grundmann, A. Madhukar and D. Bimberg, “Many-body effects on the optical spectra of InAs/GaAs quantum dots,” Phys. Rev. B, 62, 16881 (2000).

[38] J. Camassel, D. Auvergne, and H. Mathieu, “Temperature dependence of the band gap and comparison with the threshold frequency of pure GaAs lasers,” J. Appl. Phys., 46, 2683 (1975).

[39] S. Tarucha, H. Kobayashi, Y. Horikoshi, and H. Okamoto, “Carrier induced energy-gap shrinkage in current injection GaAs/AlGaAs MQW heterostructures,” Jap. J. Appl. Phys., 23, 874 (1984).

[40] K. Nishi, T. Kageyama, M. Yamaguchi, Y. Maeda, K. Takemasa, T. Yamamoto, M. Sugawara, Y. Arakawa, “Molecular beam epitaxial growths of high-optical-gain InAs quantum dots on GaAs for long-wavelength emission,” J. Crystal Growth 378, 459 (2013).

[41] R. R. Alexander, "GaAs based quantum dot lasers for 1.3m optical communications," PhD thesis, Department of Electronics and Electrical Engineering, University of Sheffield (2010).

[42] K. Zhou,"Analysis of 1.3μm GaAs quantum dot structure based devices," PhD thesis, Department of Electronic and Electrical Engineering, University of Sheffield, (2014).

Chapter 3: Study of QW Optical Pumping Effects on QDs in Hybrid QW/QD Samples

3.1 Introduction

Hybrid QW/QD structures show promise for broad spectral bandwidth [1]. It has been shown that incorporating QW layers in hybrid QW/QD structures changes the behaviour of the QDs. This is evidenced by a change in the lasing sequence for lasers of particular cavity length which exhibit multi-state lasing [2]. In this chapter optical pumping of the QD active element by emission from the QW active element, which is spectrally overlapped with second excited state (ES2) of the QDs, is explored. Consequently, hybrid QW/QD samples with different structures are investigated. A QD laser, a hybrid QW/QD SLD and three mesa diodes with different active area structures are fabricated and the characteristics of these devices are discussed. It is shown that how the emission from quantum well layer modifies the QD emission in terms of the emission spectrum (peak position and FWHM) and an increase in the intensity of the GS following apparent saturation.

3.2 Previous work and motivation

Previously, samples based on hybrid quantum dot and quantum well layers have been studied with the aim of obtaining a broad spectral bandwidth, as well as high modal gain [1]. In order to verify the effects of introducing a single QW layer to a QD multi-layer stack, three lasers with different active region structure were investigated. This includes:

- a “control” structure with 7 layers of QDs in active region,
- “n-side” structure presenting the active area with the QW layer next to the n contact of the device followed by 6 layers of QDs ,
- “p-side” structure with the QW layer next to the p contact followed by 6 layers of QDs.

The carrier transport/distribution in these structures has been discussed extensively and modal gain covering the wavelength range of 1100 to 1400nm was measured from the segmented contact device based on the n-side structure [3].

The gain spectra and amplified spontaneous emission of devices based on these materials was also analysed [2]. In figure 3.1 peak modal gain as a function of current density for the QD ground state (GS), the QD first excited state (ES1), and the lowest energy transition of QW in hybrid QW/QD sample is plotted. The modal gain of the QD GS is observed to saturate around 12±1 cm^{-1}, due to the limited density of states in QDs in line with the previous work [4]. Increasing the current density leads to an increase of modal gain of the QD ES1 transitions which is expected to be twice as that of QD GS saturated modal gain [5]. However, it appears that the ES1 does not fully saturate and appears to be pinned at an average QD occupancy around 6 e-h pairs per QD [3]. After clamping of ES1 at intermediate current densities a further increase of current leads to an increase of the modal gain of the QW. In figure 3.1 the threshold gain for lasers of different cavity lengths is marked. The internal loss for these devices was 10±0.5cm^{-1}.

Figure 3.2 plots the emission spectra as a function of current density for a laser with 2mm cavity length with as-cleaved facets. Calculating the mirror loss, and adding the experimentally determined internal loss the laser is expected to have a threshold gain of ~15cm^{-1} as shown in figure 3.1. At this length the gain of the GS transition (at 1310nm)

should be too small to overcome the total losses resulting in lasing initially from ES1 transitions (at ~1225nm). Additional lasing emission attributed to the QW (~1150nm) appears by increasing the current density, which is due to poor gain clamping in the QDs, followed by a third lasing peak attributed to QD GS (~1310nm) for further increase in current. Inspection of figure 3.1 indicates that when measured using the segmented contact method, the GS gain should be insufficient to support lasing for a cavity with these losses.

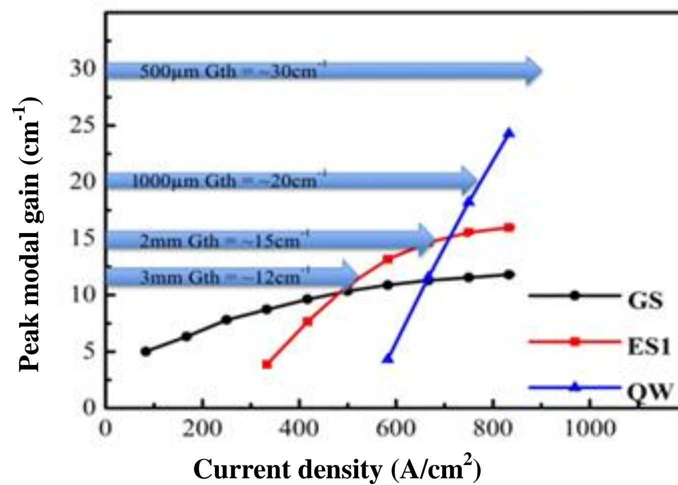

Figure 3.1: Peak modal gain as a function of current density for QD GS and ES1, and the lowest energy transition of QW in hybrid QW/QD sample [2].

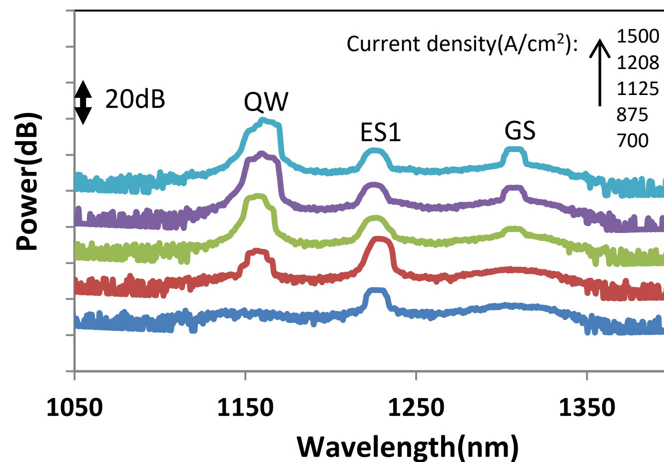

Figure 3.2: The emission spectra as a function of current density at room temperature for a 2mm long cavity [2].

The lasing spectrum at various current densities for another sample with 1mm cavity length was investigated and the results are presented in figure 3.3. At this cavity length the gain of ES1 is not sufficient to overcome the total loss and the lasing starts with the

QW transition. Increasing current density leads to additional lasing attributed to the ES1 of the QDs. Again, referring to figure 3.1, lasing from QD GS and ES1 is unexpected due to insufficient modal gain.

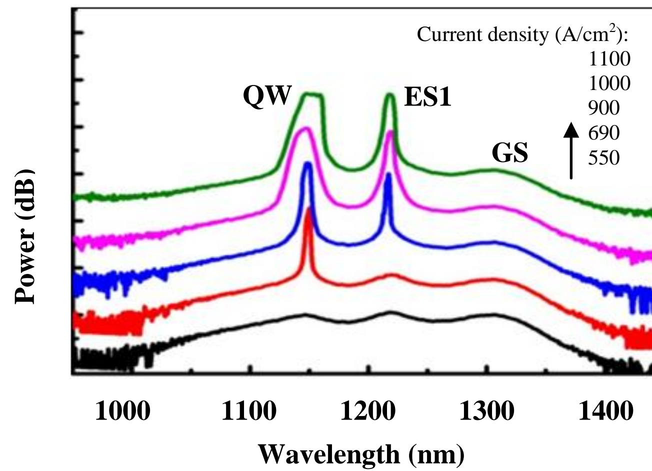

Figure 3.3: lasing spectra at various current densities for 1mm cavity length laser [2].

It appears that at higher current densities some process is enhancing the gain in the QDs. The QD density is obviously fixed, and there is no evidence for a change in radiative rate. A possible explanation for this behaviour is an enhancement of carrier capture into the QDs. Applying a current density in the range of 1 kA/cm^2 results in the gain of the ES1 being greater than the GS. Since it is not fully saturated (around 6 e-h pair per QD), it is not large enough to affect the normal behaviour of QDs. *i.e.* their physics has not previously been shown to change in this region. An alternative explanation which should be explored is that there might be an optical pumping process occurring between the QW layers and QDs leading to the increase in the modal gain in the QD GS region. In other words it is proposed that the QDs absorb photons generated by the QW within the cavity leading to an apparent decrease in carrier capture time. Therefore, the GS gain increases effectively and starts lasing.

In the remainder of this chapter I explore a number of experiments to cast further light on such processes.

3.3 Methodology

3.3.1 QD laser

In order to explore the possibility of QW layer optical pumping, the gain and spontaneous emission of a single mode QD laser with a structure based on 8 layers of QDs (QLF1374-AA material) was measured via the Hakki Paoli method [6] as discussed in chapter one. In comparison with the previous material grown at the University of Sheffield this commercial wafer has higher QD areal density. The details of the wafer structure and the measurement setup are explained before in chapter 2 (section 2.9).

Figure 3.4 plots the gain and spontaneous emission at 2.7kA/cm^2 for this laser. This operating current gives the excited state spontaneous emission greater than that of the ground state. These values of occupancy are similar to those of the QDs described in figure 3.1. It is clear that for this current density, at the wavelength range of the second excited state (~1100nm) the gain spectrum is in loss. Therefore waveguided emission from the QW at ~1100nm is likely to be absorbed by the QDs.

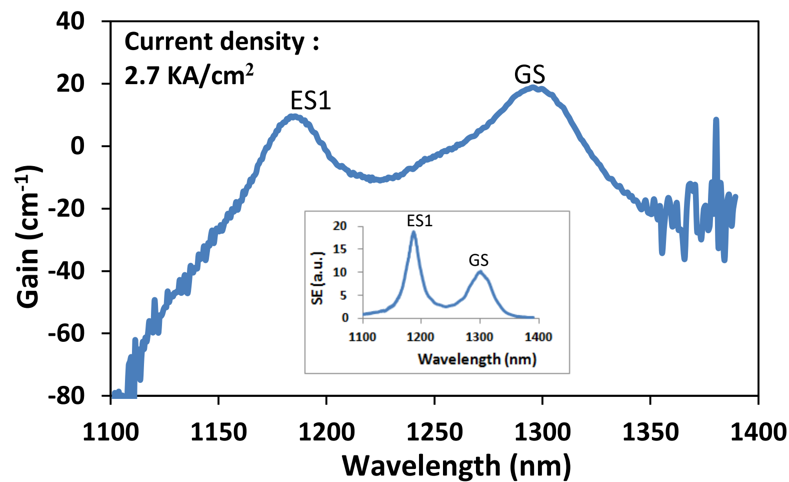

Figure 3.4: Gain of QLF1374-AA laser at 2.7kA/cm^2 at 19°C. The inset shows the spontaneous emission of the same device.

3.3.2 Superluminescent diode

In order to investigate the effect of QW emission on QD gain and SE, a multi-section superluminescent diode (SLD) was fabricated based on a hybrid QW/QD structure, QLF1375-AE.

The details of the wafer structure are schematically shown in figure 3.5.

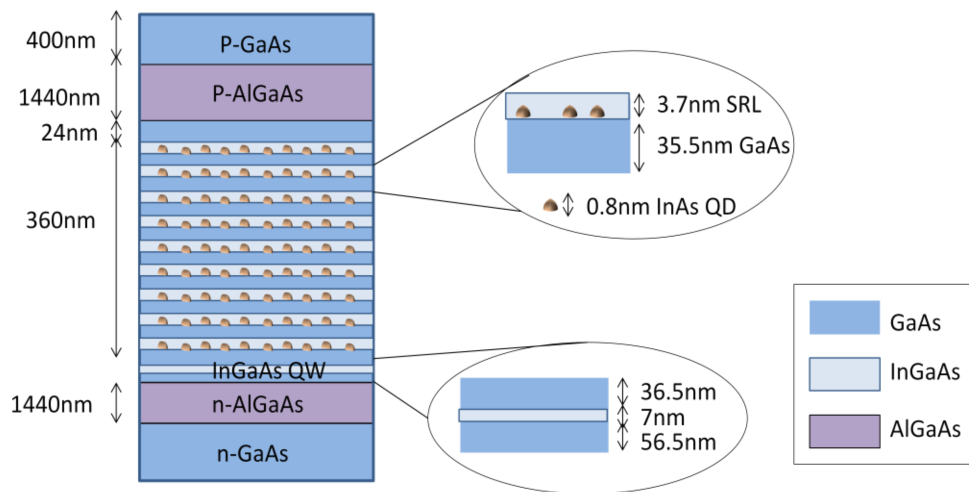

Figure 3.5: Schematic of QLF1375-AE wafer structure.

The epitaxial steps for this wafer structure includes a 300nm n-type GaAs buffer layer on top of a 3-inch n-type GaAs substrate, followed by 20nm n-type $Al_{0.2}Ga_{0.8}As$, 1400nm $Al_{0.4}Ga_{0.8}As$, and 20 nm $Al_{0.2}Ga_{0.8}As$ as the lower cladding layer. This combination is used to smooth the band discontinuities. Above this layer the active region is grown followed by upper cladding layer including 20nm p-type $Al_{0.2}Ga_{0.8}As$, 1400nm $Al_{0.4}Ga_{0.8}As$ and 20nm $Al_{0.2}Ga_{0.8}As$. At the end of the epitaxy process 400nm of highly p-doped GaAs contact layer was grown.

The active region growth starts with 56.5nm of undoped GaAs following by 7nm of InGaAs QW (1080nm), and another 36.5nm of GaAs. Above this QW layer 9 layers of InAs QDs (1280) are grown. Each layer contains 0.8nm InAs, capped with a 3.7nm InGaAs strain reducing layer (SRL) to relax the strain on the InAs QDs due to the

lattice mismatch between InAs and GaAs. With a larger lattice constant, capping with an SRL layer results in a smaller bandgap red shift induced by strain [7]. 35.5nm undoped GaAs barrier layer is inserted between the layers of QDs.

The SLD was designed to have a tilted waveguide in order to inhibit reflection of the light back into the device. The back end of the contacts/ridge of the device was designed to be wider to assist in the prevention of lasing as absorption of backward-propagating light is maximized. This sample included ten sections of 3μm wide waveguides each of 525μm length. Fabricated steps are described in chapter 1 (section 1.4.2). The sample was then mounted on a copper block instead of ceramic tile to extract the heat as much as possible. Schematic and microscopic images of the SLD are shown in figure 3.6.

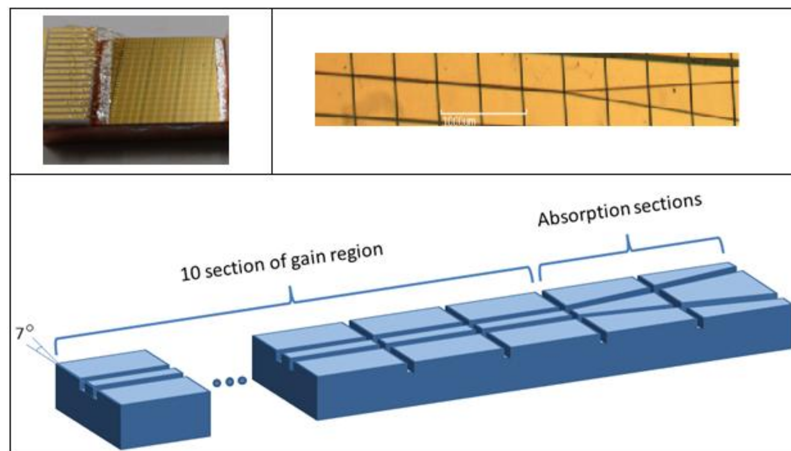

Figure 3.6: Schematic and microscopic images of the SLD.

Segmented contact gain measurements were performed with the same setup as used in the Hakki-Paoli method in chapter 2.

Spontaneous emission of the device is calculated as discussed in chapter one and is plotted in figure 3.7.

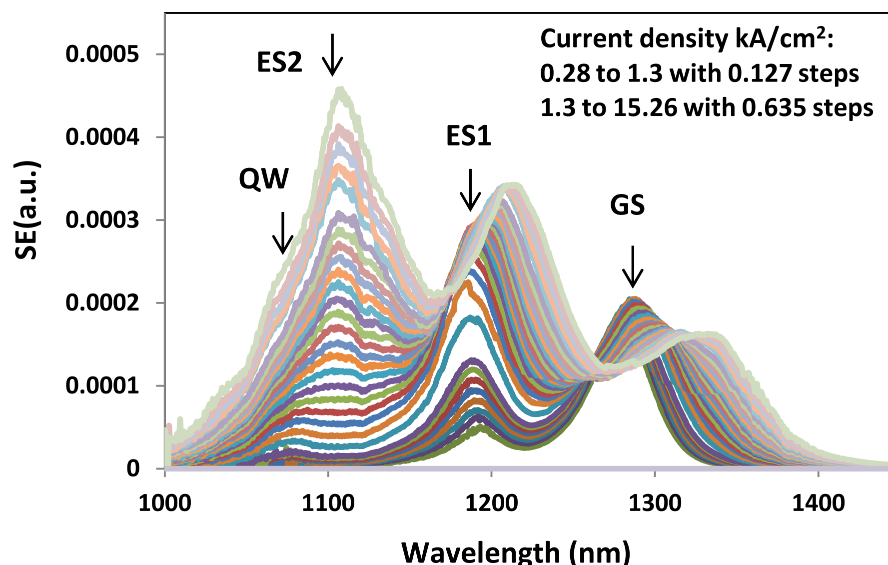

Figure 3.7: Spontaneous emission measurement of QLF1375-AE based SLD at room temperature.

As seen in figure 3.7, under CW operation of the device, a large carrier density is required in order to observe QW emission. A red-shift (~45nm) in the QD GS emission is observed indicating ~90°C increase in the junction temperature. A concomitant reduction in GS spontaneous emission intensity is also observed.

In order to further clarify the strength of QW emission, a Gaussian fit of the SE at current density of 15.26kA/cm^2 is plotted in figure 3.8. The fit is calculated to have the maximum R^2 value (0.995). The SE for ES2 is very intense as compared to the QW emission and was not observed in previous samples, where strong QW emission was readily achieved [1]. This is attributed to the high number of QDs (9 layers in comparison to 6 layers with 50% higher areal density) for the QD laser material as compared to previous University of Sheffield's samples (section 3.2).

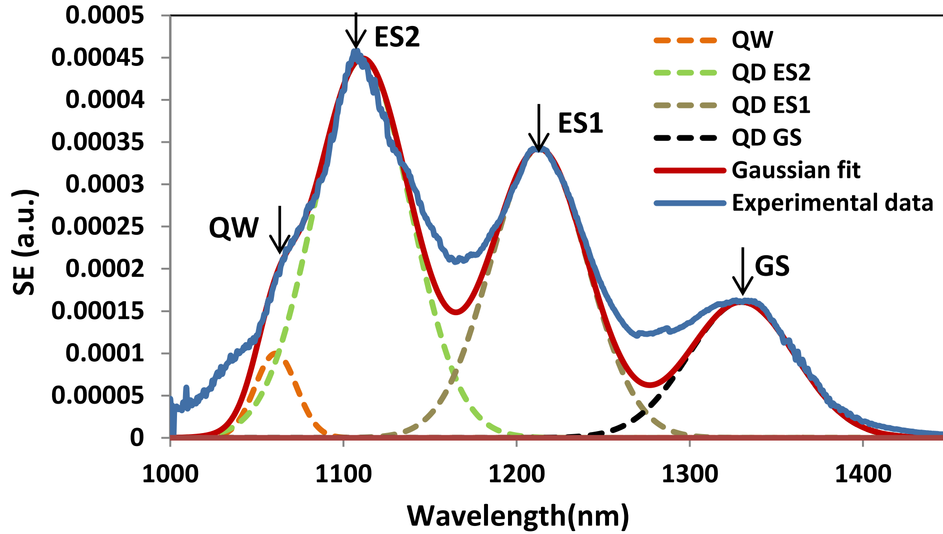

Figure 3.8: Gaussian fit of spontaneous emission at 15.26kA/cm^2.

The net modal gain at a range of currents (current density of 0.28 to 15.26 kA/cm^2) was determined as discussed in chapter one, and is plotted in figure 3.9. Gain peaks due to the GS and ES1 are clearly resolved in the gain spectra. The internal loss determined from the net modal gain measurement at long wavelength is ~5cm^{-1}. A saturated modal gain of ~40 cm^{-1} is obtained for the QD GS.

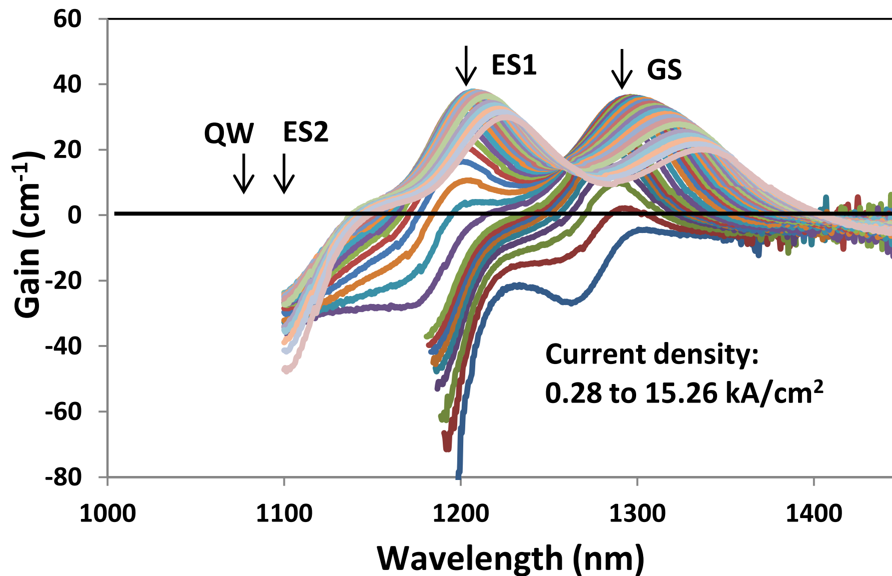

Figure 3.9: Continuous wave segmented contact gain measurement of the hybrid sample at room temperature.

Net modal gain peak values of the GS and ES1 versus the current density is plotted in figure 3.10. The GS gain of the device is saturated at ~ 4.47kAcm^{-2}. At higher current densities it decreases, and this is attributed to self heating of the device. The ES1 peak gain overtakes the GS at ~7.64 kAcm^{-2}. The peak gain then decrease due to the self heating of the device.

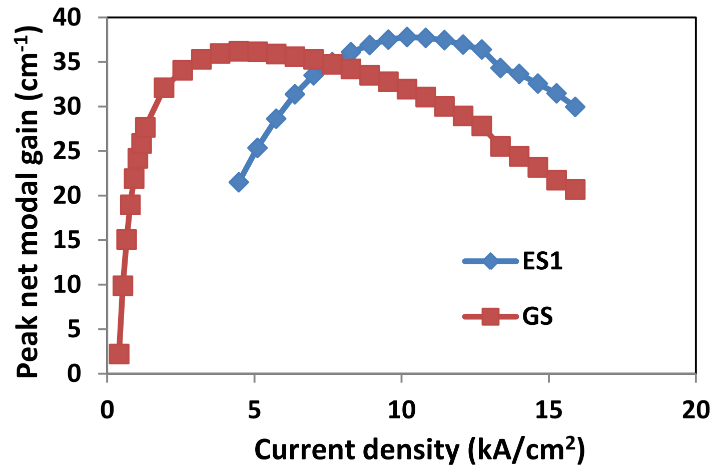

Figure 3.10: Peak net modal gain as a function of current density.

A blue shift in the GS and ES1 peak wavelengths at current densities below 1.27kA/cm^2 is noticeable which is attributed to the state filling of the QD states with an increase in excitation density. The red shift of the GS peak wavelength after this point is attributed to free carrier effects and self heating.

Due to indistinguishable signals it was not possible to measure the gain/loss at 1080nm (QW lowest state) with confidence but it is expected to be in loss in this range of current densities. The QW emission is clearly observed in SE graph (figure 3.7 and 3.8). This emission from the QW may be absorbed by the QDs and subsequently enhance the carrier capture rate, but the self heating effect is so large in these devices that the effect on the saturated SE and gain cannot be determined as their values are reducing with increasing current.

3.3.3 Mesa diodes

In this section, electroluminescence of devices based on three different wafer structures are studied and compared. The first set of samples were fabricated from wafer QLF1375-AD, which consists of 10 layers of quantum dots with designed ground state center wavelength of ~1280nm. This sample is considered as a reference or control sample and is very similar in design to QLF1375-AA. The second set of samples are based on wafer QLF1375-AG including one quantum well layer (~1080nm) and five layers of quantum dots (~1280nm) within the active element. The last sets of samples are based on wafer QLF1375-AI including chirped quantum dots (type A~1280nm, type B~1230nm) and a digital alloy quantum well layer (1080nm). All the wafers described in this chapter were grown by a commercial supplier, QD Lasers Inc. (Japan). In order to characterize the material properties, mesa diode structures with optical access windows were fabricated from all these wafers by Dr. Nasser Babazadeh based on standard fabrication process steps. The schematic is provided in figure 3.11(a). The walls of the diodes have been etched through the active layer to ensure well defined current injection. To prevent the device from lasing due to whispering gallery modes, the side-walls were scratched in order to stop the round trip of the light around the mesa wall.

Samples were mounted and bonded on tiles for cryostat measurements. A 47 ohm surface mount resistor was used for impedance matching to the pulsed current source, LDP-3811. The schematic is plotted in figure 3.11(b).

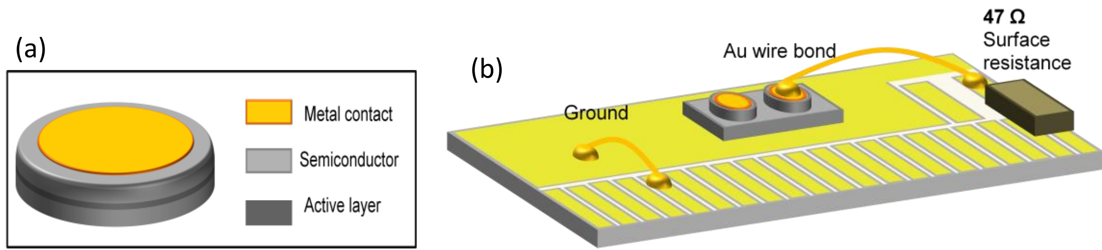

Figure 3.11: (a) Schematic of the mesa diodes with 100μm diameter (b) mounted and bonded samples.

To ensure that the self heating of devices has limited influence on the emission characteristics, pulsed measurements of spontaneous emission at room and low temperatures have been performed in a cryostat setup. Pulse widths within a range from 0.5 to 1μs and duty cycle of 2 to 10% have been utilized in these measurements. The setup schematic is shown in figure 3.12.

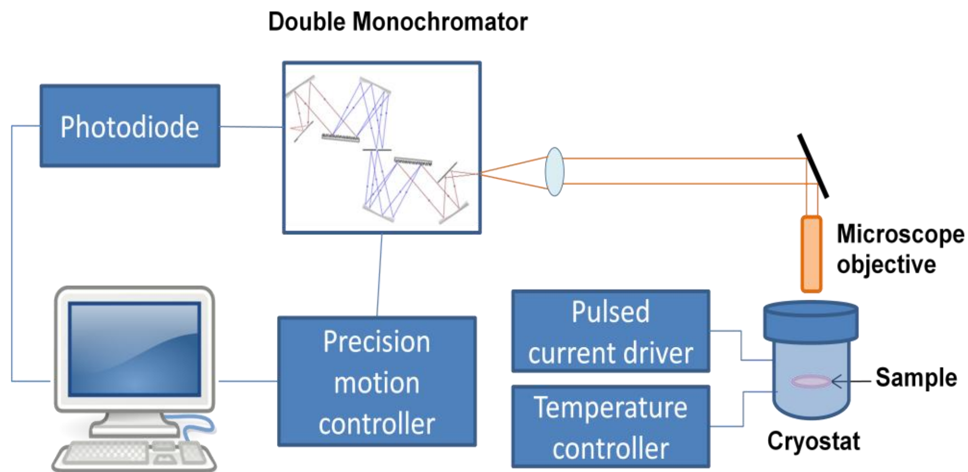

Figure 3.12: Schematic of cryostat setup for low temperature measurements.

The sample is placed in a variable temperature cryostat controlled by LakeShore-331 temperature controller. The sample is excited by a pulse current driver, ILX Lightwave-LDP 3811. The output light is then collected by an objective lens and is passed through a double monochromator, Bentham-DM150, in order to select the wavelength. A precision motion controller, Thorlabs- Apt, controls the monochromator. The intensity

of the selected wavelength is then measured by a photodiode connected to a Keithley-2000 multimeter, which is then recorded by the computer.

3.3.3.1 QD sample: QLF1375-AD

3.3.3.1.1 Wafer structure

The structure of wafer QLF1375-AD is shown schematically in figure 3.13, and includes ten layers of InAs quantum dot with InGaAs SRLs.

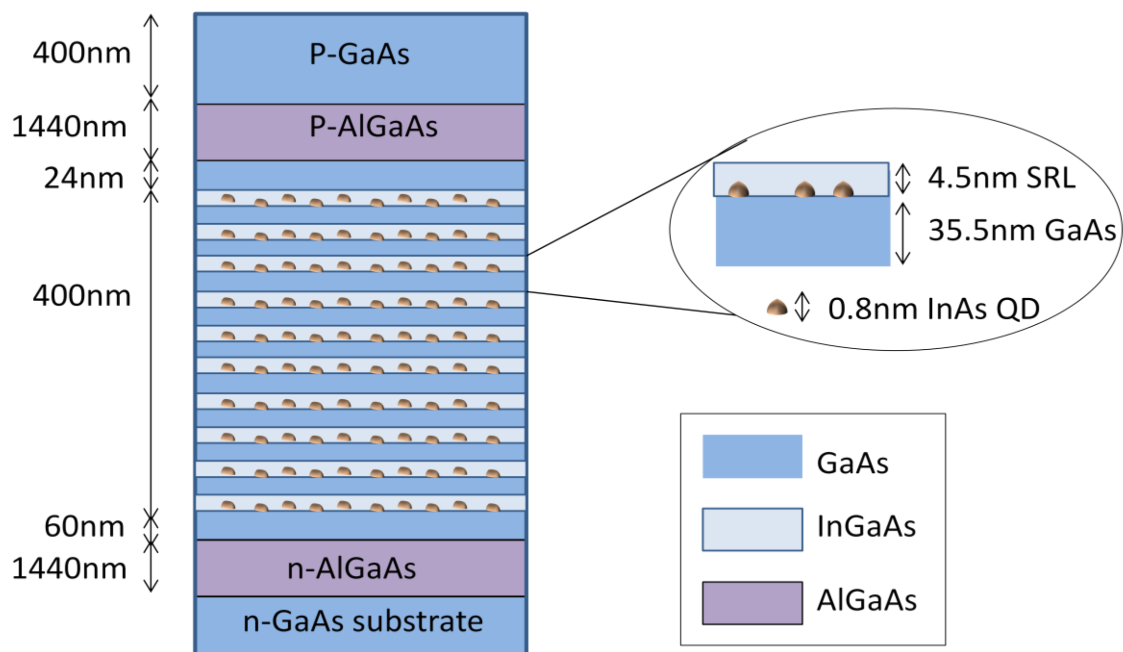

Figure 3.13: Schematic of QLF1375-AD wafer structure.

The epitaxy for this structure is essentially identical to the previous sample (QLF1375-AE) except for the growth of the active region which starts with 60nm of undoped GaAs following by 10 layers of InAs QDs layers. Each layer contains 0.8nm InAs, capped with 3.7nm InGaAs SRL. An undoped GaAs barrier layer (35.5nm) is inserted between the layers of QDs.

3.3.3.1.2 Experimental results

EL of the mesa diode was measured at room temperature and is plotted in figure 3.14. At low current densities, initially a peak is observed at 1280nm which is attributed to the QD ground state. This peak increases in intensity until it saturates which is accompanied by the increase in another peak at 1180nm which is attributed to the ES1 of the QDs. In addition, we can see a shoulder at 1100nm which is attributed to the ES2 of the QDs. Due to the dot occupancy being low (~6 e-h pair per QD) this feature is not comparable in size with other states. As the effect of gain or absorption through a single vertical pass of SE through the active element is expected to be negligible, the measured EL spectra are expected to be essentially identical to the SE spectra.

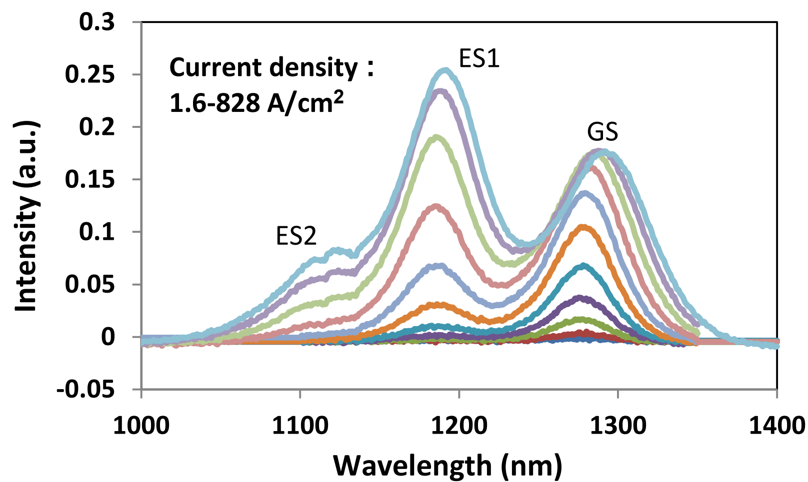

Figure 3.14: Electroluminescence of 100μm diameter mesa diode based on QLF1375-AD wafer.

Fitting this data with Gaussian curves allows the measurement of the current density dependence of the FWHM and peak wavelength of the states. An example of the data fitted to Gaussian curves is presented in figure 3.15. There is a slight mismatch observed between the fitted and the measured data, in particular between the GS and the ES1 due to a few limitations: Using three Gaussian curves to fit the experimental results and allowing the ES2 to be as broad as it is necessary to produce a good fit to

the data will result in an overestimation of the strength of ES2. Moreover, a poor fit in between GS and ES1 could be due to the fact that only the allowed (e_1hh_1 and e_2hh_2) transitions are considered. There is strong evidence from photocurrent (PC) data (courtesy Mr. Soroush Alisobhani) for the nominally forbidden transitions with a week oscillator strength contributing to the photocurrent spectra in this spectral region. This is evidenced by a clear non zero PC signal between the GS and ES1 peaks. As a consequence, data showing fits like that in figure 3.14 are considered as acceptable to deduce changes in the GS of SE.

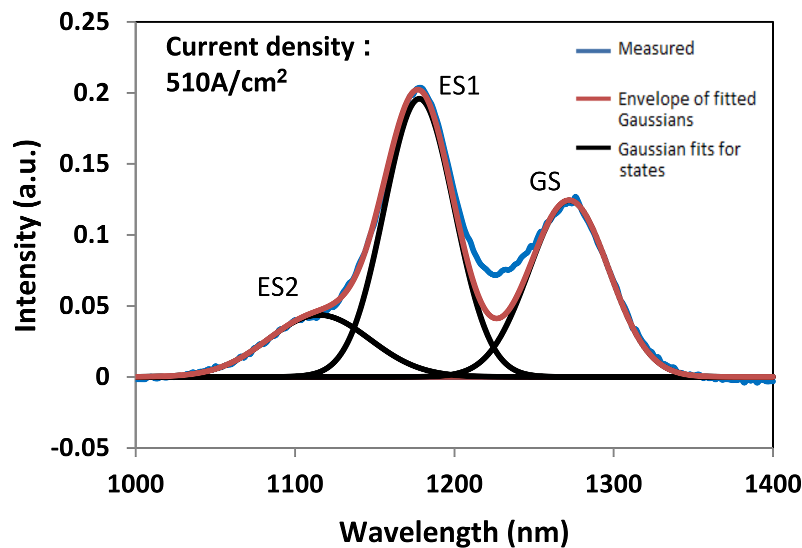

Figure 3.15: Gaussian fit of EL data at current density of 510A/cm^2 for sample QLF1375-AD.

Peak values of the states are plotted in figure 3.16 which shows the saturation of ground state around 200A/cm^2 by increasing the current density. Due to higher degree of degeneracy for the first excited state it is expected that the ES1 start to saturate at higher current densities. A probable overestimation of the ES2 state SE is noted again. The limitation of the current driver used didn't allow for higher current densities for this sample to get to the ES1 saturation point. This sort of behaviour for QD states by increasing the carrier density have been observed and well discussed by others [8].

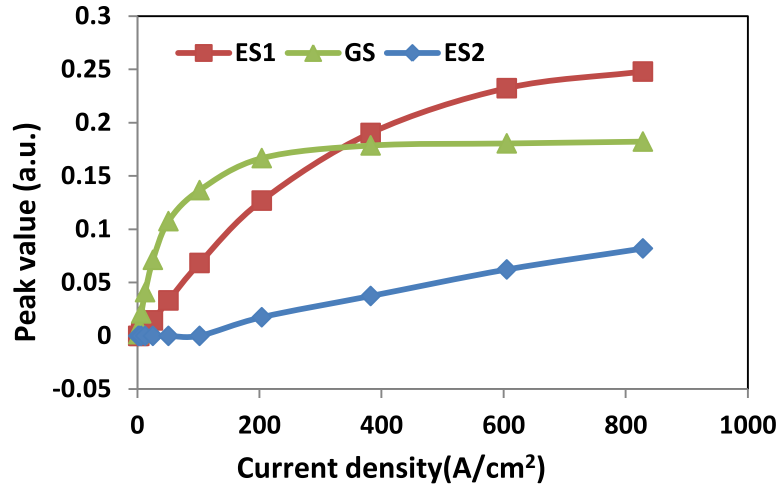

Figure 3.16: Peak value of EL emission for states of sample QLF1375-AD at room temperature.

Based on the fitted Gaussian curves, the FWHM and peak wavelength of the states are measured and plotted in figures 3.17 and 3.18, respectively.

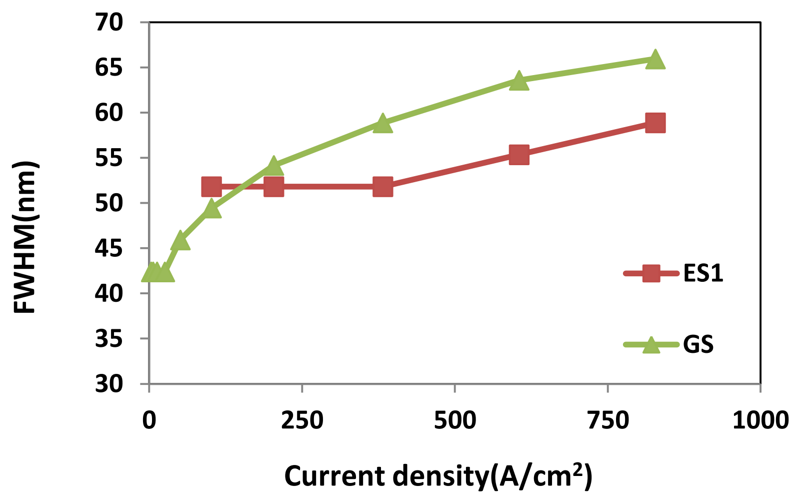

Figure 3.17: Current density dependence of FWHM of GS for sample QLF1375-AD.

The transition of the measured FWHM from ~40nm (30.4meV) to ~66nm (49.1meV) is observed in the ground state emission which is in good agreement with values observed by others [9,10,11]. At low current densities the FWHM is attributed to inhomogeneous broadening plus homogeneous broadening due to phonon scattering (at room temperature due to the thermal energy). At higher current densities free carrier effects and the Poisson broadening effect also contribute to the broadening [12]. The increase

in peak wavelength observed in the GS emission is attributed to self heating and free carrier effects as discussed previously in chapter 2.

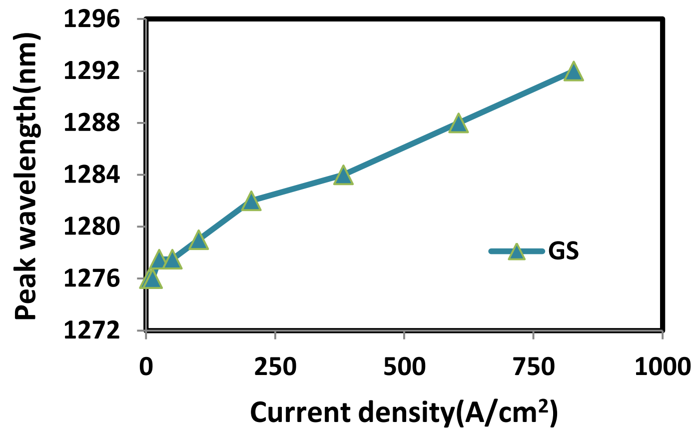

Figure 3.18: Current density dependence of peak wavelength of the GS for sample QLF1375-AD.

3.3.3.2 Hybrid QW/QD sample: QLF1375-AG

3.3.3.2.1 Wafer structure

A schematic of the wafer structure for QLF1375-AG is shown in figure 3.19 which includes five layers of quantum dots with ground state center wavelength of ~1280nm and one layer of InGaAs quantum well with ground state center wavelength of ~1080nm.

The quantum well layer is included in order to increase the gain bandwidth of devices [13]. By adjusting the e_1hh_1 emission of the quantum well layer to be resonant with the second excited state emission of the QDs, QW gain can dominate the QD ES2 absorption (loss) leading to broader bandwidth. Moreover, the reduced number of QD layers help QD saturation occur at lower current density than the previous samples (QLF1375-AD and QLF1375-AE with 10 and 9 layers of QDs, respectively), which makes it possible to unambiguously observe the effect of the QW on the QD layers more easily (see later).

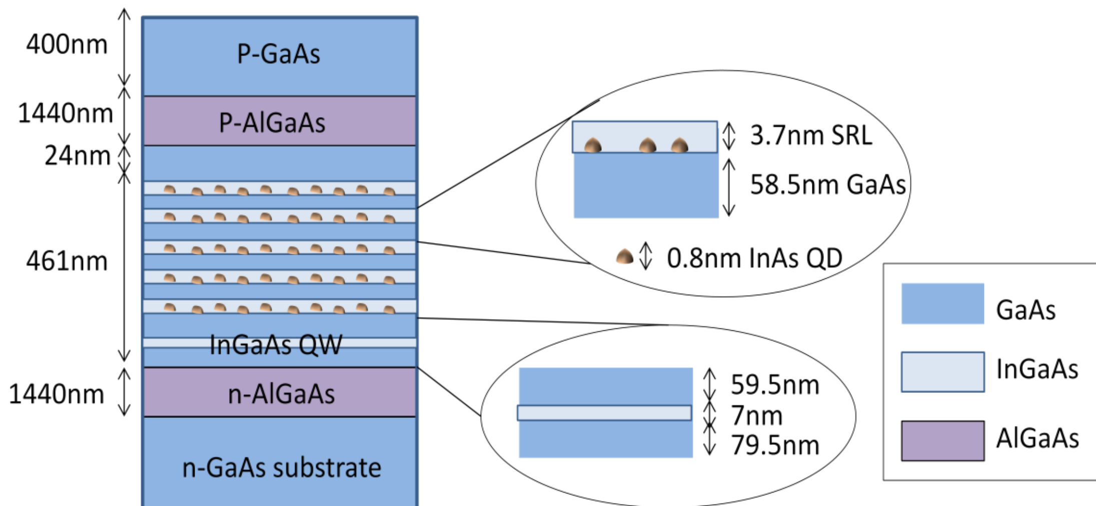

Figure 3.19: Schematic of QLF1375-AG wafer with 5 QD and one QW layers.

The epitaxy for this structure is essentially identical to the previous sample (QLF1375-AE) except for the growth of the active region which starts with 79.5nm of undoped GaAs and a 7nm $In_{0.29}Ga_{0.71}As$ single QW following by 59.5nm undoped GaAs barrier. Above the barrier five layers of InAs QDs layers were grown in a similar way to the previous sample (QLF1375-AD) but the undoped GaAs barrier layer thickness is chosen to be 58.5nm. This results in the core of the waveguide having the same thickness as the previously described sample.

3.3.3.2.2 Experimental results

Room temperature pulsed measurements of the surface emission from mesa diodes with QLF1375-AG wafer structure are plotted in figure 3.20.

Similar to the previous sample, at low current densities initially a peak is observed at 1280nm which is attributed to the QD ground state. By increasing the current density another peak appears at 1180nm which is attributed to the first excited state of the QDs. In this sample a peak at 1080nm is observed which is attributed to the QW due to it

having ~20nm shorter wavelength than the ES2 transition in figure 3.14, and being at the wavelength expected from PL measurements of test structures.

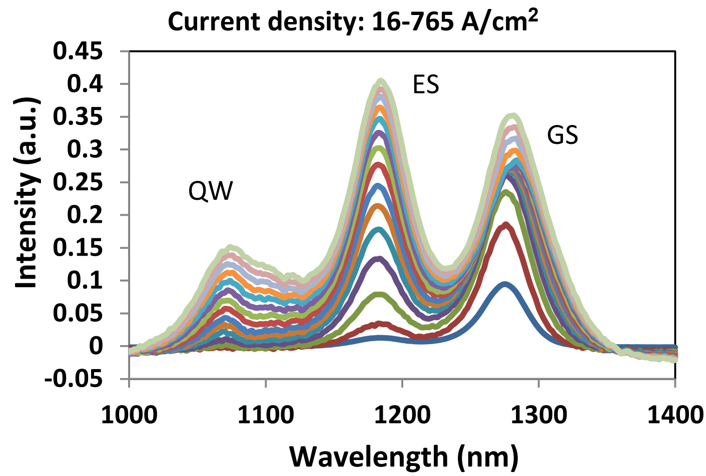

Figure 3.20: EL measurement of 100μm diameter mesa diode based on QLF1375-AG wafer.

The current density dependence of peak values of the spontaneous emission from these three transitions is plotted in figure 3.21. By contrast to the control sample with no QW (QLF1375-AD), following initial saturation, a clear increase in ground state spontaneous emission is observed at high current density (>500Acm^{-2}).

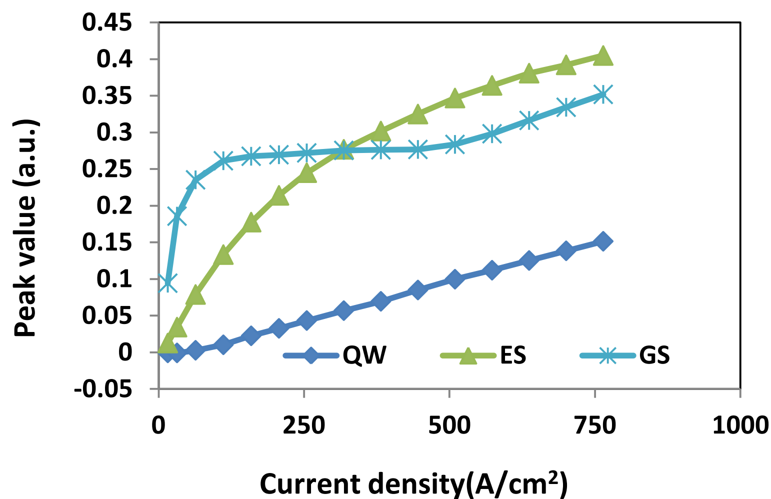

Figure 3.21: Peak values of states for QLF1375-AG sample.

The FWHM and peak wavelength of the ground state are plotted in figure 3.22(a) and 3.22(b), respectively. As in the case of control sample (QLF1375-AD with no QDs), both show an increasing trend up to around 500A/cm^2. Beyond 500A/cm^2 a reduction in both linewidth and emission wavelength is observed. The onset of the reduction in peak wavelength and FWHM coincides with the increase in GS SE at ~500A/cm^2 (figure 3.21). This behaviour contrasts that observed for the QD only structure, where peak wavelength and FWHM monotonously increased with current density, and clear saturation of the GS emission occurs.

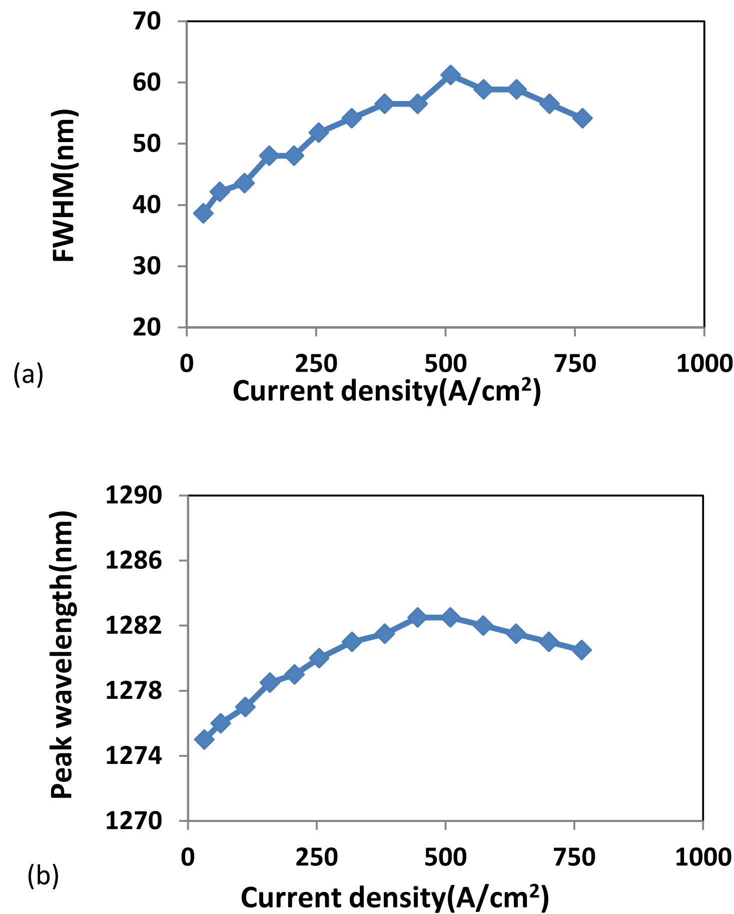

Figure 3.22: Characteristics of ground state EL emission of sample QLF1375-AG at room temperature (a) FWHM (b) peak wavelength.

3.3.3.2.3 Discussion

The uplift in GS peak which is observed in figure 3.21 does not exist in the sample with only QD layers (figure 3.16). It may be due to either increasing the radiative rate or more efficiently supplying carriers to the GS of the QDs. The coincidence of the increase in GS emission and reduction in FWHM and peak wavelength suggests that if the QW is optically pumping the QDs, then this is not occurring for the whole ensemble. Rather, this suggests that a subset of QDs is being preferentially excited. These current densities are quite reasonable and no previous reports of QD spectroscopy has indicated a curve similar to that displayed by the GS in figure 3.21.

Figure 3.23 schematically plots this process. The gain and spontaneous emission of a QD laser device is plotted in this figure showing that at 1080nm, non zero spontaneous emission exists while the gain spectra is in loss region.

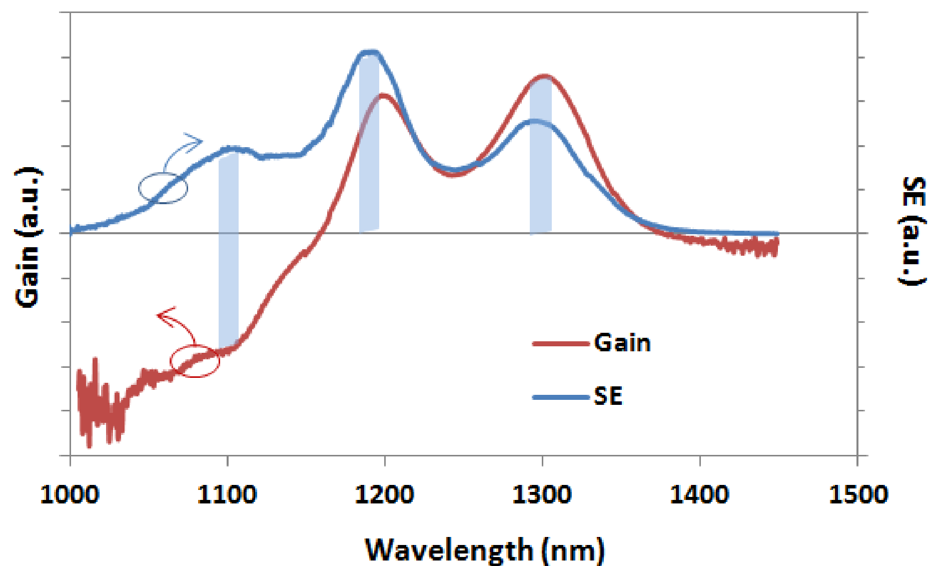

Figure 3.23: Gain and spontaneous emission of an active element containing QW. Schematically presenting the enhancement emission due to QDs which their ES2 is in resonance with QW.

The proposed model is that the subset of QDs which have absorption overlapping the QW emission peak, will have a spread of ES1 and GS peaks (all indicated by shaded regions in figure 3.23). As a result this selective preferential carrier supply to a subset of the ensemble leads to the peak wavelength shift and FWHM reduction.

In the following section, measurements are carried out on a special structure designed to have a broad emission spectrum to investigate if similar effects can be observed.

3.3.3.3 Digital alloy QW with chirped QDs: QLF1375-AI

3.3.3.3.1 Wafer structure

The wafer structure of QLF1375-AI is shown schematically in figure 3.24, and includes one QW layer and nine chirped quantum dot layers with GS center wavelengths around 1280nm (5 layers) and 1230nm (4 layers). This wafer has been designed in order to try to obtain wider bandwidth as well as more uniform emission profile. This is planned by spectrally positioning QDs to fill the gaps between the GS and ES emissions with the GS and ES emission of another set of QD layers.

This wafer also includes a digital alloy quantum well layer at 1080nm. The indium composition profile is plotted in figure 3.25 showing eighteen layers of InAs/GaAs in a thickness of 0.11nm/0.269nm to reproduce a ~6.822nm $In_{0.29}Ga_{0.71}As$ digital alloy QW. Detailed description of the growth of the digital alloy InGaAs QW is summarized in table 3.1. This is carried out in an attempt to minimise indium segregation effects.

The epitaxy for this structure is essentially identical with the previous samples (QLF1375-AD and QLF1375-AG) except for the growth of the active region.

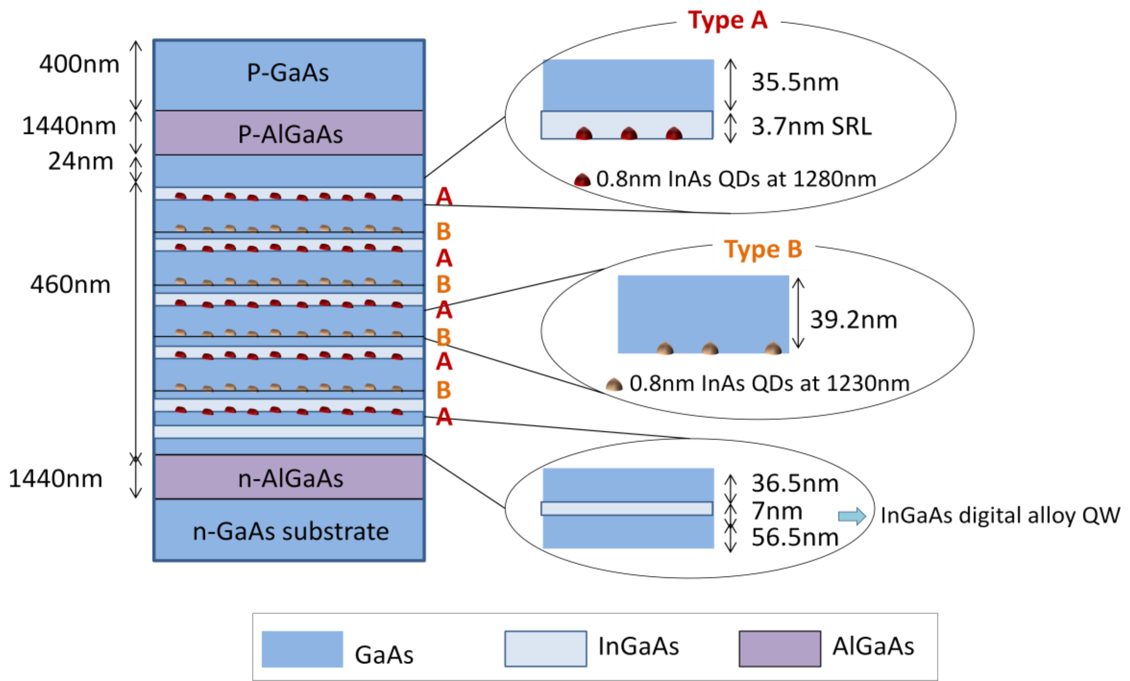

Figure 3.24: Schematic of QLF1375-AI wafer structure.

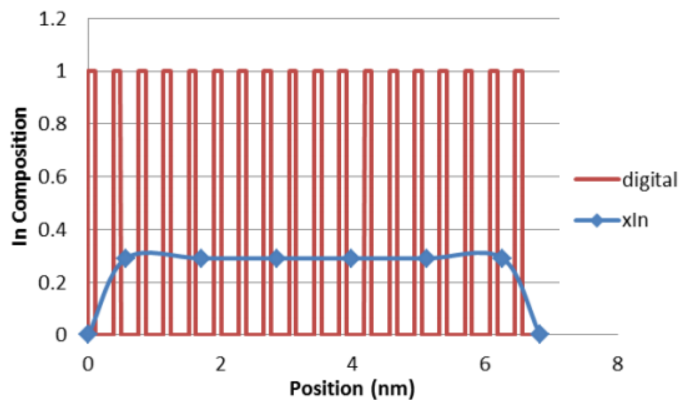

Figure 3.25: Indium composition profile for sample QLF1375-AI.

xIn	InAs(nm)	GaAs(nm)	loop	In (sec)	Ga (sec)	thickness (nm)	comm thick	position	xIn	In*thick
								0	0	
0.290237	0.11	0.269	3	1.98	2.421	1.137	1.137	0.5685	0.29024	0.33
0.290237	0.11	0.269	3	1.98	2.421	1.137	2.274	1.7055	0.29024	0.33
0.290237	0.11	0.269	3	1.98	2.421	1.137	3.411	2.8425	0.29024	0.33
0.290237	0.11	0.269	3	1.98	2.421	1.137	4.548	3.9795	0.29024	0.33
0.290237	0.11	0.269	3	1.98	2.421	1.137	5.685	5.1165	0.29024	0.33
0.290237	0.11	0.269	3	1.98	2.421	1.137	6.822	6.2535	0.29024	0.33
		total loop	18					6.822	0	
										1.98
					Well thickness	6.822			average xIn	0.290237

Table 3.1: details of growth of InGaAs digital QW for wafer QLF1375-AI.

The active region in wafer QLF1375-AI starts with 56.5nm of undoped GaAs and 7nm digital alloy InGaAs QW (1080nm emission wavelength). This is followed by five-layers of type A InAs QDs (1280nm emission wavelength) and four layers of type B InAs QDs (1230nm emission wavelength) in the sequence of A/B/A/B/A/B/A/B/A as shown in figure 3.24. 3.7nm InGaAs SRL was used for type A QDs while for the type B, QDs were covered by a GaAs capping layer. The total active core thickness is the same as samples discussed previously.

3.3.3.3.2 Experimental results

Pulsed source EL measurements of the QLF1375-AI mesa diodes were carried out at room temperature. The resultant spectra and the current density dependence of peak values for the fitted states are shown in figure 3.26 and 3.27, respectively. In addition to the peaks at ~1280nm and ~1180nm which are attributed to the GS and ES1 of type A QDs, two more peaks attributed to the GS and ES1 of type B of QDs are clearly observed at ~1220nm and ~1130, respectively. The effect of chirped QDs on the emission spectra is the reduction in modulation of the spontaneous emission. The peak around 1080nm is attributed to the lowest QW state.

As expected, the GS of the QDs is saturated with increasing current density. Further increase in current leads to more intense ES1 emission of both sets of QDs, but to get to the saturation point of these states high level of carrier density is required which was not possible with the drivers available.

Current density dependence of full width at half maximum and peak wavelength values for states are plotted in figures 3.28(a) and (b).

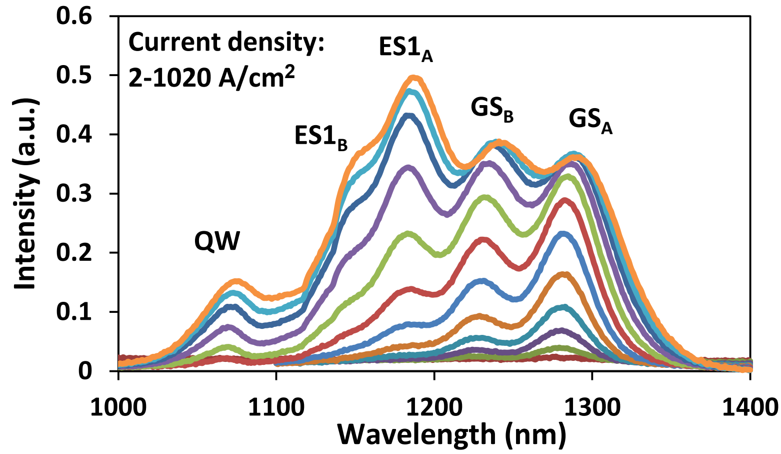

Figure 3.26: EL measurement of 100μm diameter mesa diode based on QLF1375-AI wafer at room temperature.

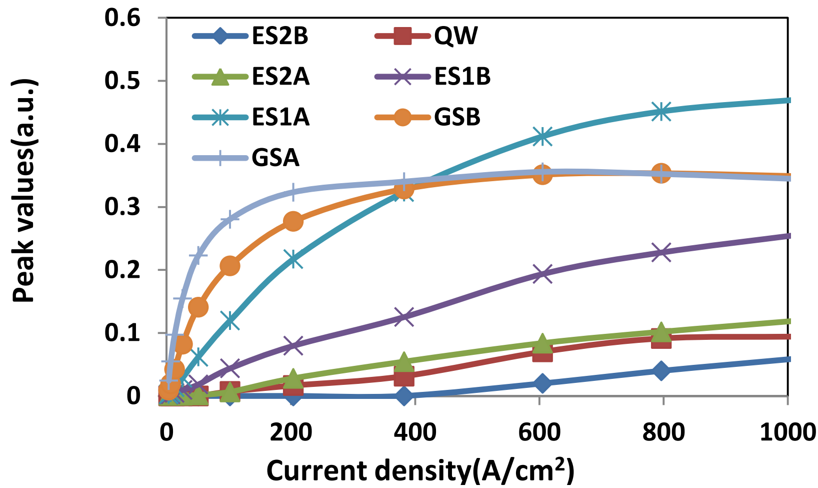

Figure 3.27: Peak values of fitted states for mesa diode based on QLF1375-AI wafer.

Unfortunately for this sample, the data for higher current densities could not be obtained due to limitations in the amount of applied current. As a result, an increase of GS peak value after the saturation point due to optical pumping by the QW is not clearly observed. It is noted that in comparison to the QD emission, the QW emission is comparatively weaker than the case for sample QLF1375-AG where effects of optical pumping were observed. The optical pumping effect of the QW may be more clearly observed by characterizing this sample at low temperature due to higher QW emission intensities being possible.

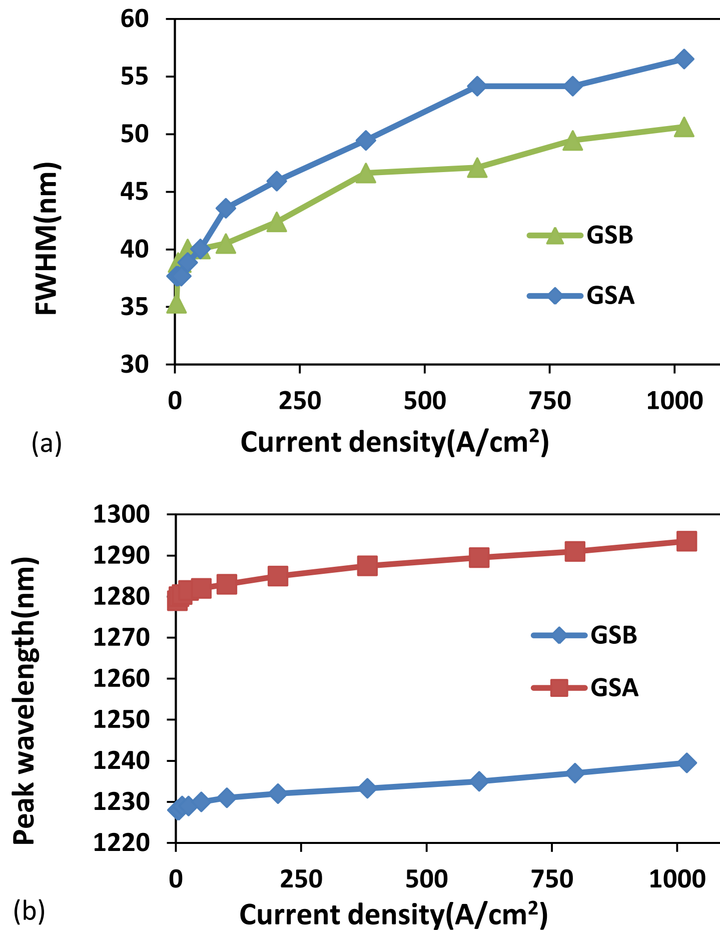

Figure 3.28: Current density dependence of (a) FWHM and (b) peak wavelength for states of sample QLF1375-AI at room temperature.

The EL spectra at 14K are presented in figure 3.29. By increasing the current density peaks at ~1180nm and ~1095nm which are attributed to the GS and ES1 of type A QDs plus two more peaks attributed to the GS and ES1 of type B of QDs at ~1140nm and ~1080 are clearly observed. The peak around 995nm is attributed to the lowest QW state. As expected QW's emission intensity is much stronger in comparison to EL measurements of the same sample at room temperature. As discussed previously a strong QW emission in comparison with QD emission is required to see the optical pumping effect.

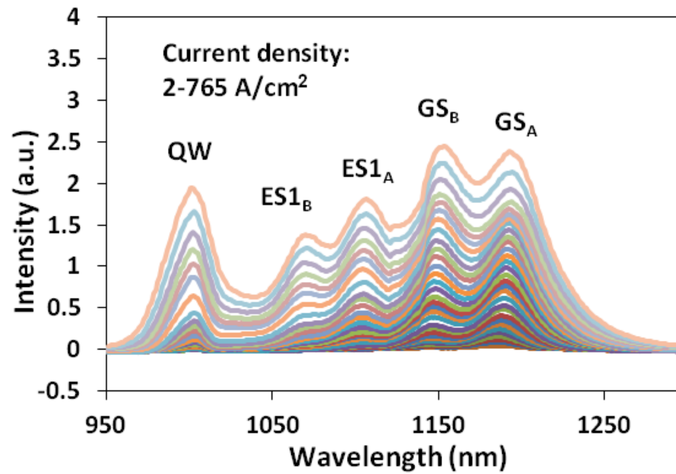

Figure 3.29: EL spectra at 14K for QLF1375-AI mesa diode.

The peak values of states are plotted in figure 3.30. There is a continuous rise in SE for all QD states which is attributed to high QW emission intensity even at low current densities which prevents the QD states being observed to saturate. This result suggests optical pumping effects are at play here too at low temperature.

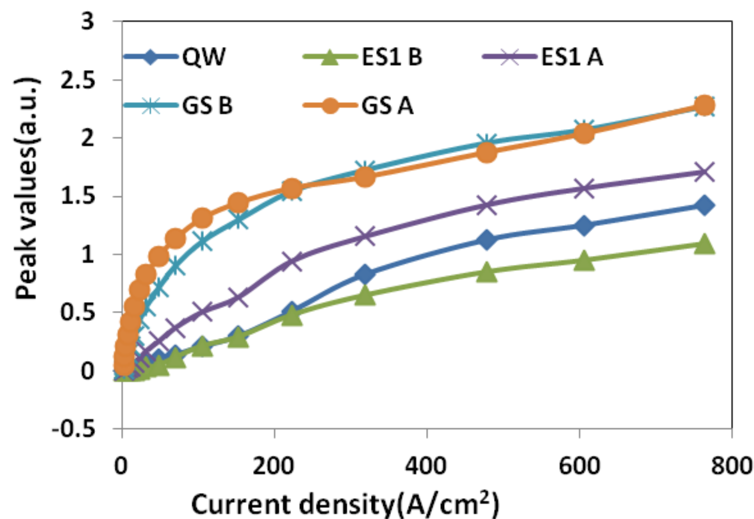

Figure 3.30: Peak values of fitted states for 100µm diameter mesa diode based on QLF1375-AI wafer at 14K.

The effect of optical pumping of the QDs by the QW emission at room temperature could not be observed. This is attributed to the fact that this sample has nearly double the number of QD layers in comparison to the QLF1375-AG sample. At low temperature we are able to reduce non-radiative recombination leading to longer carrier lifetime and therefore more light emission for a given injected current density could be

obtained. Because of the longer carrier lifetime, saturation at the states should occur at even low current densities. So any saturation based effects are more prominent. Also at low temperature more QW emission is expected as compared to QD emission [13] resulting in brighter QW and therefore a greater optical pumping effect. The monotonous increase in SE is attributed to QW optically pumping the QD ensemble, as observed for the 6 layers of QD sample in section 3.2.

3.4 Summary

In this chapter lasing behaviour of the hybrid QW/QD samples have been discussed and the effects of quantum well layer on QDs have been studied. The sequence of lasing in the lasers based on these structures suggests that emission from the QW layer is influencing the device characteristics. Structurally different samples have been investigated in order to verify the possible origins of this effect. Results show evidence that emission from the quantum well layer is modifying the QD emission. This is in terms of the emission spectrum (peak position and FWHM) and an increase in the intensity of the GS following apparent saturation. This optical pumping of the QDs is tentatively associated with the previously observed higher gain for dots at higher current densities even after saturation.

3.5 Future work

Direct measurement of gain of the QDs increasing under high levels of QW emission is required. For the SLD structure which was analysed in this chapter, self heating effects were the main reasons for being unable to clearly show the optical pumping of the QDs. To solve this problem, either low temperature measurements or new samples with fewer QD layers would help us to obtain a stronger QW emission. For this purpose,

custom wafers can be grown with only one or two layers of QDs next to the QW layer. Also, a chirped QD sample with similar structure as QLF1375-AI with no QW layer can be used in order to investigate the band filling effects at different temperatures and highlight the role of QW layer in the hybrid sample.

The Monte-Carlo model presented in the second chapter can be used in order to optimise the design of chirped sample with the aim of flat and broad gain spectra.

The lowest energy level of the QW in the hybrid sample QLF1375-AG was ~20nm shorter than the ES2 of QD layers. In future, a similar sample but with QW lowest state offset of 20nm to the longer wavelength or at the ES2 centre wavelength can be designed. For such a sample, the shift in the peak wavelength and FWHM can be investigated with regard to the QW optical pumping effect.

One method of measuring gain is Hakki-Paoli but observing GS gain during QW lasing is problematic due to difficulties in rejecting laser light in the optical spectrum analyser. Multi-section measurement with high QW emission may be the easiest method.

Moreover, for hybrid QW/QD lasers, if the QD GS lasing is due to the QW optical pumping effect, then one can argue that the modulation rate of the laser should be faster since the fast carrier dynamics of QW can be imprinted to the QD GS leading to faster modulation rates. However, this would be a rather inefficient modulation scheme. This effect may be harnessed in all-optical signal processing where a ~1100nm signal could be transferred to 1300nm without the need to enter the electrical domain.

References

[1] S. Chen, K. Zhou, Z. Zhang, J. R. Orchard, D. T. D. Childs, M. Hugues, O. Wada, and R. A. Hogg, “Hybrid quantum well/quantum dot structure for broad spectral bandwidth emitters,” IEEE J. Select. Topics Quantum Electron., 19, 1900209, (2013).

[2] S. Chen, K. Zhou, Z. Zhang, O. Wada, D. T. D Childs, M. Hugues, and R. A. Hogg., “Room temperature simultaneous three-state lasing in hybrid quantum well/quantum dot laser,” Electron. Lett., 48, 644 (2012).

[3] S. Chen, K. Zhou, Z. Zhang, D. T. D. Childs, M. Hugues, A. Ramsay, and R. Hogg., “Ultra-broad spontaneous emission and modal gain spectrum from a hybrid quantum well/quantum dot laser structure,” Appl. Phys. Lett., 100, 041118 (2012).

[4] S. K. Ray, K. M. Groom, R. R. Alexander, K. Kennedy, H. Y. Liu, M. Hopkinson and R. A. Hogg, “Design, growth, fabrication and characterization of InAs/GaAs 1.3m quantum dot broadband superluminescent light emitting diode,” J. of Appl. Phys., 100, 10, 103105 (2006).

[5] H. Shahid, D. T. D. Childs, B. J. Stevens, and R. A. Hogg, “Negative differential gain due to many body effects in self-assembled quantum dot lasers,” Appl. Phys. Lett. 99, 061104 (2011).

[6] B. W. Hakki and T. L. Paoli, “Gain spectra in GaAs double-heterostructure injection lasers,” J. Appl. Phys. 46, 1299 (1975).

[7] V. M. Ustinov, A. E. Zhukov, A. Y. Egorov, and N. A. Maleev, “Quantum dot lasers,” Oxford, New York (2003).

[8] S. Osborne, P. Blood., P. Smowton, J. Lutti, Y. C. Xin, A. Stintz, D. Huffaker, and L. F. Lester, “state filling in InAs quantum-dot laser structures,” IEEE J. Quantum Elect., 40, 12 (2004).

[9] M. Sugawara, K. Mukai, Y. Nakata, H. Ishikawa and A. Sakamoto “Effect of homogeneous broadening of optical gain on lasing spectra in self-assembled $In_xGa_{1-x}As$/GaAs quantum dot lasers,” Phys. Rev., 61, 7595 (2000).

[10] M. Lorke, J. Seebeck, T. R. Nielsen, P. Gartner, and F. Jahnke “Excitation dependence of the homogeneous linewidthsin quantum dots,” phys. stat. sol. (c) 3, 7, 2393–2396 (2006).

[11] K. Matsuda, K. Ikeda, T. Saikic, H. Saito and K. Nishi, “Carrier–carrier interaction in single $In_{0.5}Ga_{0.5}As$ quantum dots at room temperature investigated by near-field scanning optical microscope,” Appl. Phys. Lett., 83, 2250, (2003).

[12] M. Grundmann and D. Bimberg, "Theory of random population for quantum dots," Phys. Rev. B 55, 15, 9740 (1997).

[13] S. Chen, "Hybrid quantum well/quantum dot structure for broad spectral bandwidth emitters," PhD thesis, Department of Electronics and Electrical Engineering, University of Sheffield (2013).

Chapter 4: Broadband Swept Light Sources for Optical Coherence Tomography Applications

4.1 Introduction

To begin, I present an introduction to the swept light sources (SLS) used in optical coherence tomography applications. With a literature review, I will show the common methods of implementing these swept sources. In this thesis SLS refers to short ring cavity configurations (~meters). This is followed by long cavity swept source lasers (the Fourier domain mode locked lasers) and their implementation methods.

Benefiting from an inhomogeneously broadened emission and gain, QD-SOAs can be considered as potentially interesting active devices in SLSs. Previously, a swept source laser (SSL) based on QD-SOA has shown 94nm bandwidth with 16mW output power [1]. In order to increase the bandwidth, possible options are investigated in this chapter incorporating different cavity configurations. A 17nm increase in bandwidth is achieved by using multiple QD-SOAs in a SSL in comparison to the previous work. Moreover, a complimentary QD-SOA and QW-SOA SSL, is investigated and a spectral coverage of 154nm is achieved. Future opportunities for this to be increased to ~220nm are discussed. Finally, a filtered ASE source with a spectral coverage of 225nm is described and routes to improve this structure have been discussed.

4.2 Light source

As described in chapter 1, one of the key components in swept source OCT (SS OCT) is the light source. The general requirements of sources to be used in SS OCT systems can be summarized as follow [2-4]:

- Emission in the near infrared for imaging in biological tissues. The optimum source wavelength can be determined by the required penetration depth, optical absorption and backscatter contrast, ensuring adequate penetration of light into the tissue.
- High irradiance. Since skin tissue is turbid, most of the light is scattered and lost so does not contribute to the received signal. This problem increases with depth, so more power means more depth to the image. However, a source power greater than a few milliwatts can provide adequate dynamic range.
- The wavelength sweep range defines the axial resolution. The broader the sweep bandwidth (sweep range), the higher the resolution.
- The instantaneous lineshape of the swept light source limits the depth over which images can be taken. The narrower the instantaneous linewidth, the longer the instantaneous coherence length, therefore, deeper imaging of the tissue is achievable. This is referred to as “roll off” of sensitivity. The sensitivity exponentially falls off with depth as the visibility of higher fringe frequencies decrease.
- The sweep speed needs to be fast enough to reach video rate acquisition times. The sweep frequency of a cavity SLS depends on the length of the cavity, the gain of the active element and amount of loss inside the cavity. To obtain fast sweeping rates in a SLS the simplest method is to shorten the cavity length. Increasing the gain can be problematic in terms of high current densities and self-heating effects since the gain in active element cannot exceed a defined value. Reducing the loss is possible in choosing components with low insertion loss and fusion splicing components together rather than using connectors.

In the simplest structure of a swept light source different sections can be defined as:

- An active element to provide light amplification.
- A tunable filter section to select the required wavelength.
- A feedback path which can be implemented in free space or optical fiber.

4.2.1 Semiconductor optical amplifiers (SOA) as gain medium

Thanks to the advanced techniques in semiconductor device design and fabrication, SOAs are one of the most permissive candidates for many optical applications. Beside all the functional applications they provide such as optical switches, modulators and wavelength convertors, they can also be utilized as an optical gain block for a swept source laser, benefitting from their amplification properties.

The invention of the SOA occurred at nearly the same time as the semiconductor laser in the 1960's, with a focus on the 830nm wavelength range operation [5]. During the subsequent years there have been a range of improvements in design and fabrication of these amplifiers. Since the original GaAs based devices, development of InP/InGaAsP SOAs provided the possibility of operation at 1300nm [6].

The structure of an SOA is based on the same technology as a Fabry-Perot diode laser, but utilises techniques to prevent the device from self oscillation. These travelling wave amplifiers (TWA), as single pass gain media, can be implemented either by tilting the waveguide with respect to the facets or antireflection (AR) coatings can be applied on the cleaved facets. These two methods are often used simultaneously to ensure the single pass of light without cavity effects. Figure 4.1 plots schematically two different structures for SOAs.

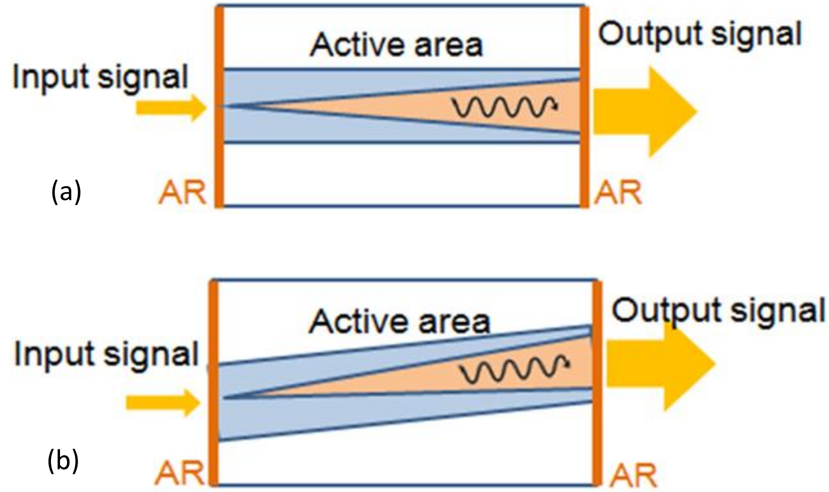

Figure 4.1: SOAs, (a) TWA with antireflection coating at the facets, (b) TWA with angled waveguide and AR coatings.

A typical effective reflectivity of a normal incidence AR coated facet (figure 4.1(a)) is 10^{-3}. A value for a well designed angled facet is typically 10^{-6}. This change in reflectivity makes the threshold gain larger for an angled facet, as in equation 4.1. For example for a 1mm chip without internal loss, with AR coated facets the threshold gain is 69cm^{-1}, whilst it is 138cm^{-1} for a tilted ridge, making angled facet SOAs more preferable.

$$G_{th} = \alpha_i + \frac{1}{2L}\ln\left(\frac{1}{\mathrm{R}_1\mathrm{R}_2}\right) \qquad (4.1)$$

Where α_i is the internal loss, L is the length of device and R_1 and R_2 are the reflectivity of the facets.

The operation of a SOA can fall into two regimes:

- Linear regime: This condition occurs when the input signal is small enough so the stimulated emission rate in comparison with spontaneous emission rate is negligible. In this case the steady state carrier density is independent of the position in the waveguide and gain can be calculated simply as $G = e^{Lg}$ where g is the net modal gain.

- Gain saturation: In the case of a large input signal, the local stimulated emission rate cannot be ignored. In this case the photon density near the output end of the SOA would be very large leading to an increase in stimulated emission rate which in turn acts to reduce the carrier density. If carriers cannot be supplied fast enough, the carrier density will be depleted and the gain will reach its saturation point. Therefore, photon and carrier density are dependent on the position in the waveguide as plotted in figure 4.2. A SOA to be utilised as an amplifier is preferred to be driven at its linear regime, since at the gain saturation regime distortion appears at the output power.

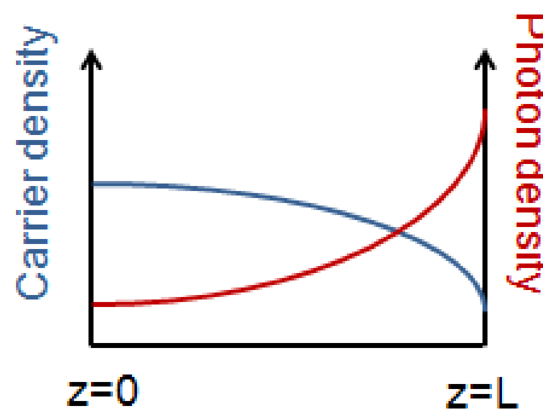

Figure 4.2: Length dependent photon and carrier density in a saturated SOA.

Some of the key parameters required for an SOA can be summarised as low insertion loss, reflectivity and polarization sensitivity, and high material gain and output saturation power. All these parameters cannot be achieved simultaneously and a trade off is expected. SOAs based on QW active area are polarization sensitive with a TE mode greater than TM due to hydrostatic strain pushing light hole energies up relative to the heavy hole band-edge in commonly used strained QWs. Moreover, different confinement factors in the waveguide for TE and TM modes makes SOAs sensitive to the polarization and therefore different amplification of the two polarizations in the active region. In the case of QD-based devices, the bandgap energy can be adjusted by

the choice of material, hydrostatic strain and the size of QDs. By adjusting the strain profile splitting between light and heavy hole bands can also be adjusted, making them more sensitive to TM mode than TE [7].

In order to enhance the bandwidth in SLSs with SOA as gain medium, one should bear in mind that both optical loss and parasitic lasing from the residual reflections limit the operation of the light source. To explain this limitations figure 4.3 plots a gain spectrum for a standard SOA. The loss resulting from (very) long fibers, connectors and splitters limits the lowest amount of required gain while the upper limit is defined by the parasitic lasing due to unintentional reflections from connectors, splices, splitters, etc.. Whatever the configuration of the swept laser cavity, the gain should be kept between these values. In order to obtain the widest bandwidth, usually a drive current to the SOA is selected to give a gain just below the parasitic lasing level, or more realistically, the point below which the ripple from the parasitic cavity affects the smooth sweep output of the laser.

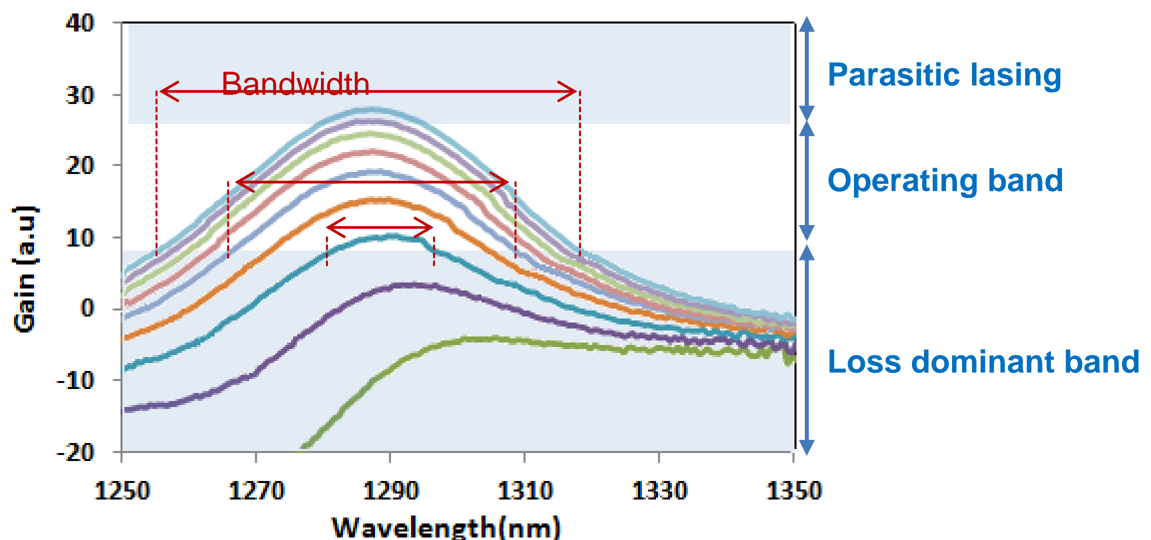

Figure 4.3: Possible operating band for OSA

4.2.2 Filter section

In addition to the SOA a filter section to select the required wavelength is needed to realize the swept light source. In the case of using reflective filters in the configuration, they are considered as a part of the feedback path. If the filter is transmissive then a loop will be required to provide the feedback in the cavity. Different types of filters that can be used in swept light source configuration are summarized in table 4.1.

Filter type	Sweep Speed	Comment
Motorised grating	very slow <<10Hz	The traditional monochromator
Birefringent filter	Slow	Used in Ti Sapphire and solid state lasers, (kHz)
Galvo mirror/ diffraction grating	100's Hz typical	Resonant design can achieve ~10kHz
Polygon mirror and diffraction grating	~10kHz	High speed rotating drum with multifaceted mirrors. Mechanical wobble can be a problem
MEMS mirror/grating	100's kHz	Miniature, potentially cheap and robust
Tunable FFP filter	~100kHz operating speeds	Piezoelectrically adjustable Fabry-Perot cavity filter. Fibre coupled.
Tunable semiconductor filters	ns tuning enabling >MHz repetition rates	Bragg reflector FP or ring resonators. Index change small.

Table 4.1: Filter options for swept source lasers

As discussed in this table, a range of filters can be used in the SLS structure, each with a different operating speed, and various pros and cons. In this chapter two types of filters are used: a traditional galvo mirror with a diffraction grating and a tunable Fabry-Perot filter. The galvo mirror in comparison with the other available options is rather slow, operating in the range of ~100Hz, but is straightforward to implement in a free space design for Littrow and Littman cavities. The tuneable fibre fabry perot filter is simple to implement in a fibre based system, and can achieve 100kHz sweep speeds. For higher speeds beyond this, integrated semiconductor tunable filters can be used to reach MHz range of speeds.

4.2.3 Swept light source configurations

Frequency swept sources with narrow linewidth generally can be implemented in two different configurations, as summarized in figure 4.4. In the first category, called “cavity tuning”, the filter is placed inside of the resonator cavity. In this case only the wavelength which passes through the filter is amplified and may start to lase. The problem with this type of setup is the slow operation speed since the lasing needs to be built up from ASE each time the filter’s wavelength changes. However, due to the multiple passes of the filter, the instantaneous bandwidth of the output will be narrower than the bandwidth of the filter transmission curve. In the second category, which is called “post filtering”, a broadband light source is used and the bandpass tunable filter’s job is to eliminate all the unwanted wavelengths. This setup has a low output power because of filtering the low power per unit bandwidth of spontaneous emission that, once filtered, means low power, compared to lasing where the power is in a very small bandwidth and so filtering does not cut out most of the power. In this case no lasing is expected to happen, and the output will essentially be a direct copy of the filter transmission.

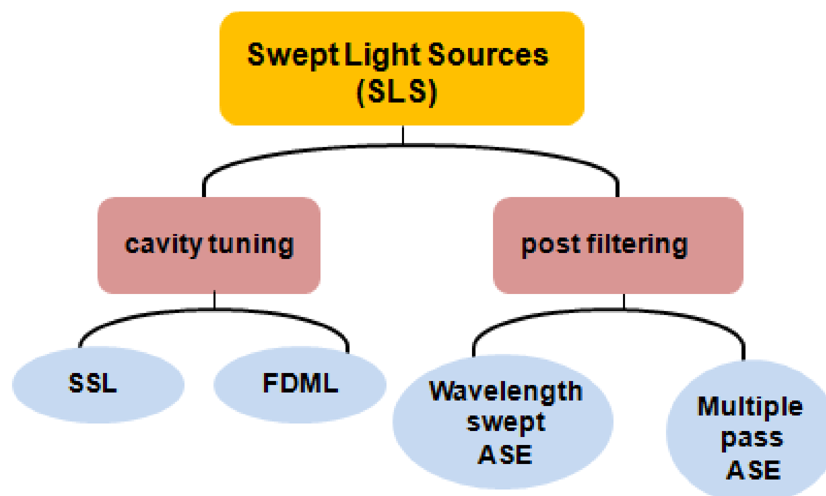

Figure 4.4: SLS configurations and examples of each category.

Commercial SSLs are implemented in “cavity tuning” configuration. In a standard SSL, as shown schematically in figure 4.5 [8], a broadband light spectrum is generated by the active element (spontaneous emission) and this also gets amplified each time the light passes through it (since it is operated in the regime of stimulated emission, which is optical gain). The loop is usually implemented by optical fibers, which provides the feedback path for the light. The filter section which sweeps in wavelength selects the instantaneous wavelength and filters out all other wavelengths. Therefore the output would only contain the amplified filtered wavelength and can even be amplified again to higher output powers by an external output SOA. The isolators are normally utilized in order to assure unidirectional circulation of light in the cavity and are essential in order to eliminating intra-cavity reflections. The main source of reflection in this case is from the Fabry Perot filter, since all the wavelengths that are not transmitted are reflected back.

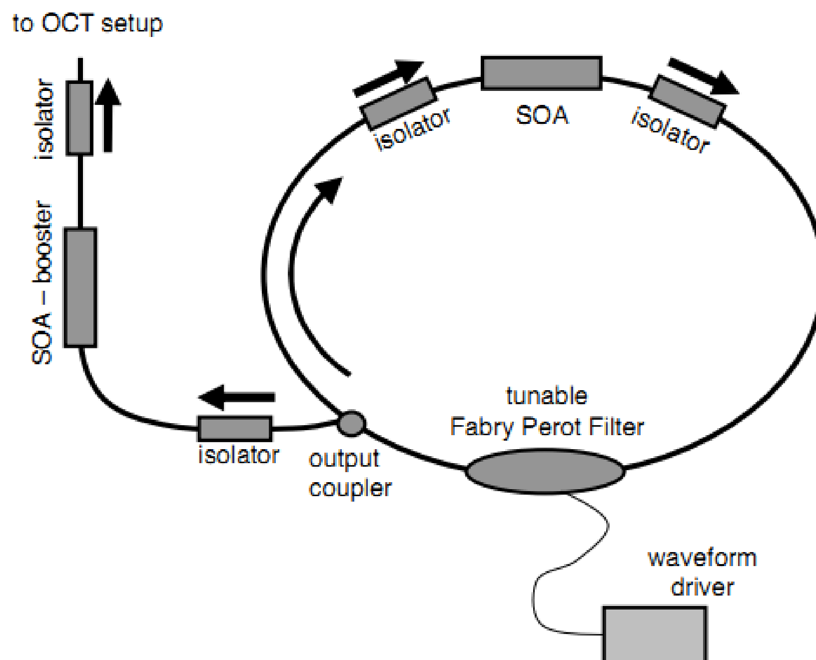

Figure 4.5: Schematic of a standard SSL. The laser uses a fiber coupled SOA as the active element and a FFP-TF as filter section. The feedback is provided by the fiber cavity. The purpose of SOA at the output is to boost the output power [8].

In 2006, Huber *et al.* introduced the Fourier domain mode-locked (FDML) as a new technique for fast performance swept lasers in OCT applications with high output power and low ASE background [9]. The schematic diagram of the FDML frequency swept laser is presented in figure 4.6.

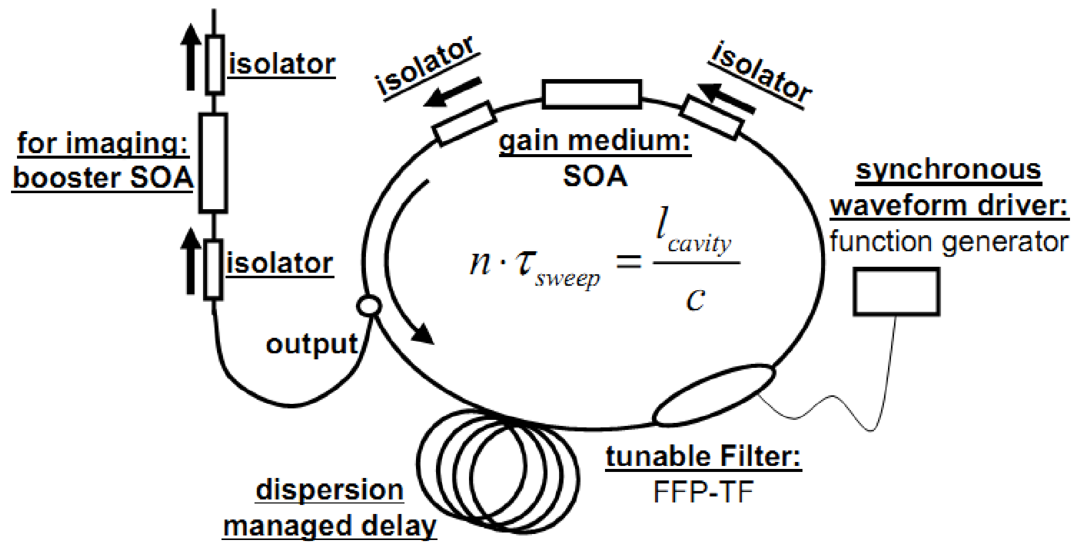

Figure 4.6: Schematic diagram of the FDML frequency-swept laser [9].

In the FDML setup, which is implemented in a "cavity tuning" configuration, a delay line is integrated into the laser cavity. A quasi stationary mode is produced in the cavity by tuning the optical filter at (or a harmonic of) the cavity roundtrip time. In other words the optical filter is synchronized to the cavity roundtrip time. In this technique lasing does not have to be built up from spontaneous emission; which increases the sweep rate of the system tremendously. In order for the round trip time to be equal to the tuning speed of the filter, several km of fibre are required in the delay section. Due to the additional loss, the peak power is lower than for the corresponding short cavity laser. By this method, a tuning range of 63nm at 236kHz with 7mW average output power, and applied to human retina imaging was achieved [10]; while the short cavity equivalent could only demonstrate a sweep rate of 20kHz in tuning range of ~120nm and peak power of 45mW [8].

Beside all these promising features there are some difficulties with FDML operation including the high loss of nearly 3dB per kilometre in the optical fiber, large chromatic dispersion, and expensive optical fibers at specific frequencies (i.e. not SMF-28 or similar) for 800nm or 1060nm wavelength range. This setup will be very expensive in case of using polarization maintaining fibers. Otherwise polarization maintaining would be required all the time. Moreover, the size of this setup is fairly large relative to the other swept laser configurations due to fibre spool.

To overcome these problems, wavelength swept ASE sources have been introduced [11]. By passing the ASE light through multiple different gain and filter elements, sufficient output power and sensitivity is obtained without any need for lasing in an optical cavity. The schematic of the setup is plotted in figure 4.7.

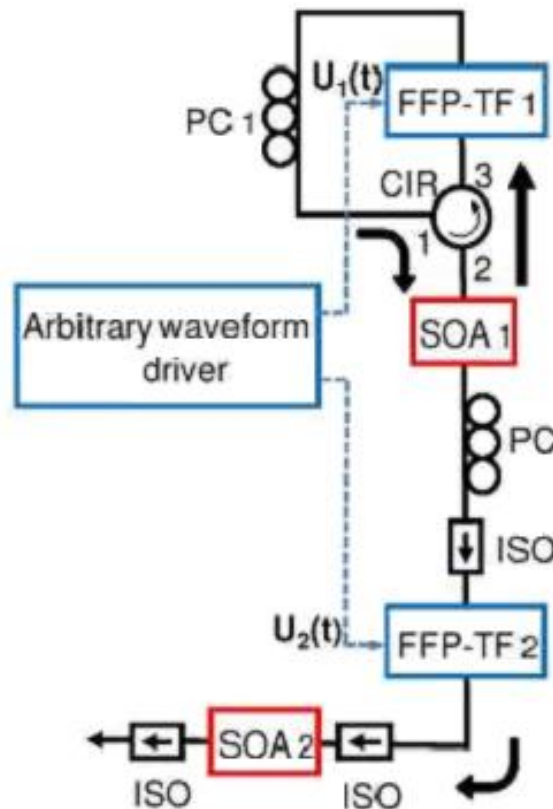

Figure 4.7: Wavelength swept ASE source. The propagation direction of the light is indicated by arrows [11].

In this setup ASE from the first SOA propagates through an optical circulator and is filtered by a tunable Fabry-Perot filter. Directing back to the same SOA and getting amplified, the spectrum is filtered once again with another filter to ensure that the ASE background is removed before the second SOA boosts the light. The arbitrary waveform driver needs to provide two equal frequent waveforms with adjustable phase shifts for the filters.

With this configuration at center wavelength of 1300nm sweep rates of 10kHz, 100kHz and 340kHz over 100nm full width sweep range with average power of 50mW were demonstrated. The linewidth of this system is not as good as a laser, and so roll-off in sensitivity with depth, causing limited imaging depth, is a problem.

As previously discussed, wider range of wavelengths are desirable for OCT applications. Covering the spectral range between 1.1 to 1.3µm is of specific interest for biomedical imaging applications due to low scattering and absorption.

In 2010 in a static tunable laser configuration, tuning ranges of more than 200nm in the range of 1122nm – 1324nm have been obtained using QD based SOAs by Rafailov *et al.* [12]. In a quasi-Littrow configuration by driving the QD-SOA to very high current densities (8.5kA/cm^2), they reached average output power of 400mW for a tuning range of 110nm. Adding an output coupler to the configuration extended the tuning range with 202nm being demonstrated. This highlighted the possible benefits of using QD based SOAs for obtaining a broad spectral band-width SSL.

4.3 Previous work

Krstajić *et.al.* implemented the first swept source and OCT system utilising QD-SOAs, shown in figure 4.8 (a) and (b) respectively [1]. The swept source has been set up in a short cavity Littmann configuration. A commercial QD-SOA (Innolume Gmbh) is used as the gain medium. Fast lasing build up within the cavity is expected for QD-SOAs due to the fast carrier dynamics in QDs [13].

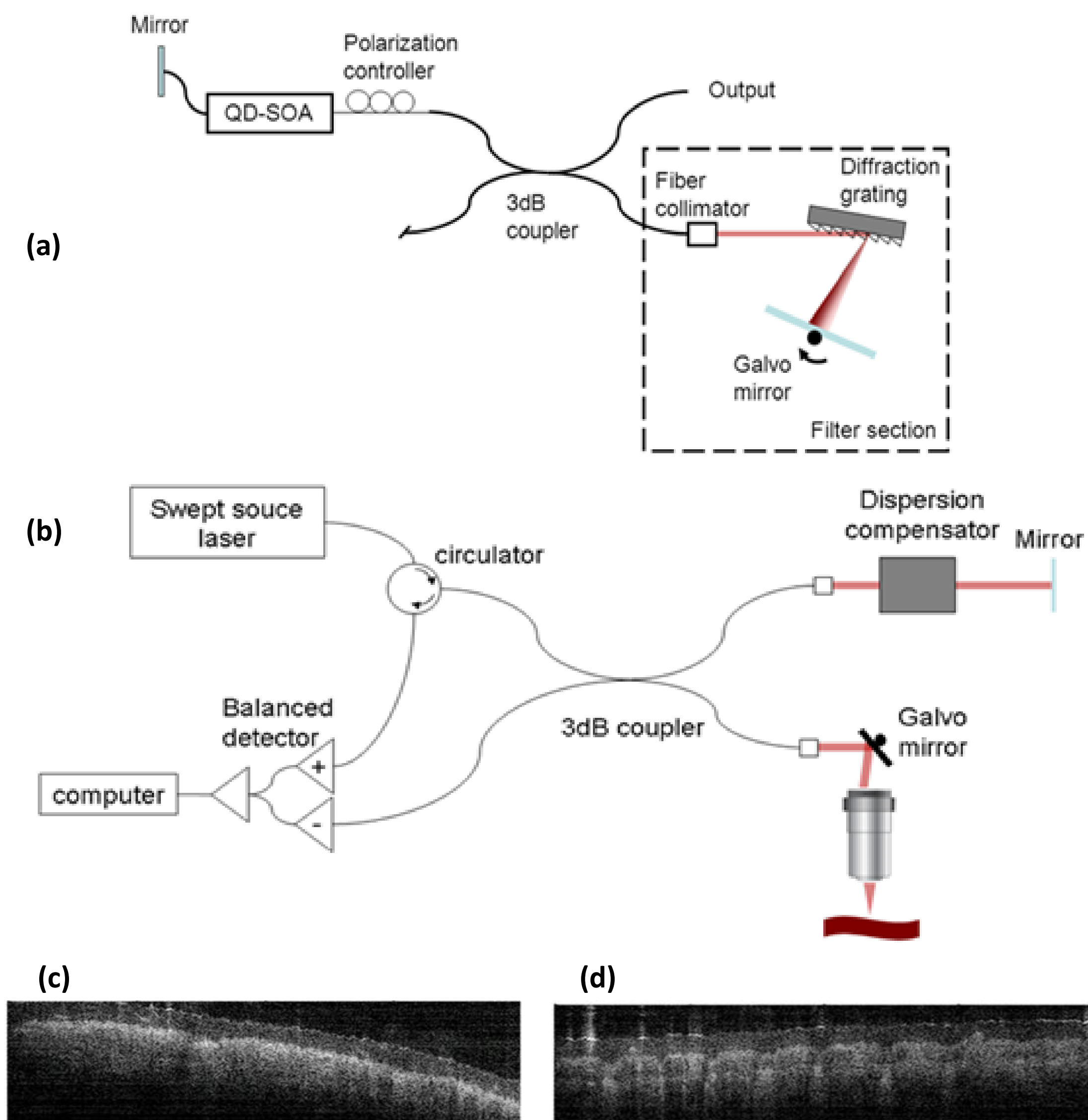

Figure 4.8: a) Schematic of short cavity Littmann configuration swept source setup; b) SS OCT system used for imaging evaluation; c) Finger palmar skin image taken by the SS-OCT system; d) Palmar knuckle joint image (Both figures are approximately 5mm wide and 2mm deep) from [1].

In this setup the lasing wavelength of the SSL is tuned by a galvanometer mirror and diffraction grating. By applying a triangular voltage waveform to the mirror, the angle of the mirror in respect to the grating changes, resulting in different wavelengths being fed back to the cavity. The linewidth of this filter is proportional to 1/(the number of lines illuminated) based on the standard grating equation. This implies that to have a narrow filter one should illuminate a light beam which covers more lines on a large grating with high number of lines per millimetre. The larger the grating the slower the movement is, therefore, it is difficult to have a fast narrow linewidth swept laser in this way.

The polarization controller is used to ensure maximal output power by matching the polarisation of light emitted from the fibre to the required input orientation of the SOA, since the QDs are highly strained and therefore only have TE gain. The 3dB coupler connects the QD-SOA to the filter section and acts as the cavity output coupler.

The filter consists of an 830 grooves per millimetre diffraction grating and scanning galvanometer mirror. A gold plated single mode fiber is used at the other side of the SOA to act as the cavity end mirror and reflect back the light into the amplifier.

Sweep bandwidth of 94nm with 16mW peak power was achieved with this configuration. In order to show the practical application of the QD swept, laser, skin-tissue images are shown in figures 4.8 (c) and (d).

4.4 Gaps in knowledge

As previously discussed, QD based SOAs with inhomogeneously broadened bandwidth comparable to commercial QW devices have shown promising results as active elements in broadband light sources. Since the application of QD technology to swept

light sources, is new, there is plenty of scope to enhance the characteristics of the light source. Initially, multiple QD-SOAs can be incorporated in one SLS configuration in order to achieve broader bandwidth. Overlapping spectra of SOAs with different center wavelength is a possibility to obtain a broader spectrum from a SLS. QW and QD materials can be engineered to cover specific range of wavelength. Further to this, to further increase the bandwidth the design of the light source can be optimised. Finally, the material being used in the active element can be optimised for this application since most QD developments has been towards narrowing the bandwidth in order to improve laser performance.

One of the main disadvantages to the QD technology is the low areal density (relative to a QW) and also since these are designed for broadband operation, the peak gain is lower than for narrowband SOA counterparts. In order to compensate for this, the device length needs to be extended. However, once the chip length exceeds about 5mm, standard packaging becomes difficult. As such, a simple way to mitigate for this low peak gain is to use two butterfly SOA modules to double the gain. These can be used in two configurations, two identical devices in series to increase peak gain, or two devices with shifted central wavelength to broaden the gain. In the first case, since the gain is approximately parabolic, increasing the peak also increases the bandwidth. In the latter, complementary SOAs obviously increase spectral bandwidth coverage for the same peak gain. I shall discuss the merits and results of both of these approaches in the following section.

4.5 Experimental results

4.5.1 Comparison of QD-SOA and QW-SOA

Two different SOAs have been used, one manufactured from GaAs based self-organised quantum dots and the other manufactured from InP based quantum wells. The ASE of the QW-SOA (BOA-1130, COVEGA) is shown in figure 4.9 (a) at 20°C. It shows a peak at 1350nm under low current injection, and with state-filling as the current is increased, the emission broadens to span 1250-1350nm. The QD-SOA (part number 1200-70-PM-20dBm, Innolume Gmbh, Dortmund, Germany) shows a slightly more complicated emission spectrum. Amplified spontaneous emission of QD-SOA is shown in figure 4.9 (c) for various drive current levels at the same temperature. The QD active element is made up of three different types of QD layers emitting at 1270 nm (x4), 1243 nm (x3) and 1210nm (x3). In addition to peaks from the ground-states of these QD ensembles, state filling effects result in saturation of the ground-state, and emission from the QD excited states.

Figure 4.9(b) shows the intensity of the QW-SOA at two different wavelengths of 1250nm and 1350nm and figure 4.9(d) shows QD-SOA intensity at two different wavelengths of 1200 and 1300nm. In QD-SOA the intensity drops drastically for wavelengths longer than 1300nm which can be compensated by adding the intensity of another amplifier (for example, the QW-SOA) with high intensity at long wavelengths.

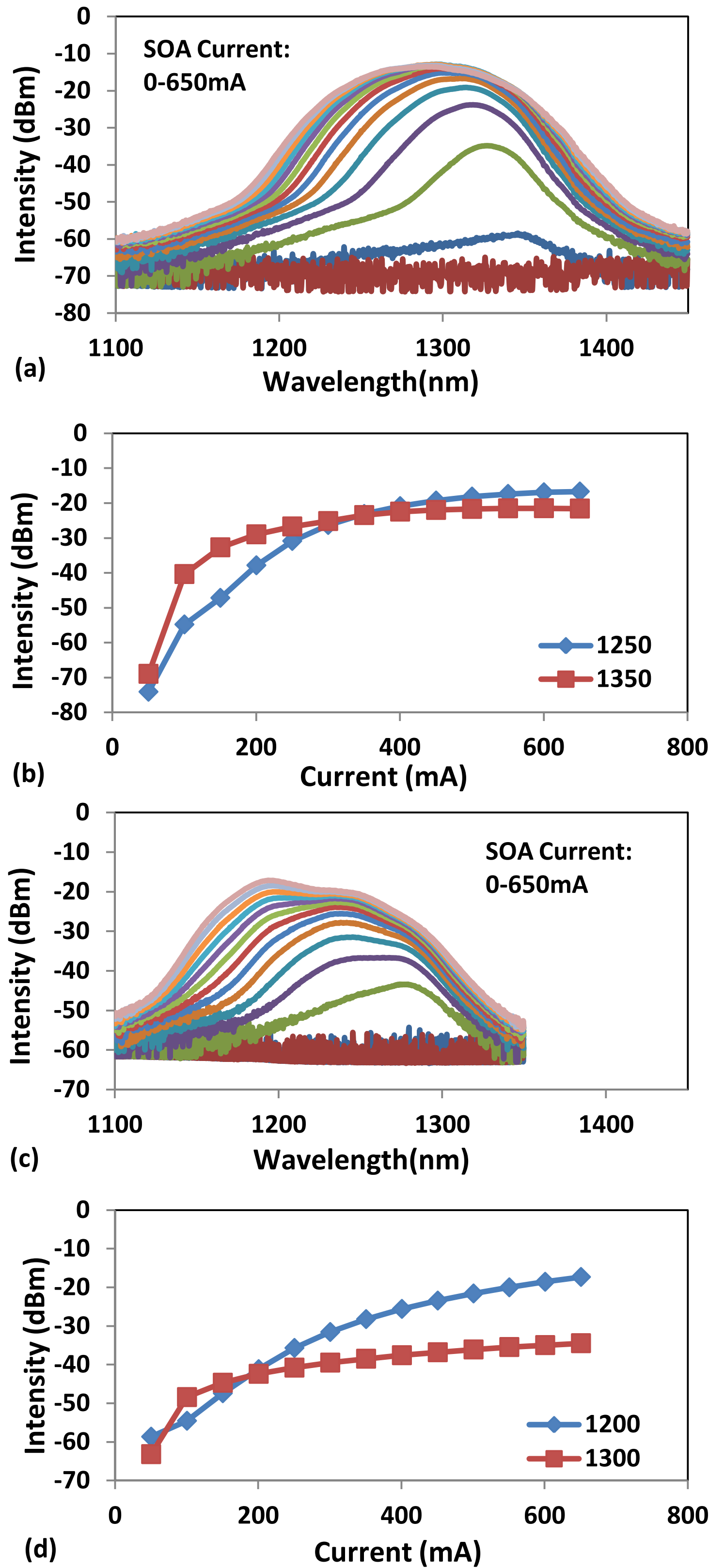

Figure 4.9: (a) Amplified spontaneous emission of InP based QW-SOA (b) QW-SOA intensity at 1250nm and 1350nm(c) Amplified spontaneous emission of GaAs based QD-SOA and, (d) QD-SOA intensity at 1200nm and 1300nm.

4.5.2 QD-SOA characterization

Characterization of the QD-SOA was carried out using the arrangement shown in figure 4.10(a). The swept laser source for the characterisation is setup similar to that shown in figure 4.8(a). For uniformity, a variable attenuator is used to keep the input power of the test SOA fixed. The 50:50 splitter makes it possible to measure the input and output power of SOA simultaneously.

The single-pass gain was calculated by dividing the output power of the SOA at the probe wavelength, by its input power. Figure 4.10(b) plots the gain as a function of wavelength. The output power dependency of the gain for different wavelengths is shown in figure 4.10(c). The 3dB saturation output power can be calculated from this data.

A value for the saturation power of the QD-SOA is 3-4mW, which is around an order of magnitude lower than that of the QW-SOA (refer to the specification sheet in appendix II). A key advantage for QD-SOAs is reported to be high saturation power [13]. However, in order to achieve these benefits, further optimisation of this particular QD-SOA device design is required. An increase in areal dot density, and number of layers stacked within the active element will increase the gain coefficient, and an increase in chip length will increase the single-pass gain. However, increasing chip length may result in challenges in terms of self-heating or parasitic lasing of the SOA.

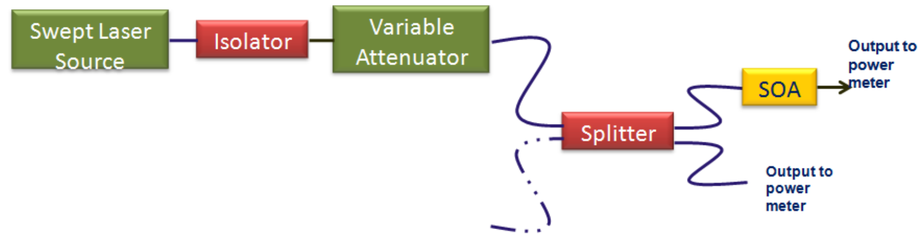

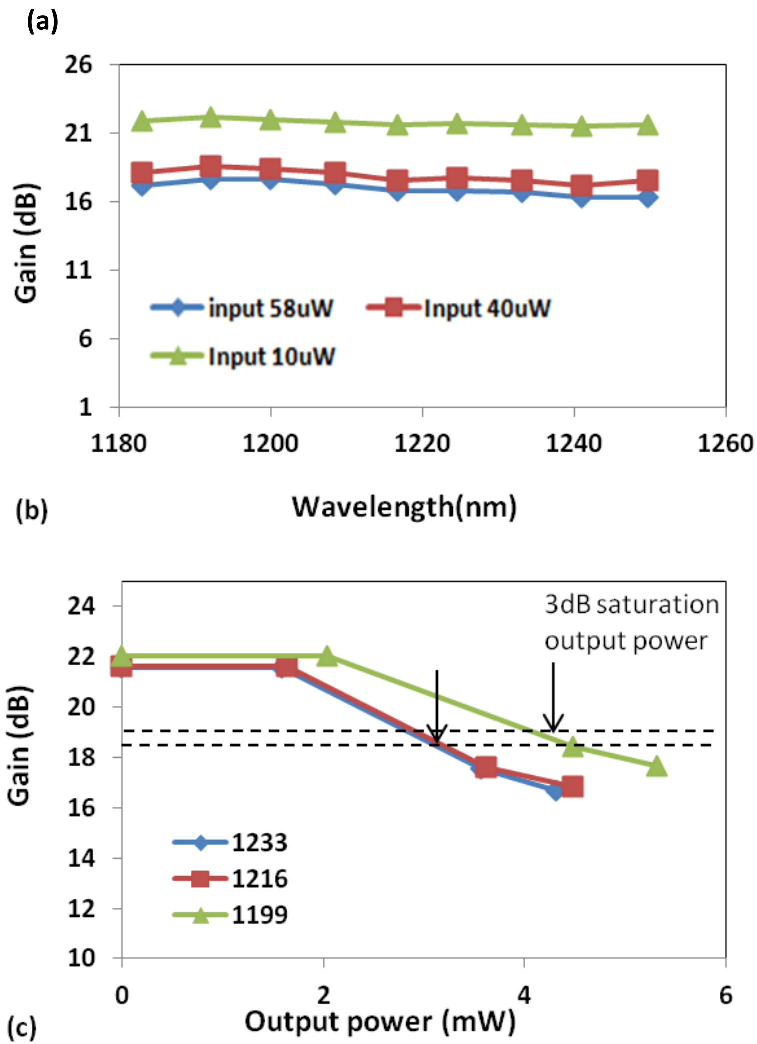

Figure 4.10: Characterization of QD-SOA. (a) Characterization setup, (b) Gain vs. wavelength of SOA, (c) Gain vs. output power for constant wavelength

4.5.3 QW-SOA characterization

The ASE power as a function of current for the QW-SOA is plotted in figure 4.11. The intensity increases by increasing the current and tends to saturate for currents higher than ~600mA. This parameter was measured by the power meter, directly after the SOA.

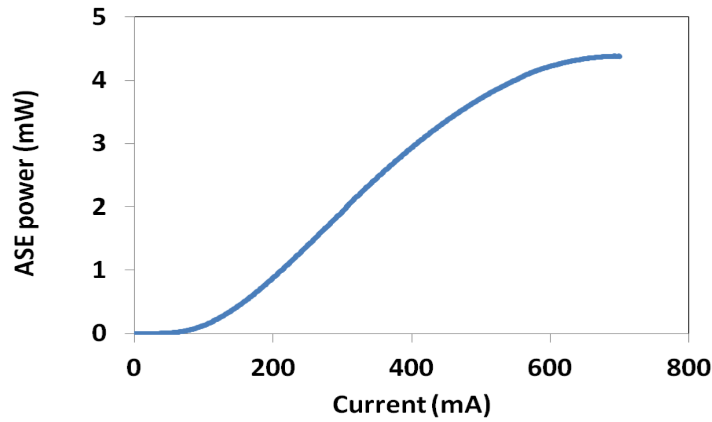

Figure 4.11: ASE power of the QW-SOA

The same swept source laser can be utilised to characterize the QW-SOA. The net gain spectra measured for this SOA is plotted in figure 4.12 (a) and (b) for various applied current. By increasing the current the gain increases and the peak gain shifts toward shorter wavelengths until it becomes saturated above 500mA. For the QW device, as expected, a parabolic gain is a good approximation, as shown by the black curves.

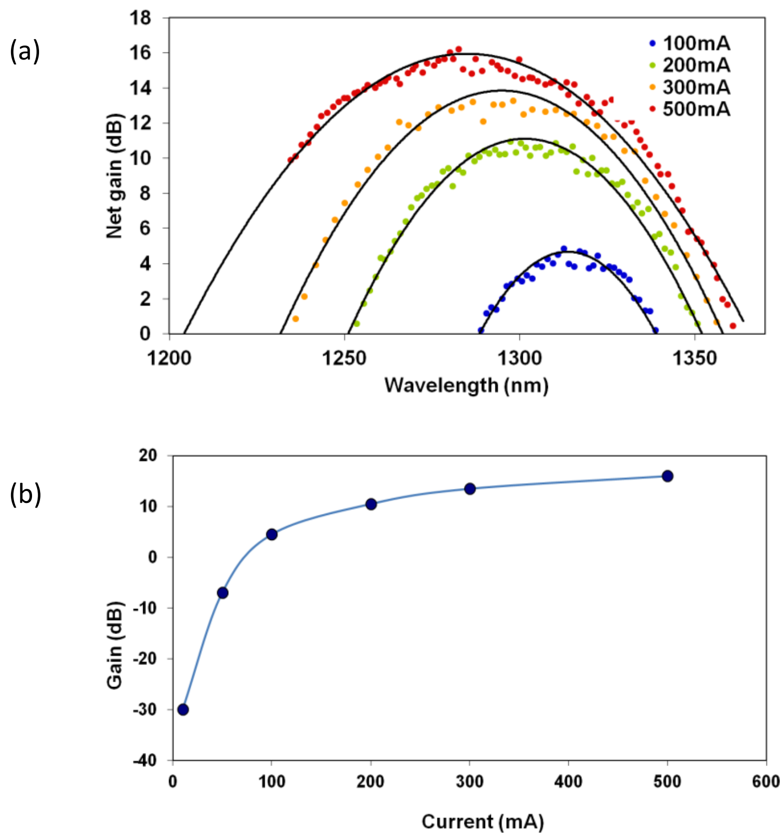

Figure 4.12: Net gain of QW-SOA, measured through the swept source laser (a) spectra, (b) peak gain as a function of current.

4.5.4 Identical QD-SOAs

As discussed previously, increased single-pass gain is advantageous for the SLS in terms of tuning rage and output power. As a consequence, the benefits of using two identical QD-SOAs in the SSL have been explored. These two QD-SOAs (part number-1200-70-PM-20dBm, Innolume Gmbh, Dortmund, Germany) are used in a ring cavity as shown in figure 4.13.

The isolator used in this configuration is io-j-1250 with the reverse transmission response plotted in figure 4.14. This isolator compared to the other available options had better performance in terms of isolation (>20dB) in the required wavelength range (1175-1275nm). The 'standard' narrowband 1310nm isolator (io-h-1310) is a telecoms component and is designed for maximum isolation. The broadband component io-j-1250 is designed for moderate isolation over a wider wavelength range and is also centred closer to the QD emission wavelength.

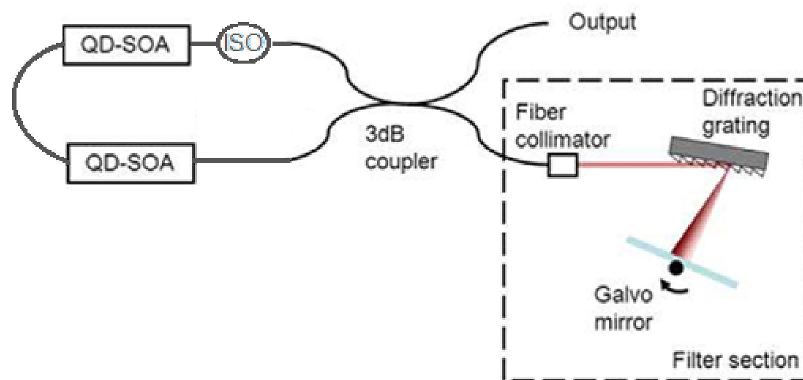

Figure 4.13: Schematic of swept source setup with two QD-SOAs.

To check whether intra-cavity reflections from the splitter may be an issue, the back reflection of the 3dB splitter used in this configuration is measured and plotted in figure

4.15. The reflection is found to be better than 45dB, which is greater than the combined gain of both SOAs, so is acceptable.

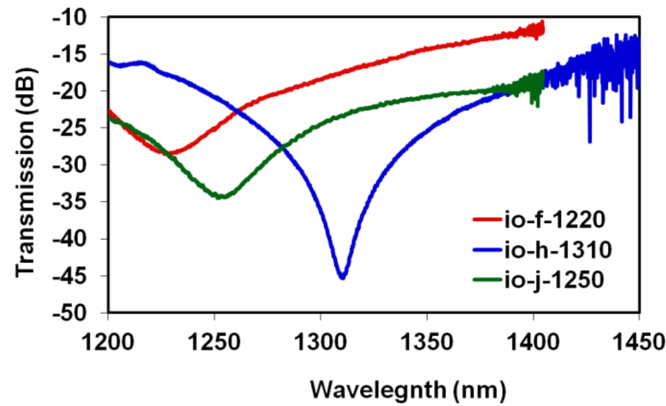

Figure 4.14: Reverse transmission response of available isolators

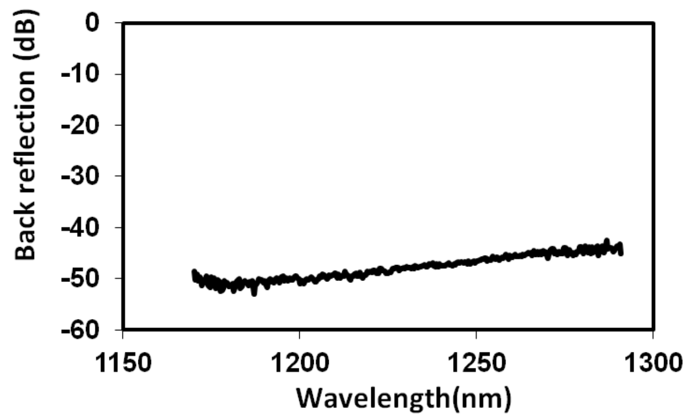

Figure 4.15: Back reflection of 3dB splitter

Figure 4.16 shows the range of lasing spectra obtained for this configuration. In this setup the output is observed with an optical spectrum analyzer (HP 70951B). The 3dB coupler and the filter section are identical to ones used for setup in figure 4.8. A 94nm bandwidth and output power of 17mW was obtained. This compares favourably to using a single QD-SOA in the ring cavity (77nm, 7mW), highlighting the benefits of additional gain within the cavity in order to overcome the insertion losses of the fibre components.

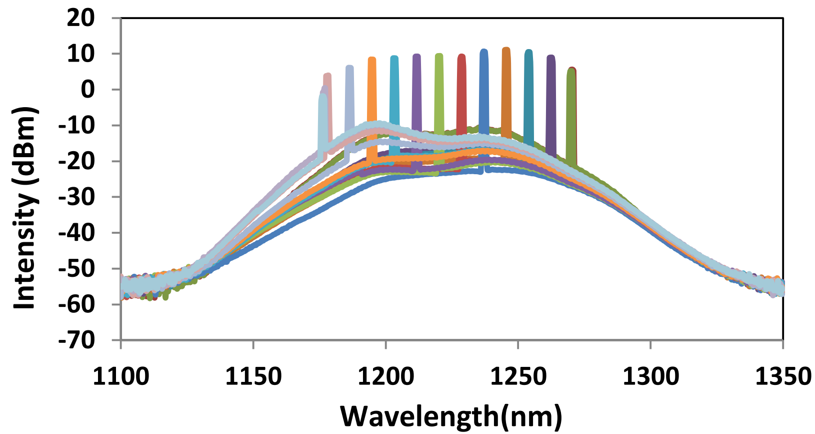

Figure 4.16: Laser sweep detected by the optical analyser

The bandwidth here is limited by the current rating of the amplifier (0.7A), in comparison with previous results of 200nm being possible at currents beyond the maximum operating conditions of the device (1.7A) [12]. Using higher current drive currents should allow the lasing band to be extended to shorter wavelengths. On the other hand, increasing the current may lead to appearance of the parasitic lasing since the peak gain will also increase, requiring additional isolators. Further improvements to this system would be possible by using fibres of uniform type, splicing rather than using connectors, and adding further isolators (between and after the QD-SOAs). For this last point, the neighbouring QD-SOAs inject ASE into each other which will be amplified and reduce the carrier population (and hence gain) available for the desired lasing wavelength.

Comparing these results to previous work using a single QD-SOA in a dual pass configuration with the SOAs having the same drive currents (0.7A) in both cases we find almost identical performance (94nm, 16mW). This is as expected due to the mirror symmetry of the two systems. However, the excellent performance obtained using the amplifiers in dual-pass mode opens up possibilities to combine two dissimilar SOAs in a novel configuration.

4.5.5 Complementary QD-SOA and QW-SOA

As highlighted previously, a novel approach, utilising SOAs with different spectral coverage was explored to increase the spectral tuning range of the SLS. Figure 4.17(a) shows a schematic of the SSL configuration using two very different SOA technologies, an InP based QW device in parallel with one of the GaAs based QD-SOAs used previously. The amplified spontaneous emission of two amplifiers is shown in figure 4.17(b). The centre wavelength for the ASE for the QW-SOA is at ~1300nm while that of the QD-SOA is ~1200nm. These two devices have a complementary spectral coverage with regards to extending the spectral bandwidth for the SSL. Figure 4.17(c) shows the range of lasing spectra which may be obtained for this configuration. Both SOAs were driven with 0.7A. A 154nm bandwidth is obtained with 8mW power.

Here an additional 70nm of bandwidth has been obtained in this layout in comparison with that of Krstajić *et. al.* using a single QD-SOA in dual pass mode [1]. This spectral bandwidth is predicted to approach 220nm if additional current were to be applied to the QD-SOA [12]. Such a spectral bandwidth offers ~3um axial resolution (see equation 1.1) offering a x2 increase in resolution as compared to present OCT systems.

In order to make a practical system, the output power at shorter wavelengths (from the QD-SOA) needs to match those at longer wavelengths (QW-SOA). The simple solution is to reduce current in the QW-SOA. Modulating a booster SOA is not an option in this configuration as a single booster SOA is not possible. A better solution would be to increase the gain in the QD-SOA. These have been discussed previously with regard to enhancing the saturation power for the QD-SOA. Using two QD-SOAs in series is an additional enhancement to this system. It is also noted that the QD-SOA and QW-SOAs

cannot be placed in a loop configuration since the absorption region of the QW will overlap the QD-SOA gain.

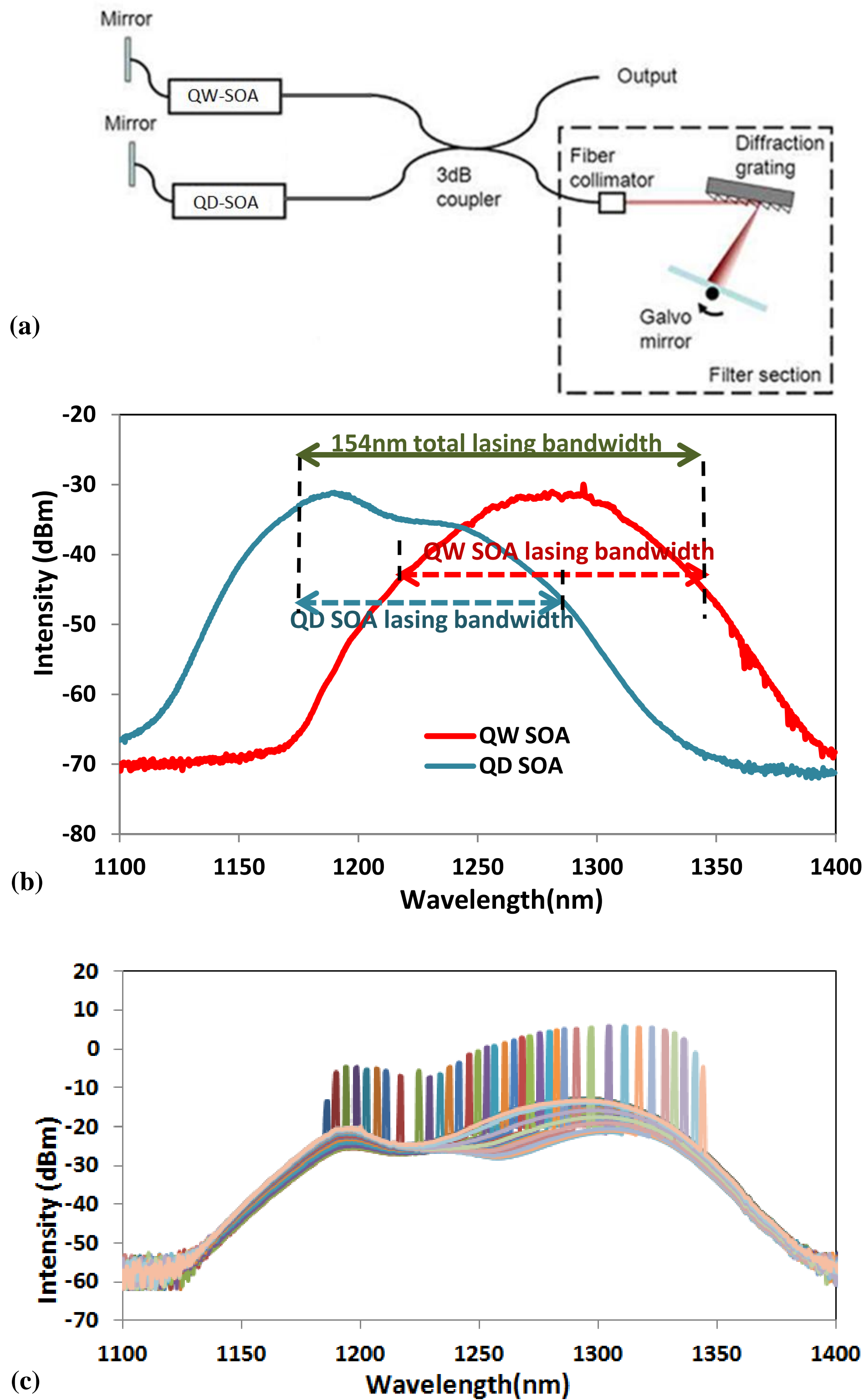

Figure 4.17: a) Schematic of swept source setup with QD-SOA and QW-SOA, (b) ASE of amplifiers, (c) Laser sweep detected by the optical analyser

4.5.6 Multiple pass ASE

Finally, a filtered ASE source using these complimentary SOAs was designed and characterized. Previously, a filtered ASE source, with coupled Fabry-Perot filters, driven with a carefully selected phase-shift has realized a rapidly swept, broad band-width light source, as discussed earlier in this chapter, was presented [10]. I have therefore developed the idea of incorporating complementary SOAs in a filtered ASE source.

4.5.6.1 Filter Characterisation

For this configuration I have utilised a tunable Fabry-Perot filter (FFP-TF2 Micron Optics). In order to characterise the filter, the ASE output was passed through the filter, and the transmitted light was measured by a high resolution OSA (Advantest Q8384, 0.01nm bandwidth). This is plotted in figure 4.18.

The FWHM of filtered ASE (and hence the filter linewidth) is measured to be 0.11nm. The linewidths is a function of the filter being used in the setup (FFP).

Due to the mechanical nature of this filter, hysteresis behaviour for forward and backward voltage sweeps will occur. This is plotted in figure 4.19 showing the difference in wavelength for forward and backward voltage sweeps. The linearity performance is excellent over at least a 150nm range.

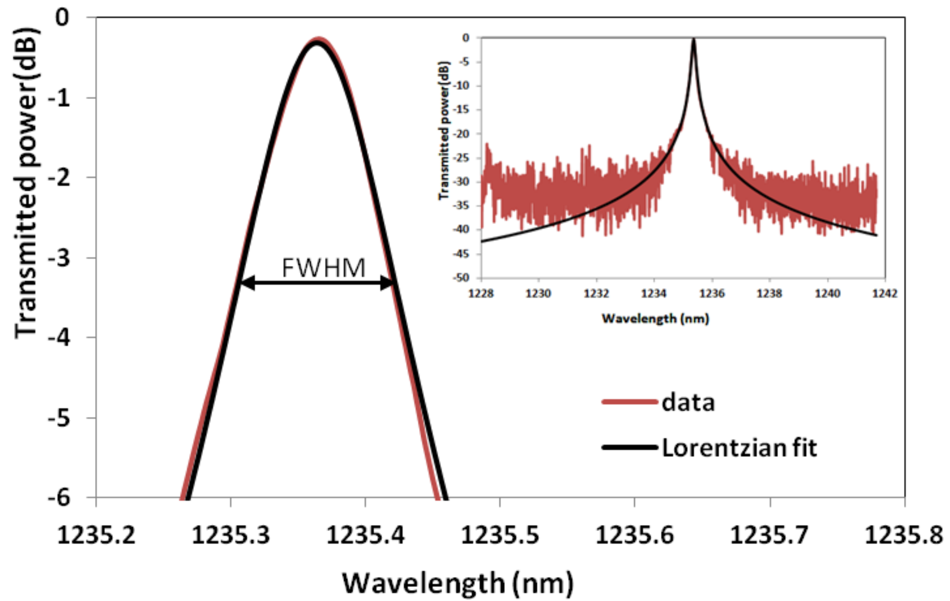

Figure 4.18: FWHM of QW-SOA lasing under 700mA driving current (red), with a Lorentzian fit (black). (OSA resolution: 0.01nm)

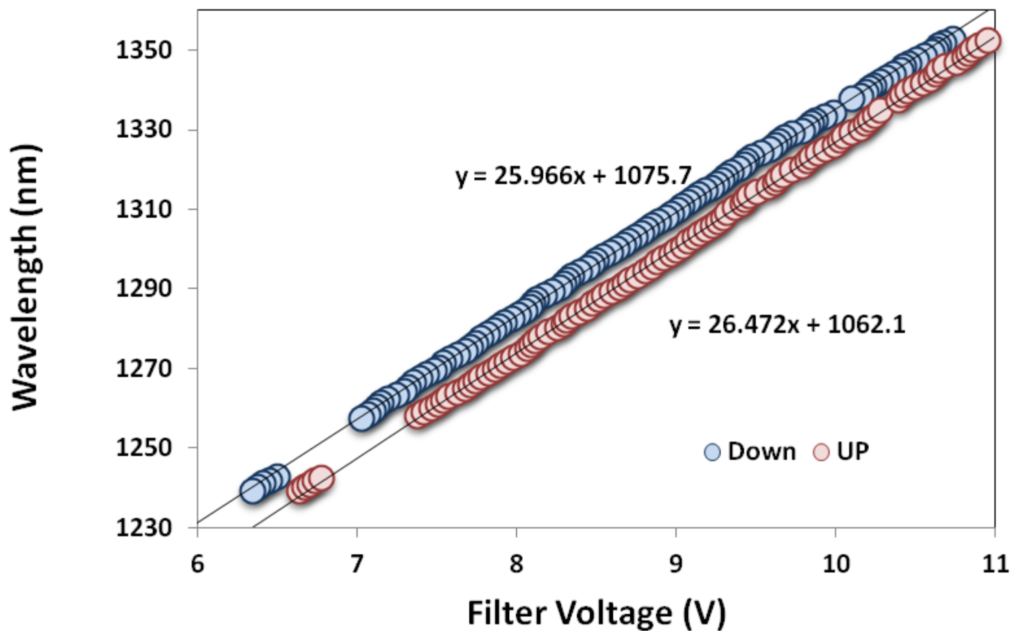

Figure 4.19: Hysteresis in FFP filter

4.5.6.2 Analysis of SSL scanning speed

Another important parameter in SSL is the speed of sweeping the laser. The speed is primarily limited by the time the laser needs to build up lasing from the ASE and is

mostly dependent on the gain of the SOA, the losses in the cavity and the finesse of the filter section being used in the setup. Intensity of the ASE, saturation power and the length of the cavity have also influences on the maximum achievable speed. The particular galvanometer mirror which has been used previously in this work gives us the maximum speed of only 100 Hz which is too low for practical OCT applications. The FFP filter provides a speed in the range of 100 kHz. The impact of cavity length, and therefore round trip time, by using different fibre lengths is investigated. Here, a high speed photo diode has been utilised in order to plot the lasing intensity as a function of sweep frequency.

For the first step the operation of a SSL utilising a QW SOA was investigated. The output intensity is plotted for various drive currents in figure 4.20. Frequencies up to 2000 Hz have been investigated. As expected, by increasing the filtering speed the intensity gradually decreases.

The cavity length for this setup is ~13m which is very long in comparison to the previous setup of Huber *et.al.*. To show the effect of cavity length on the operating speed and bandwidth, extra 7m of optical fiber was added to the cavity length and the measurements were repeated. The results are plotted in figure 4.21.

For frequencies above 1kHz the intensity decreases which defines the maximum speed limit where the output power can be preserved. The calculation of this value will be discussed later.

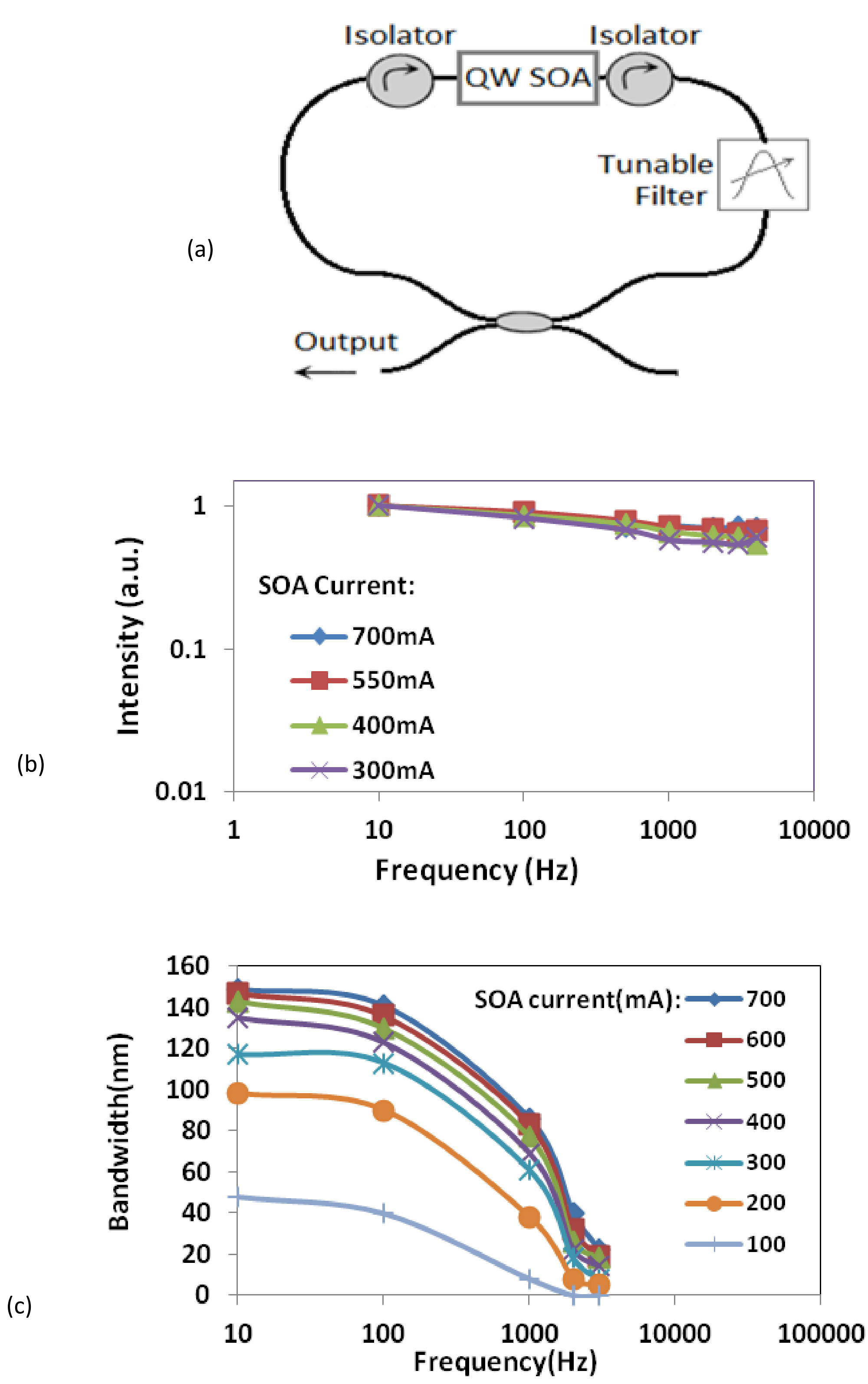

Figure 4.20: (a) QW SOA with FFP filter in a cavity setup with 13m length, (b) maximum intensity of the output as function of frequency and (c) bandwidth as a function of frequency.

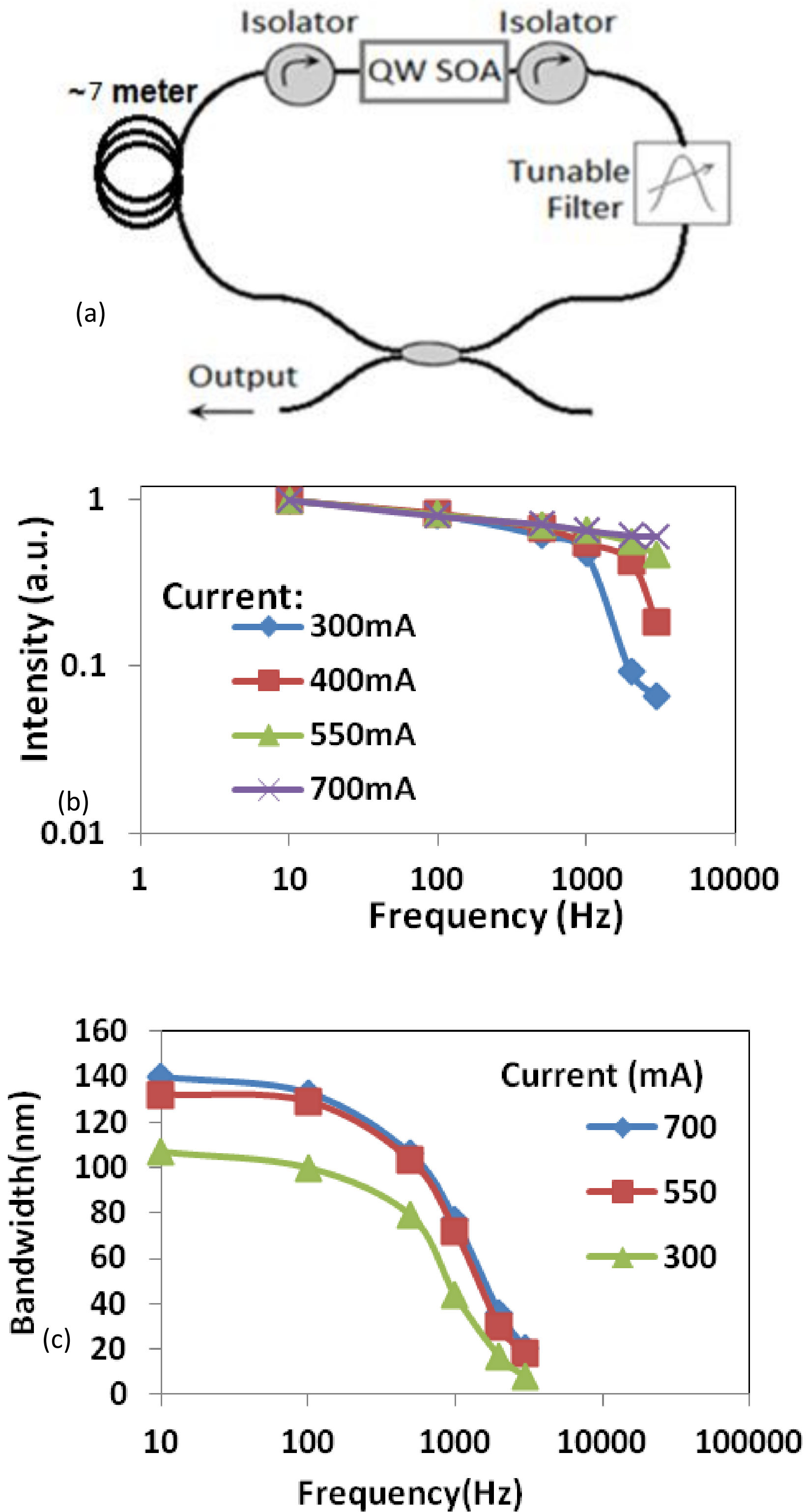

Figure 4.21: (a) QW SOA with FFP filter in a cavity setup with 20m length, (b) maximum intensity of the output as function of frequency and (c) sweep bandwidth as a function of frequency.

The intensity profile of the output power for forward (from short to longer wavelengths) and backward (long to short wavelengths) sweeps were measured with a photodiode and the data plotted in figure 4.22 for cavity lengths of 13 and 20m for a filter speed rate of 10Hz (repetition rate) and SOA drive current of 700mA.

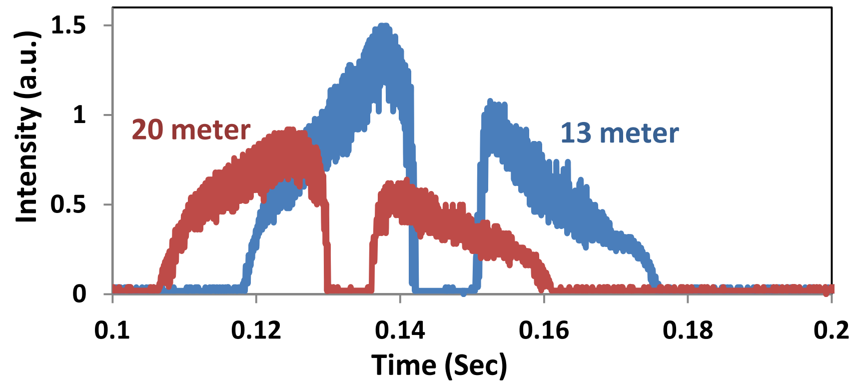

Figure4.22: Temporal intensity profile for different cavity lengths (forward sweep with slightly higher peaks and backward sweep with slightly lower peaks).

At this speed, the setup is working bellow the saturation limit of the laser. There are enough round trips of the cavity within the filter bandwidth for lasing to be built up from ASE. It can be observed that both forward and backward sweeps are clearly resolved.

For higher frequencies the profile of the output signal changes as plotted in figure 4.23 for cavity length of 20m at 2000Hz. At this speed, there are still multiple roundtrips of amplification of the spontaneous emission, however, the movement of the filter to a different wavelength is too quick to let the power build up to reach full saturation. In addition, a significant asymmetry in the two scan directions is observed which is attributed to four-wave mixing effect in the nonlinear laser gain medium leading to a downshift in energy or frequency [8].

For sweep frequencies even higher, the ASE does not have enough time to make multiple roundtrips and the output will be the filtered single pass ASE.

Correspondingly, the output intensity is very low. However, an advantage is that in this type of the setup high speed sweeping rate can be achieved and since there is no feedback, the nonlinearity of the gain medium will have no influence on the output intensity profile. The low power can be mitigated by amplification with an output SOA (booster) after the filter.

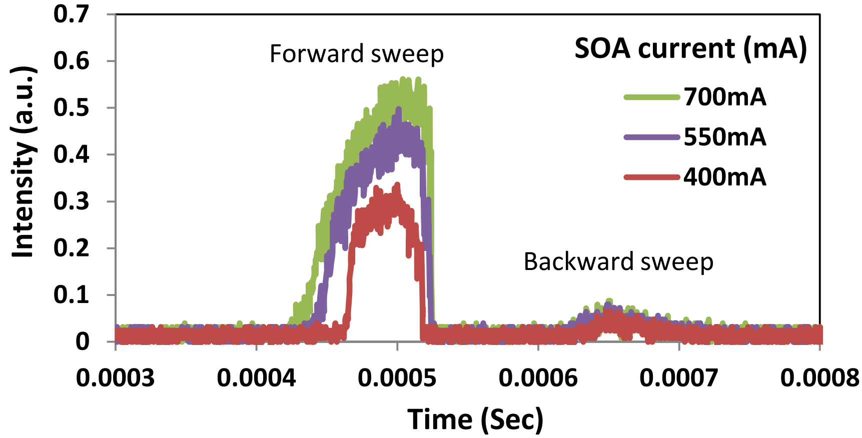

Figure 4.23: Temporal intensity profile for different SOA drive currents at 2000Hz.

The maximum sweep frequency f_{sweep} for lasing build up to saturation can be estimated as [9]:

$$f_{sweep} \approx \frac{\log(G.\rho).\Delta\lambda.\eta.c}{\log\left(\frac{P_{sat}.\Delta\lambda_{tuningrange}}{\Delta\lambda.P_{ASEtotal}}\right).L.n_{ref}.\Delta\lambda_{tuning\ range}} \quad (4.1)$$

Where G is the small signal gain of the laser medium and ρ is the fraction of energy fed back after one roundtrip and is a function of the round-trip losses and the output coupling. $\Delta\lambda_{tuningrange}$ is approximately the total bandwidth of the ASE and $\eta = 1/\pi$. P_{sat} is the saturation power and $P_{ASE,total}$ is the total spectrally integrated ASE power. Finally $\Delta\lambda$ is the filter width. For the presented setup these values are:

$G \approx 30$dB (1000)

$\rho \approx 0.2$ (<1.5dB filter insertion loss, <0.5dB isolators loss, 50% output coupler)

$\Delta\lambda = 0.135$nm

$c \approx 3e8$ m/Sec

$P_{sat} = 30mW$

$\Delta\lambda_{tuningrange} = 169nm$

$P_{ASE,total} = 3mW$

These values give us f_{sweep} equal to 2.25 kHz for cavity length of 13meters. In comparison with previous work from Huber *et. al.* [9] with (2.4m fiber length) it is nearly five times smaller. This frequency determines the maximum speed of sweep which the ASE has enough time to build up to the full steady state lasing power. For the setup investigated here, this value is in good agreement with experimental results as shown in figure 4.20(c) (2.25 kHz for L=20m) and 4.21(c) (1.46 kHz for L=13m).

4.5.6.3 Configuration of QD & QW swept laser

Figure 4.24(a) shows a schematic of a swept source where the QD-SOA and QW-SOA are in connected in parallel, before the FFP tunable filter. The filter is controlled by a swept source controller (Micron Optics SSC 225). This setup is considerably simpler to implement due to the all fibre design, but is expected to achieve much lower powers, than the previous work of Huber *et al.*[9], because of extra 3dB couplers and longer fiber length. Due to the considerably lower moving mass, the fibre tunable filter should enable much faster sweeping speeds (>100kHz) in comparison to a galvo mirror filter (10kHz). Its Lorentzian pass-band filters the amplified spontaneous emission and gives a wide wavelength span.

Figure 4.24(b) plots the emission sweep for the filtered ASE source. The bandwidth obtained from this configuration is 225nm centered at 1253nm, with an instantaneous linewidth of 0.11nm. However, multiple peaks are observed, due to the FSR of the filter being only 165nm.

Solutions which may be applied in future, to obtain higher power levels include using nominally identical SOAs in series, and increasing the driving currents of the SOAs. In addition, an FFP with wider FSR or utilising correlated (phase shifted) drive voltages applied to two FFPs, geometry similar to that of Huber *et al.* [10], may also allow ultra-broadband, high speed sources to be realised. In this setup there is additional loss due to the use of 3dB couplers that limits the operation of the setup for low gain SOAs. The operating sweep rate for this configuration was chosen to allowing the multiple pass ASE build-up in the cavity. For high sweep rates only single pass ASE can be achieved. Again, this type of filtered ASE configuration gives low output power which can be amplified with a booster at the output.

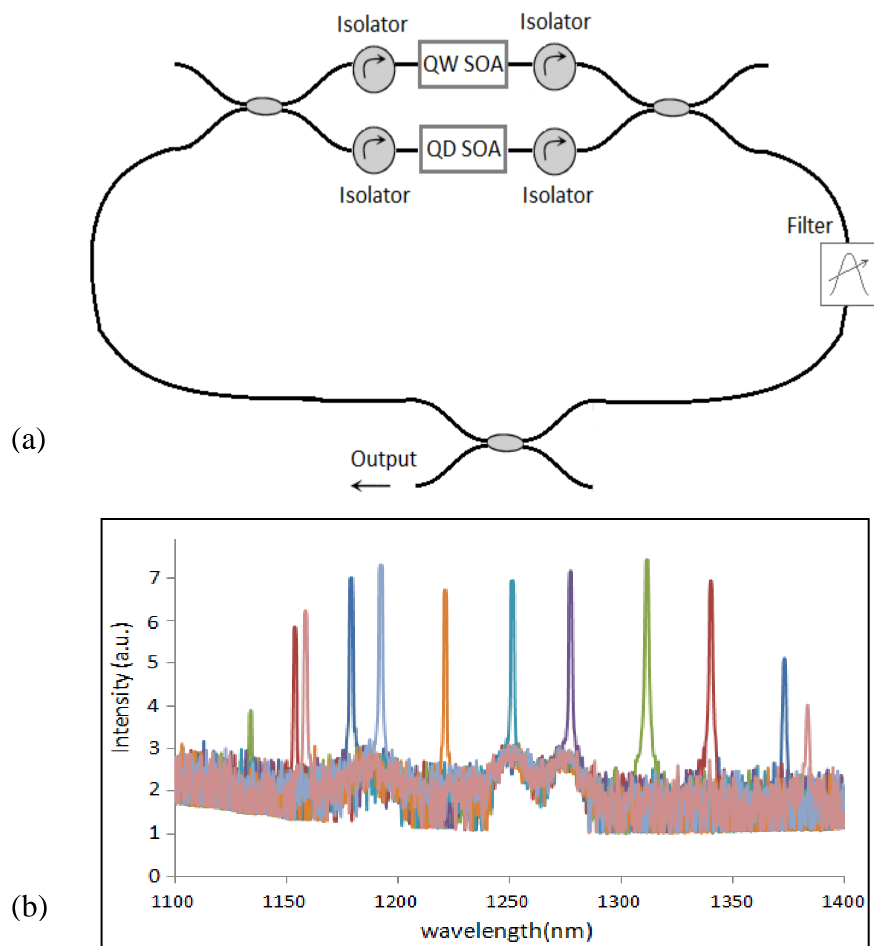

Figure 4.24: a) Schematic of swept source setup with QD-SOA and QW-SOA and the FFP, b) Laser sweep detected by the optical analyzer.

4.6 Summary

The characterisation of QD-SOAs has been reported. A comparatively low gain and saturation power has been measured, and routes to improve these characteristics have been discussed. A dual QD-SOA, ring cavity SSL has been realised with 94nm spectral bandwidth and 17mW of output power. The similarity in performance between this system and a dual pass SSL opens up the route to explore using complimentary SOAs in an SSL and Filtered ASE.

For the complimentary SOA SSL, a spectral coverage of 154nm is obtained which may be increased to ~220nm by increasing the current to the SOA (beyond the recommended rating). For the filtered ASE source a spectral coverage of 225nm is obtained, but with very low powers. Routes to improve these structures have been discussed.

4.7 Future work

In order to improve the functionality of the SLS, high gain QD-SOAs can be incorporated in the setup. To have higher gain and power QD-SOAs need to be designed with greater length. Moreover, as work worldwide continues each year, epitaxial development provides higher quantum dot areal density and more QD layers in the active area. These growth improvements can immediately be translated into improved SOA performance and therefore improves swept source improvements.

To make the hybrid QW/QD configuration more efficient (packaging and coupling loss), selective area epitaxy can be used in order to design and grow QW/QD active areas on one wafer. Further still, hybrid QW/QD devices where layers can be stacked,

as discussed in chapter 3, can be utilized in SOA fabrication leading to broader bandwidth.

For all the swept lasers, the output of the sweep laser can be amplified with a booster SOA in order to increase the power. This will be helpful for high speed filtering. However it comes with a disadvantage of a larger ASE background unless the booster SOA is optimised for these applications.

For skin imaging application low depth penetration is required, therefore, a long coherence length (through narrow bandwidth) can be sacrificed for speed. For this reason, optimisation of the FFP filter bandwidth to get speed versus depth roll-off is needed.

To minimise the round trip loss in the ring cavity, instead of using connectorised fibres with long patch cords (1m is standard on each end of every component) fusion splicing of the components can be utilized.

Following this, we can look towards photonic integration of components into a chip size solution. This can be achieved by implementing all semiconductor filters such as ring resonators in adjacent with the active element, reducing the cavity length to micrometer range. Higher speeds will be achieved without improvement of any individual component.

References

[1] N. Krstajić, D.T.D. Childs, S.J. Matcher, D. Livshits, A. Shkolnik, I. Krestnikov, R. A. Hogg, “Swept-source laser based on quantum dot semiconductor optical amplifier - applications in optical coherence tomography,” Photon. Tech. lett. 23, 739 (2010).

[2] Joseph M. Schmitt, “Optical Coherence Tomography (OCT): A Review,” IEEE J. Sel. Top. Quant. Elec. 5, 1205 (1999).

[3] M. A. Choma, M. V. Sarunic, C. H. Yang, and J. A. Izatt, “Sensitivity advantage of swept source and Fourier domain optical coherence tomography,” Opt. Express 11, 2183 (2003).

[4] B. R. Biedermann, W. Wieser, C. M. Eigenwillig, T. Klein, and R. Huber, “Dispersion, coherence and noise of Fourier domain mode locked lasers,” Opt. Express 17, 9947–9961 (2009).

[5] M.J. Coupland, K.G. Hambleton and C. Hilsum, “Measurement of amplification in a GaAs injection laser” Phys. Lett., 7, 231 (1963).

[6] Rashid, A.M., Murison, R., Haynes, J. , Henshall, G.D. , Stockton, T.E. and Janssen, A., “High reliability low-threshold InGaAsP ridge waveguide lasers emitting at 1.3 µm”, J. of ,6 , 25 (1988).

[7] A. Rostami, H. Baghban and R. Maram, 2011, “Nanostructure semiconductor optical amplifiers, building blocks for all optical processing,” Springer, pp. 19-20.

[8] R. Huber, M. Wojtkowski, K. Taira, and J. G. Fujimoto, “Amplified, frequency swept lasers for frequency domain reflectometry and OCT imaging: design and scaling principles,” Opt. Exp. 13, 3513 (2005).

[9] R. Huber, M. Wojtkowski, and J. G. Fujimoto, “Fourier Domain Mode Locking (FDML): A new laser operating regime and applications for optical coherence tomography,” Opt. Exp. 14, 3225 (2006).

[10] R. Huber, D. C. Adler,V. J. Srinivasan and J. G. Fujimoto, “Fourier domain mode locking at 1050 nm for ultra-high-speed optical coherence tomography of the human retina at 236,000 axial scans per second,” Opt. Lett. 32, 2049 (2007).

[11] Ch. M. Eigenwillig, B. R. Biedermann, W. Wieser and R. Huber, “wavelength swept amplified spontaneous emission source,” Opt. Exp. 17, 18794 (2009).

[12] K. A. Fedorova, M.A. Cataluna,I. Krestnikov, D. Livshits and E. U. Rafailov, “Broadly tunable high-power InAs/GaAs quantum-dot external cavity diode lasers,” Opt. Exp. 18, 19438 (2010).

[13] T. Akiyama, M. Sugawara, and Y. Arakawa, “Quantum-Dot Semiconductor Optical Amplifiers,” Proc. of IEEE, 95, 9 (2007).

Chapter 5: Conclusions and Future Work

In this chapter a brief conclusion from each experimental chapter is provided and future work is proposed to expand understanding of the results, and enhance the performance of the relevant optical devices. The main aim of the thesis was to explore broadband optical devices based on QD and QW materials in terms of their performance in different configurations. QD devices are currently being commercialised and their applications in telecommunication and medical fields have been confirmed. However, there is a continuing need to explore the physics of the devices in terms of optimizing their performance for specific purposes.

The dominance of the role of carrier distribution and/or free carrier effects in semiconductor QDs are explored in chapter 2. Simulation results which include the effect of free-carrier induced shift and broadening on the gain and spontaneous emission spectra (and hence carrier distribution function) are investigated. This study is performed considering very different carrier statistics (Fermi-Dirac and random carrier distribution). With the results from both simulation and experiments I concluded that the free carrier effects dominate the form of the gain and spontaneous emission spectrum for the QD ensemble, rather than the carrier statistics. It was shown that the gain and SE spectra do not show unambiguous signatures which allow the carrier distribution to be deduced.

In order to identify the carrier distribution it is proposed that we may study the GS and ES1 peak values in SE and gain. The values of average carrier occupancy of the QDs, <n>, at which these values cross may provide an indication of the carrier statistics at

play. However, the data from simulation and experiments are not easily comparable since the carrier lifetime is not known. The simulation results determine the peak values as a function of the average number of carriers per QD while the experimental data determines these values as a function of carrier density. Comparing these two parameters requires accurate knowledge of the carrier lifetime. With an experimental method which gives the carrier lifetime simultaneously with the gain and SE spectrum, we may be able to determine the carrier statistics at play within the QDs. Differential carrier lifetime and temperature dependent studies have been carried out to this end, but a combined measurement has yet to be carried out [1]. It is noted however, that the determination of the carrier statistics may be of secondary importance, as compared to a more thorough understanding of the precise role of free carrier effects.

In order to achieve broader spectral bandwidths of SLDs and SOAs, hybrid QW/QD structures have been introduced [2-4]. The effect of additional QW on the performance of the QD active element was discussed in chapter 3. This work was done as the samples may have cast some light on the carrier statistics as a "chirped" set of QDs was used. It was shown that incorporating QW layers in hybrid QW/QD structures has an influence on the behaviour of the QDs. Structurally different samples have been investigated indicating that emission from the quantum well layer is modifying the QD emission in terms of the emission spectrum and an increase in the intensity of the GS following apparent saturation. This is in line with previous laser characterisation that suggested a similar increase in gain in hybrid QW/QD laser structures [4].

However, direct measurement of the QD gain increasing under high levels of QW emission is required for further investigations. For the SLD structure which was analysed in chapter 3, self heating effects were the main reasons for being unable to

unambiguously show that optical pumping of the QDs lead to an increase in gain. To overcome this issue, either low temperature measurements or new samples with fewer QD layers would help in obtaining a stronger QW emission/more rapid QD saturation. For this purpose, custom wafers should be grown with a few (only one or two) layers of QDs in addition to the QW layer.

Also, a chirped QD sample with similar structure as QLF1375-AI with no QW layer can be used in order to investigate the band filling effects at different temperatures. The Monte-Carlo model presented in the second chapter can be used in order to design future samples with optimised design for flat and broad gain spectra.

The lowest energy level of the QW in the hybrid sample QLF1375-AG was ~20nm shorter than the ES2 of QD layers. In future, a similar sample but with QW lowest state offset of 20nm to the longer wavelength or at the ES2 centre wavelength can be designed. For such a sample, the shift in the peak wavelength and FWHM can be investigated with regard to the QW optical pumping effect.

The other method of measuring gain is the Hakki-Paoli method, but observing GS gain during QW lasing is problematic due to difficulties in rejecting laser light in the optical spectrum analyser, therefore, multi-section measurement with high QW emission with GS saturation at a low current density is considered to be the easiest method.

Moreover, for hybrid QW/QD lasers, if the onset of QD GS lasing is due to the QW optical pumping effect (the QW lasing at lower currents), then one can argue that the modulation rate of the QD laser should be faster since the fast carrier dynamics of QW can be imprinted to the QD GS. Whilst a higher modulation rate may be achieved, this would be a rather inefficient modulation scheme. This effect may be harnessed in future

in all-optical signal processing where a ~1100nm signal could be transferred to 1300nm without the need to enter the electrical domain.

Chapter 4 provides the experimental analysis of a variety of configurations implemented using commercial QD-SOAs and QW-SOAs. Firstly, a dual QD-SOA, ring cavity SSL has been realised with 94nm spectral bandwidth and 17mW of output power. This highlighted the opportunity to use a dual pass OSA system with complimentary SOAs. Such a complimentary SOA SSL was developed with a spectral coverage of 154nm with the possibility to be increased to ~220nm by increasing the current to the SOA beyond the recommended rating. Finally, for a filtered ASE source a spectral coverage of 225nm is obtained, but with very low powers. Routes to improve these structures were discussed.

In order to improve the functionality of the SLS, higher gain and saturation power QD-SOAs are required. A simple method to achieve this is to engineer QD-SOAs with longer length. Moreover, epitaxial development can provide higher quantum dot areal density and more QD layers in the active area, increasing the gain coefficient, and negating the need for increased SOA length.

To make the hybrid QW/QD configuration more efficient, advanced epitaxial processes may be used in order to design and grow QW or QD active areas on one wafer. Or alternatively, hybrid QW/QD wafers as discussed in chapter 3 should be utilized in SOA fabrication leading to broader bandwidth.

As a final development possibility for these devices, it is proposed that in future integrated filters may be utilized in order to fabricate very short cavity SLSs. This is proposed by implementing filters such as ring resonators in conjunction with the active element, reducing the cavity length to the ~500-1000μm range.

References

[1] K. Zhou ,"Analysis of 1.3μm GaAs quantum dot structure based devices," PhD thesis, Department of Electronic and Electrical Engineering, University of Sheffield, Jan 2014.

[2] S. Chen, K. Zhou, Z. Zhang, J. R. Orchard, D. T. D. Childs, M. Hugues, O. Wada, and R. A. Hogg, "hybrid quantum well/quantum dot structure for broad spectral bandwidth emitters," IEEE J. Select. Topics Quantum Electron., 19, 1900209, (2013).

[3] S. Chen, K. Zhou, Z. Zhang, D. T. D. Childs, M. Hugues, A. Ramsay, and R. Hogg., "Ultra-broad spontaneous emission and modal gain spectrum from a hybrid quantum well/quantum dot laser structure," Appl. Phys. Lett., 100, 041118 (2012).

[4] S. Chen, K. Zhou, Z. Zhang, O. Wada, D. T. D Childs, M. Hugues, and R. A. Hogg., "Room temperature simultaneous three-state lasing in hybrid quantum well/quantum dot laser," Electron. Lett., 48, 644 (2012).

Appendix 1: Monte Carlo model Methodology

In this appendix the calculation used in this model is described step by step and the methodology is discussed.

A1.1 Setup energy array for the QDs in ensemble

In this model inhomogeneous broadening of the QDs in ensemble is approximated as a Gaussian function due to the self organised nature of the growth method. Whilst the Normal distribution is not perfect, it does represent the simplest to implement in most cases. However, in this model, any distribution could be used, since the QDs are treated individually. Knowing the total number of QDs in the ensemble, they are distributed in energy based on the Gaussian distribution. For simplification, a discrete Gaussian function is considered with 0.1meV energy steps, since this is well below the inhomogeneous linewidth at room temperature, the discretisation would not be resolved spectrally. The value of the Gaussian function at each energy step (E_i) defines the number of QDs with ground state energy equal to E_i. By the end of this function each QD would have an associated energy value such that the ensemble follows a Gaussian distribution.

For this calculation 5000 points in energy is assumed, separated by 0.1meV, therefore covering from -150meV to 350meV with respect to the ground state center energy, (defined as 0meV). QDs outside this range are not considered. For even widely broadened ensembles (e.g. Γ_{inhom}=50meV) and considering a population of $1x10^6$ QDs, this will lead to maximum one QD out of calculation range, therefore this is a good enough approximation to consider.

Figure A1.1(a) shows a simplified flow chart for this calculation. An inhomogeneous distribution of an ensemble with 12 QDs is schematically plotted in figure A1.1(b), with larger (smaller) QDs at lower (higher) energy levels. Each QD in this ensemble will be associated with an energy value with regard to its size (figure A1.1(c)).

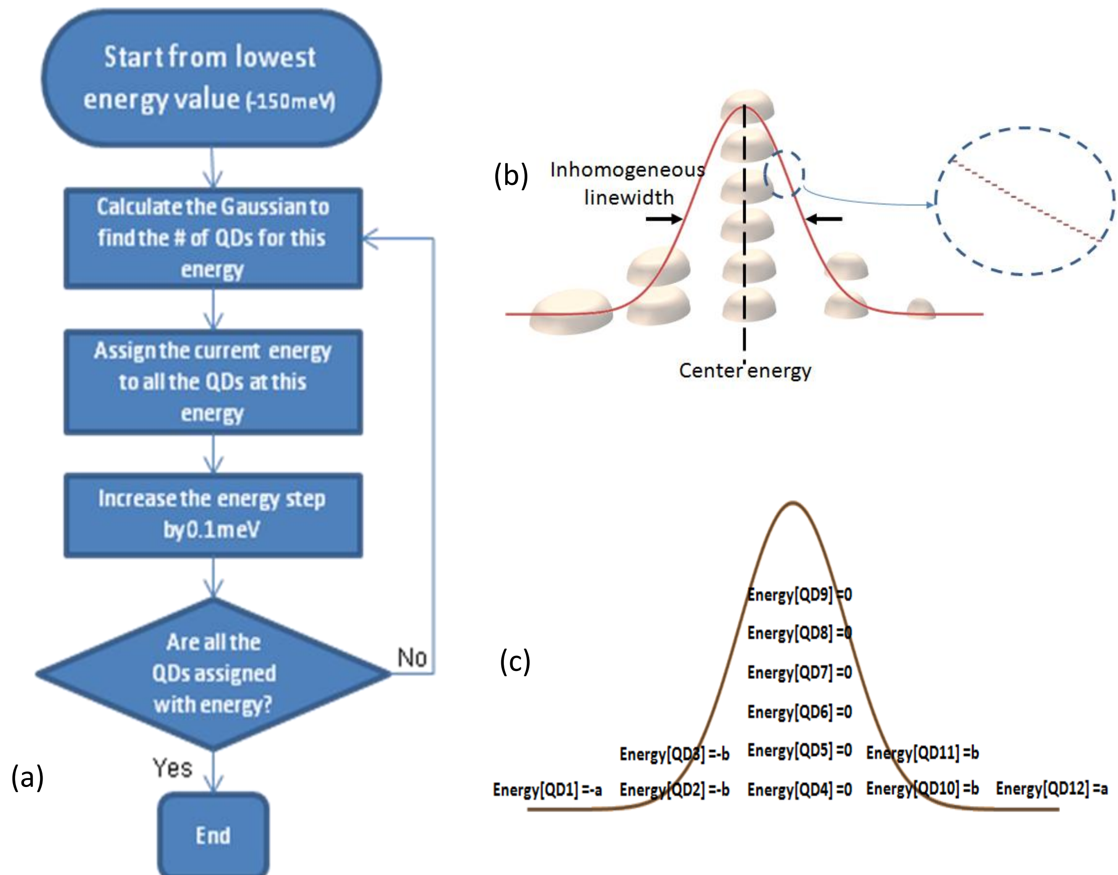

Figure A1.1: (a) Flow chart for setting the energy of each QD based on the inhomogeneous broadening, (b) Schematic of how QDs in an ensemble of 12 QDs are distributed through a Gaussian function, (c) Filled energy array at each QD.

A1.2 Applying carrier statistics

For each QD in the model 5 available quantized energy levels are assumed (The fifth energy level is the wetting layer). It is the form of the carrier statistics chosen that causes the carriers to fill this energy level system differently. In a Random distribution, the QDs are filled randomly with no preference of QD energy/size. Figure A1.2 schematically shows an ensemble with 3 QDs with their energy levels filled randomly.

In this algorithm one QD can have carriers in its excited states while the ground state of other QDs are still empty.

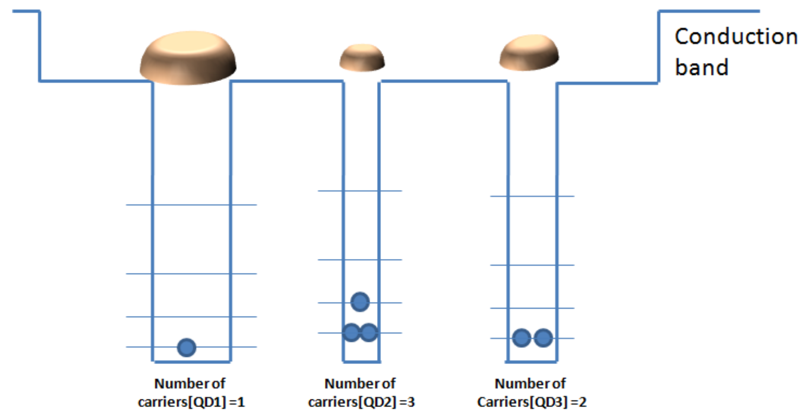

Figure A1.2: Schematic of an ensemble with 3 QDs filled randomly

In Fermi-Dirac distribution, to fill the QDs, an incremental trial quasi-Fermi level is considered starting bellow the lowest energy level and then iteratively increased toward higher energy levels. A suitable small step in this trial quasi-Fermi energy is required to get close enough to the desired number of total carriers allocated to QDs. A step in Fermi energy of 0.02meV gives an error of 0.01 carriers per QD. Decreasing this step size increases accuracy without a significant impact on total computing time, but is only of value for large QD populations. This process is schematically shown in figure A1.3.

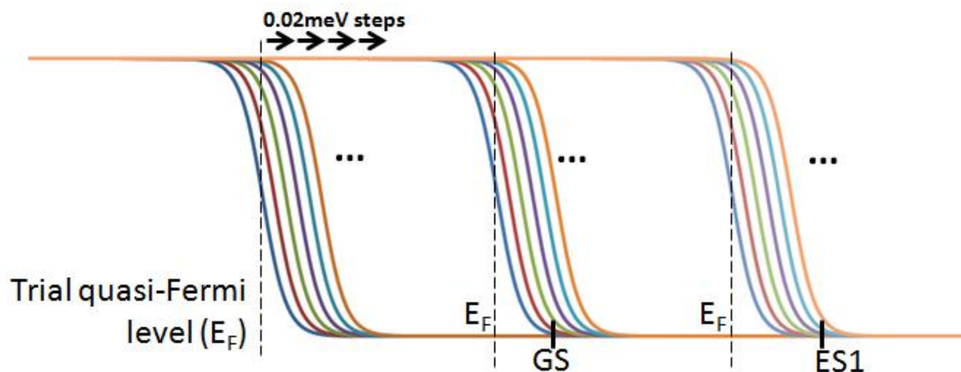

Figure A1.3: Increase in trial quasi-Fermi level to calculate the occupation probability of each available energy level.

At each QD energy level, the probability of occupation is dealt with by a random number (0 to 1) compared to the Fermi function. During the filling process, Pauli exclusion is dealt with by filling the lowest free energy state in each QD. If a QD has two electrons, and the state separation is large enough, its next free state is too high, so is far less likely to receive the third carrier until the ensemble is close to full. For a large state separation, contrasting with the random filling, a QD is unlikely to have any carriers in the excited state before the ground states of the entire ensemble are full. In reality, for this to be true, the carrier capture and escape for each QD must be rapid relative to the recombination lifetime.

The throw of the dice is done once for every QD in each loop, so each loop can put one carrier into a QD or not. As such it is repeated so that the QD could be full, i.e. for 5 levels of degeneracy, 2+4+6+8+10=30 carriers per QD will be the maximum occupancy. This essentially allows every confined state to be compared to Fermi probability.

Figure A1.4(a) shows a simplified flow chart for Fermi filling algorithm. Figure A1.4(b) schematically shows same ensemble in figure A1.2 filled by this algorithm.

Bandgap shrinkage causes energy shifts related to the number of carriers per QD. In this model it is assumed that the bandgap shrinks with the one-third power of carrier density as in both bulk and quantum-well materials. Energy levels are shifted according to carrier occupancy in each QD. This is done whilst filling the QDs since it affects the lowest free-state energy.

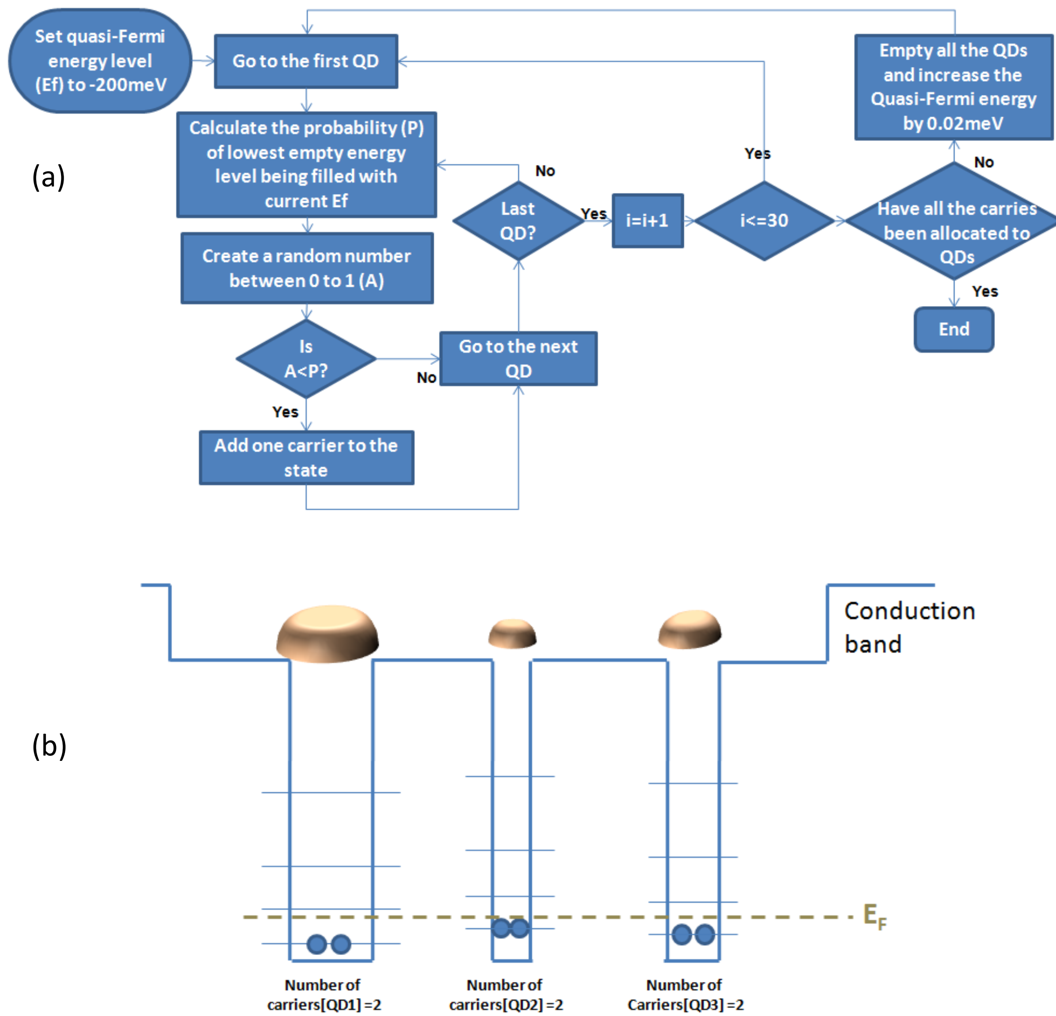

Figure A1.4: (a) The flow chart for filling algorithm based on Fermi-Dirac statistics, (b) Schematic of an ensemble with 3 QDs filled with this algorithm.

A1.3 Gain calculation

In the previous steps, the state energy and number of carriers in each QD is defined. Knowing these parameters the gain of each QD can be calculated and these discrete gain spectra can be integrated over the entire ensemble. Figure A1.5 schematically shows the gain of one QD as the number of carriers is increasing. Free carrier effects are not shown here and only 3 energy levels are plotted for simplicity.

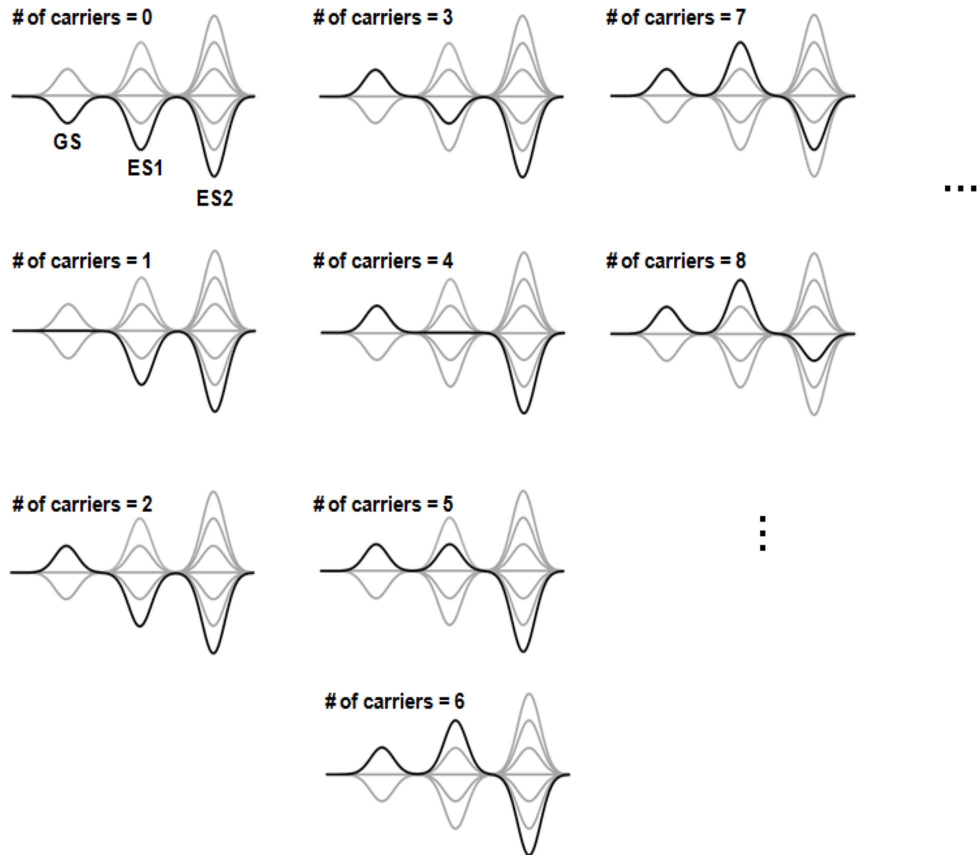

Figure A1.5: Schematic of Gain for one QD as the number of carriers is increasing. Free carrier effects are not shown and only 3 energy levels are plotted for simplicity.

Homogeneous broadening is applied to this model during the gain calculation process. This homogeneous broadening consists of two parts, firstly a carrier-phonon interaction which is the base homogeneous broadening. This homogeneous broadening is related to the temperature of the lattice, and is considered identical for all QDs. A second additional contribution is a further broadening from carrier-carrier interactions, and is applied based on the individual QD occupancy. For both, a Lorentzian function is considered in array units of 0.1meV to span either side of the discrete state energy level center. Figure A1.6 shows the flowchart for gain calculation.

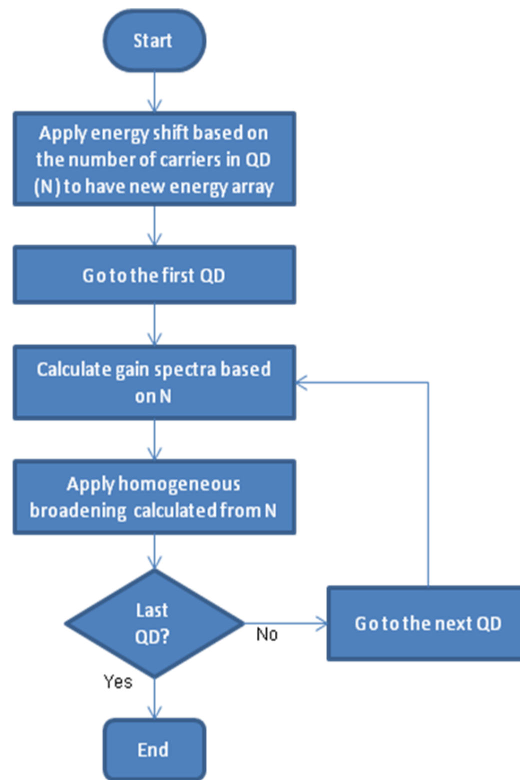

Figure A1.6: Flow chart of gain calculation for QD ensemble

A1.4 considerations

The number of QDs considered in this model considerably affects the computing time. Figure A1.7 shows how the computing time increases with the number of QDs. In this graph the runtime on a single core of an Intel(R) Core(TM) i3 CPU processor running at 2.4GHz, is calculated for average number of carries per QD increasing from 0 to 10 in steps of 0.2, considering Fermi-Dirac statistics and including the free carrier effects.

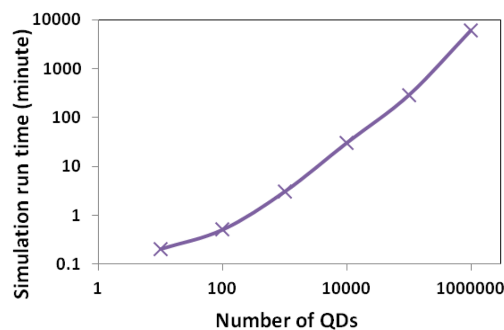

Figure A1.7: Simulation runtime as a function of number of QDs

On the other hand, more number of QDs in model leads to more accurate simulation results. From figure A1.7, it can be seen that the relationship is approximately linear for large QD numbers, this is as expected since the QDs are treated individually for almost every step of the calculation. The code is written in C and compiled for a single processor, so the speed scales directly with clock speed. Since processor speeds have not increased significantly in recent years in favour of more cores, parallelism is needed. The simplest way to improve throughput on modern multi-core processors is to run one instance of the code on each core with different input parameters.

The gain spectra at the ground state with 1.2 average number of carriers per QD, are plotted in figure A1.8 for different number of QDs for Fermi-Dirac and random statistics with and without homogeneous broadening. In figure A1.8(a) by applying random carrier statistic and no homogeneous broadening with 10 QDs in the ensemble, the discrete values for the gain of occupied QDs are clearly resolved. By increasing the number of QDs the gain spectra gets smoother due to the overlap of more QDs. With 1,000,000 QDs the gain spectra shows a very smooth profile. In figure A1.8(b) same graphs are plotted for random carrier statistics including homogeneous broadening in the calculation. Since the gain spectrum for each QD broadens based on the occupied number of carriers, there is greater overlap between neighbouring QDs, and the spectra appear smoother at lower number of QDs. Figure A1.8(c) and (d) show that the same trend is observed with Fermi-Dirac carrier statistics. For this simulation above 100,000 QDs is found to be sufficient to have a smooth gain profile. For all the simulations in this chapter 1,000,000 QDs are considered for more accurate results.

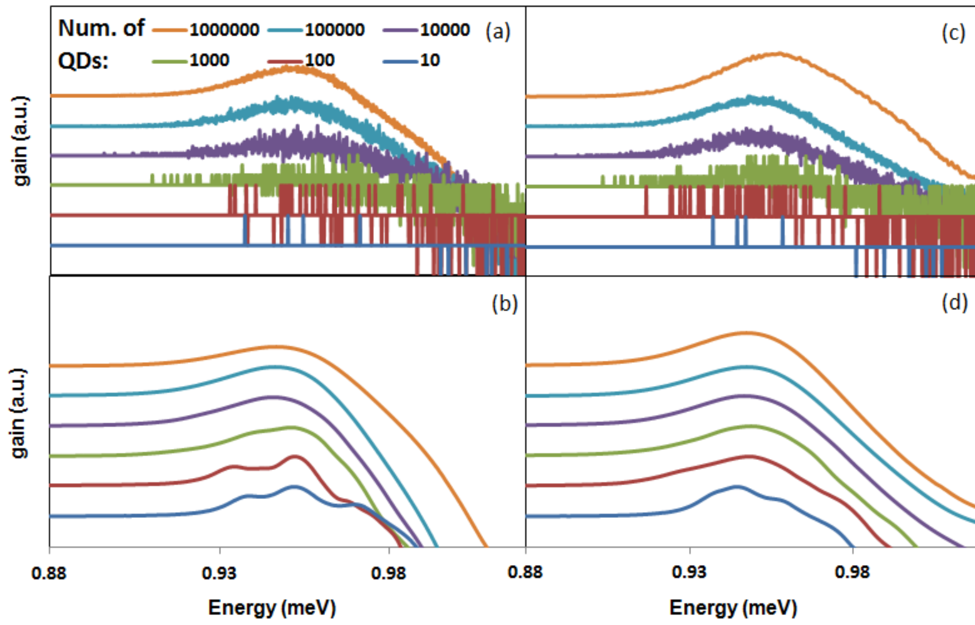

Figure A1.8: Normalized gain at ground state for (a) Random statistics with no homogeneous broadening, (b) Random statistics with homogeneous broadening, (c) Fermi-Dirac statistics with no homogeneous broadening and (d) Fermi-Dirac statistics with homogeneous broadening. The gain spectra at the ground state are plotted at 1.2 average number of carriers per QD.

Appendix 2: BOA 1130: O-Band booster amplifier

TQE
10335 Guilford Road, Jessup, MD 20794, USA
Phone: +1 877.226.8342 **Fax**: +1 240.456.7200
Email: sales@covega.com **Web**: http://www.covega.com

BOA 1130: O-band Booster Optical Amplifier

7.1.2.SP.1130 Rev C

Description

The BOA 1130 is a high saturation output power high bandwidth polarization maintaining Booster Optical Amplifier (BOA). It incorporates a highly efficient InP/InGaAsP Quantum Well (QW) layer structure and a reliable ridge waveguide design.

It is housed in a standard 14 pin butterfly package with integrated thermoelectric cooler and thermistor. Packaging options include isolator(s) and choice of single mode fiber and polarization maintaining fiber tails.

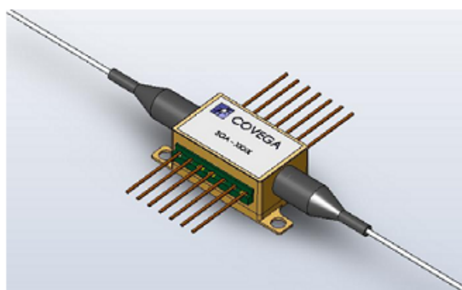

Features

- → High Saturation Output Power
- → Broad Spectral Bandwidth
- → High Fiber-to-Fiber Gain
- → High Polarization Extinction Ratio

Applications

- ✓ Telecom & Datacom
- ✓ Booster Amplifier of Fixed and Tunable ITU Lasers and Transmitters
- ✓ Swept-Source Tunable Lasers

Specifications

CW; T (Chip) = 25°C, T (Case) = 0 - 70°C

Parameter		Min	Typ	Max	
Operating Current	I_{OP}		600	750	mA
Central Wavelength	λ_C	1265	1285	1295	nm
Optical 3 dB Bandwidth	BW	80	87		Nm
Saturation Output Power @ -3 dB	P_{SAT}	15	17		dBm
Small Signal Peak Gain @ Pin = -20 dBm	G	27	30		dB
Gain Ripple (rms) @ I_{OP}	δG		0.2	0.3	dB
Noise Figure	NF		7	9	dB
Forward Voltage	V_F		1.6	2.0	V
TEC Operation (typ / max @ T_{CASE} = 25°C / 70°C)					
- TEC Current	I_{TEC}		0.4	1.5	A
- TEC Voltage	V_{TEC}		0.5	4.0	V
- Thermistor Resistance	R_{TH}		10K		Ω
SPECIFICATIONS SUBJECTED TO CHANGE WITHOUT NOTICE					

THE PICTURE IS A REPRESENTATION. THE ACTUAL PART MAY VARY FROM THE ONE SHOWN.

COVEGA

TQE
10335 Guilford Road, Jessup, MD 20794, USA
Phone: +1 877.226.8342 **Fax**: +1 240.456.7200
Email: sales@covega.com **Web**: http://www.covega.com

BOA 1130

Performance

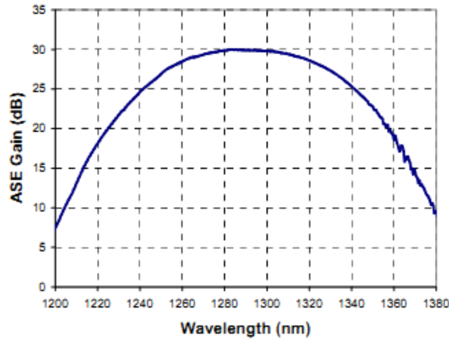

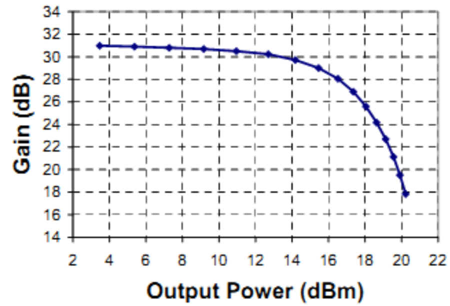

Packaging

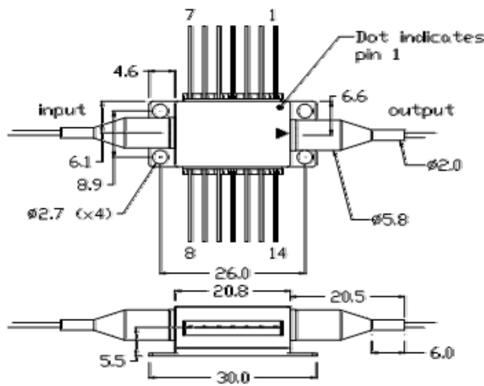

PIN IDENTIFICATION

1.	TEC +	14.	TEC −
2.	Thermistor	13.	Case
3.	NC	12.	NC
4.	NC	11.	SOA Cathode
5.	Thermistor	10.	SOA Anode
6.	NC	9.	NC
7.	NC	8.	NC

Recommended mounting torque is 10-20oz.in (0.07-0.14Nm).

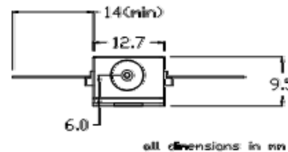

all dimensions in mm

Ordering Information

BOA 1130 - X - 0 - X - X - X - X - X

X **Isolator**	0 **Reserved**	X **Fiber jacket configuration***	X **Input Fiber**	X **Output Fiber**	X **Input Connecter**	X **Output Connector**	Numeric **Grade Level**
0 = none		T = SMF-28, tight jacket	S = SMF	S = SMF	A = FC/APC	A = FC/APC	0 / blank = Std.
1 = input only		W = PMF 1300 nm, loose tube	P = PMF	P = PMF			1 = XL
2 = output only							2 = Reserved
3 = input & output							

* see all of the fibertail options in the Covega catalog

© TQE - All rights reserved